University of Sussex

The Thermal Sunyaev-Zel'dovich Effect from the Epoch of Reionisation

Azizah R Hosein

Submitted for the degree of Doctor of Philosophy

University of Sussex

December 2020

Declaration

I hereby declare that this thesis has not been and will not be submitted in whole or in part to another University for the award of any other degree.

The following is a breakdown specifying the work which was done by my supervisor, collaborators and myself, in the relevant sections of this thesis.

3.2 Simulations

The CoDa II run and post-processing was done by the CoDa II collaboration. The 100 Mpc, 50 Mpc and 10 Mpc auxiliary simulations were performed by my supervisor, Prof Ilian T. Iliev, using initial conditions provided by the CLUES collaboration. I ran the 25 Mpc auxiliary simulations using initial conditions which I created using MUSIC. I made the calibration plots in Section 3.2.4 using simulation output files, CoDa II star particle files provided by the CoDa II collaboration, and the `seren3` package developed by my previous coworker Dr David Sullivan.

3.3 Methodology

The cubes of the hydrodynamic properties were made by Dr Pierre Ocvirk of the CoDa II collaboration. I made the the auxiliary simulation cubes of the hydrodynamic properties using the RAMSES `amr2cube` tool. I constructed the lightcones for all simulations using scripts which I wrote for this purpose, utilising and modifying the Python module `c2raytools` for the integration. I also performed the tests in Section 3.3.3.

3.4 CoDa I

CoDa I was run and post-processed by the CoDa I collaboration. The cubes of the hydrodynamic properties were made by Dr Pierre Ocvirk of the CoDa I collaboration. I constructed the lightcones for CoDa I using the tools mentioned in the previous section.

4 Results

All graphs in this chapter were plotted by me.

4.1.2 Impact on Galaxy Cluster Measurements

Dr Rajesh Mondal calculated the angular power spectra from the maps that I made, and provided the l and C_l data for Figure 4.7.

Signature:

Azizah R Hosein

UNIVERSITY OF SUSSEX

Azizah R Hosein, Doctor of Philosophy

The Thermal Sunyaev-Zel'dovich Effect from the Epoch of Reionisation

Abstract

The thermal Sunyaev-Zel'dovich (tSZ) effect arises from inverse Compton scattering of low energy photons with thermal electrons, and is usually observed in galaxy clusters. During the Epoch of Reionisation (EoR), although the temperature of the ionised intergalactic medium (IGM) is lower, its high density leads to an increased electron pressure which results in a tSZ effect. In order to investigate its strength, we analyse data obtained from fully-coupled radiation-hydrodynamics simulations and construct lightcones of the electron pressure in the IGM during the EoR. These simulations utilise the hybrid CPU-GPU code RAMSES-CUDATON and span the duration of reionisation. We vary the box sizes, star formation parameters and resolutions to investigate how these factors affect the tSZ effect. We produce plots of maps and distributions of the Compton y-parameter, as well as angular power spectra of the tSZ signal, obtained from integrating the lightcones constructed for each simulation. We find that having a high box resolution is important as smaller areas where the temperature is higher are better resolved, leading to higher values of the y-parameter. We estimate the average y-parameter arising from the EoR to be $\langle y \rangle \sim 10^{-8}$, making this the first time this value has been calculated from numerical simulations. In the case of the power spectra, on scales probed by current technology, we find that the tSZ signal from the EoR is $< 1\%$ of that modelled by cluster templates. Our results suggest that it would be worthwhile to consider the contribution of the EoR to the tSZ effect in the future when more sensitive technologies emerge.

Acknowledgements

I would like to start by thanking my supervisor, Ilian Iliev, for his support and guidance throughout my PhD. Without his help, I would not have been able to complete this work. Thank you for your patience with me and your willingness to explain even the simplest concepts that I needed clarifying. Next, I would like to thank my second supervisor, Mark Sargent. Although my work ultimately did not involve radio interferometry, I am grateful for the guidance which you gave me at the start of my PhD and being there for any additional support that I needed along the way. I would also like to thank Keri Dixon and Rajesh Mondal who have both assisted me with my research. I am indebted to David Sullivan for the immense help which he gave while at Sussex and even after leaving. I am also grateful to my collaborators Paul Shapiro, Pierre Ockvirk, Taha Dawoodbhoy, and others who provided some of the data for this study and kindly provided assistance when needed. I would also like to thank Jens Chluba, whose suggestion it was to carry out the investigation on which this thesis is based.

A special thanks goes out to the friends I have made during my time at Sussex. My friends and office-mates from both 4C15 and 4C13: David Sullivan, Hannah Ross, Alexander Eggemeier, Antonio Vázquez, Carlos Vergara, Rosemary Coogan, Sunayana Bhargava, and Michele Bianco; thank you for the banter, snacks, making the office and enjoyable place to be, and keeping me sane. I would also like to mention Scott Clay, Mateja Gosenca, Dániel Molnár, Ridwan Barbhuiyan, Benoît Fournier, Steven Duivenvoorden, Chris Lovell, Sean Butchers, Michaela Lawrence, Pippa Cole, Ciaran Fairhurst, and the other members of the Astronomy Centre. Outside of the Astronomy Centre: Caroline Hurley, whose witty humour and intellectual, non-Astronomy conversations I will miss; Dimitrios Theodorakis, with whom I've enjoyed many meals and sweets; the friends from Caribbean Students Unite, who added the vibes and eased my homesickness. I cherish the friendships I have made during this period of my life and I already know that I will have ties with some of you that will extend beyond these years.

I'd like to thank my parents, Ishrad and Zalimoon Hosein. Words really cannot express the depths of my gratitude. Without your support, I wouldn't have reached where I am

today. For this, I am eternally grateful. My sister, Faaizah Hosein, thank you for putting up with me, the witty burns, forever having my back, and always forgiving me. You are someone I can rely on to be honest with me, and one of the most talented people I know. To Akshey Shah, thank you for being there for my sister, especially at times when I couldn't. My late grandmother, Shiroon Hosein, although you are no longer here, I know you'd be proud. To my Uncle Monaph Hosein and his family, and my Auntie Hamida Mohammed and her family, you are my closest relatives. You continue to be there for my family and me, and without you, I also would not be here.

Thanks to my friends and support group in Trinidad: my best friend, Kimberley Ali, who feels more like a sister, and is one of the few people whom I can say truly knows me, yet at times discourages my slackness; Michael Ali for taking me on adventures, putting up with my oddities, and encouraging my slackness; Phillip Young Hoo for being an awesome senpai, someone with whom I can have wholesome conversations about life and self-development, and for taking me to fetes; Vincent Chanicka for the moral support, and being someone I can feel totally comfortable (to be my weird self) around and talk to about almost anything; Rashad Khan for your (occasional) rationality and listening ear. My liming posse: Denva Lutchman, Lorenzo Labban, Ravi Mahabir, Gina Jules, Custer Lutchman, Imran Samad, and Keenan Lutchman (RIP), who always considered me as part of the group even though I didn't return home often.

Thank you to Jonathan Young and his family, who made me feel like part of their own during my undergrad years and the first half of my PhD.

Lastly, but definitely not least, I would like to thank my viva examiners, Robert Crain and Peter Thomas. Your friendliness eased my initial anxiety and helped to make the process enjoyable. I am grateful for your insights and suggestions which have made this thesis more complete.

This list is not exhaustive by far. There are many, many more who have made a positive impact on my life, but it is getting quite lengthy, so I shall stop.

"For nothing is so productive of elevation of mind as to be able to examine methodically and truly every object which is presented to thee in life, and always to look at things so as to see at the same time what kind of universe this is, and what kind of use everything performs in it, and what value everything has with reference to the whole..."

— **Marcus Aurelius, Meditations**

Contents

List of Tables

List of Figures

Chapter 1

Introduction

1.1 Modern Cosmology

In 1929, Edwin Hubble and Milton Humason observed that nearby galaxies were travelling away from us (Hubble and Humason, 1931). This led to Hubble's law. It states that the velocity of this recession is proportional to the distance of the object from us:

$$\boldsymbol{v}(t) = H(t)\boldsymbol{r}(t), \tag{1.1}$$

where $H(t)$ is the time-dependent Hubble parameter. Its value today is

$$H_0 = 100h \text{ km s}^{-1} \text{ Mpc}^{-1}, \qquad h = 0.674 \pm 0.005, \tag{1.2}$$

where the subscript 0, by convention, denotes present time, and h is the uncertainty in the measurement with its value given by the Planck 2018 cosmology (Planck Collaboration et al., 2018a).

This universal expansion Doppler shifts cosmic light travelling towards us to longer wavelengths. This shifting of the light to redder wavelengths is thus referred to as redshift,

$$z = \frac{\lambda_{\text{obs}} - \lambda_{\text{em}}}{\lambda_{\text{em}}}, \tag{1.3}$$

where λ_{obs} and λ_{em} are the wavelengths of the observed and emitted light, respectively.

We measure the expansion of the Universe with the scale factor,

$$a(t) = \frac{1}{1+z}, \tag{1.4}$$

which is related to the Hubble parameter by

$$H(t) = \frac{\dot{a}(t)}{a(t)}, \tag{1.5}$$

where $\dot{a}(t)$ denotes the time-derivative of the scale factor.

Another fundamental cornerstone of modern cosmology is the cosmological principle (or Copernican principle), which states that the universe is both homogeneous and isotropic on large scales, i.e. it is uniform at all points and in all directions. Consequently, it means that our position in the Universe is not special. This is evidenced in large-scale galaxy surveys and the almost homogeneous cosmic microwave background (CMB) (Penzias and Wilson, 1965).

The cosmological principle allows for an exact solution of Einstein's field equations of general relativity (GR). This is given by the Friedmann-Lemaître-Robertson-Walker (FLRW) metric. From this metric, we can derive the Ricci tensor and Christoffel symbols. Substituting these into Einstein's field equations gives us the Friedmann equation:

$$H^2(t) = \frac{8\pi G}{3}\rho - \frac{kc^2}{a^2}, \tag{1.6}$$

for a universe with curvature measured by the constant k. Observations suggest that we live in a flat ($k = 0$) universe. Taking this into account, we can rearrange the Friedmann equation and define the critical density:

$$\rho_c = \frac{3H^2}{8\pi G}, \tag{1.7}$$

which is the density required to yield a universe of this curvature. Since the Hubble parameter varies with time, the critical density is not a constant.

It is conventional to express the energy density contributions in terms of the density parameter,

$$\Omega = \frac{\rho(t)}{\rho_c}. \tag{1.8}$$

Observations suggest that the energy content of the universe is comprised of matter, radiation and dark energy. The latter is expressed as a cosmological constant, Λ, and first appeared in Einstein's field equations as a way to balance gravity. It can be thought of as vacuum energy and is considered to be responsible for the accelerating expansion of the universe.

Using the density parameter and considering how the components scale with redshift, we can rewrite the Friedmann equation as:

$$H^2 = H_0^2 \left[\Omega_{r,0}(1+z)^4 + \Omega_{m,0}(1+z)^3 + \Omega_{k,0}(1+z)^2 + \Omega_{\Lambda,0}\right], \tag{1.9}$$

where the subscripts r and m represent radiation and matter, respectively. For a spatially flat universe, we find that

$$\Omega_0 = \Omega_{r,0} + \Omega_{m,0} + \Omega_{\Lambda,0} = 1. \tag{1.10}$$

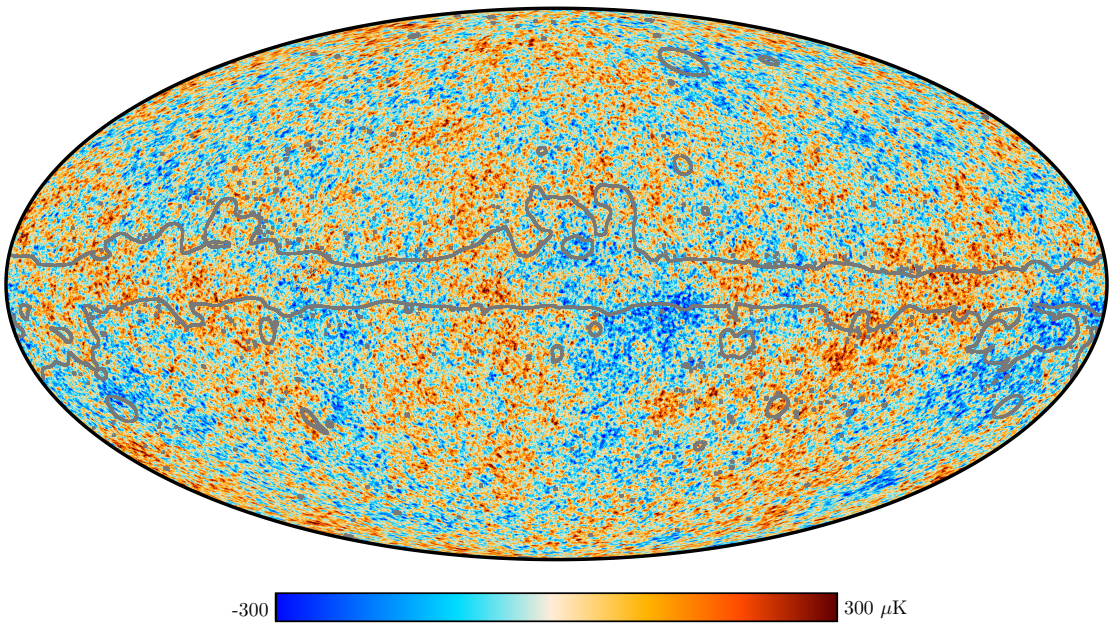

Figure 1.1: The Planck CMB sky. Tiny temperature fluctuations correspond to regions of slightly varying densities. Blue spots are slightly colder than the average temperature, while red spots are slightly hotter. Credit: ESA/Planck Collaboration (Planck Collaboration et al., 2018b).

Of these parameters, only $\Omega_{r,0}$ has been accurately measured directly. $\Omega_{r,0}$ is dominated by the energy of the CMB. The Cosmic Microwave Background Explorer (COBE; Smoot et al., 1992) measured its temperature to be 2.725 ± 0.001 K, which corresponds to a radiation density parameter $\Omega_{r,0} = 2.47 \times 10^{-5} h^{-2}$.

1.2 Angular Power Spectrum

Although the temperature of the CMB is impressively homogeneous, there still exists small fluctuations around the average value (approximately 1 part in $10,000$). Since we observe the CMB temperature as a map projected onto a 2D spherical surface sky (see Figure 1.1), it is most appropriate to express the temperature fluctuations using spherical harmonics. The set of spherical harmonics are orthonormal and defined as:

$$Y_{lm}(\theta, \phi) = \sqrt{\frac{2l+1}{4\pi} \frac{(l-m)!}{(l+m)!}} P_l^m(\cos\theta) e^{im\phi}, \tag{1.11}$$

where $l = 0, ..., \infty$ is the multipole, $-l \leq m \leq l$, and P_l^m are the Legendre polynomials. The multipole, l, represents an angular scale in the sky (in degrees), $\alpha = \frac{\pi}{l}$.

The temperature fluctuations in the CMB can be decomposed in spherical harmonics

as:

$$\Theta\left(\hat{\mathbf{n}}\right) = \sum_{l=0}^{\infty} \sum_{m=-l}^{l} a_{lm} Y_{lm}\left(\hat{\mathbf{n}}\right), \tag{1.12}$$

where $\hat{\mathbf{n}}$ is a unit direction vector, $Y_{lm}\left(\hat{\mathbf{n}}\right)$ are the spherical harmonic functions, and a_{lm} are the harmonic coefficients given by

$$a_{lm} = \int_{\theta=-\pi}^{\pi} \int_{\phi=0}^{2\pi} \Theta\left(\hat{\mathbf{n}}\right) Y_{lm}^{*}\left(\hat{\mathbf{n}}\right) \mathrm{d}\Omega. \tag{1.13}$$

The power spectrum of the fluctuations can be defined as the variance of the harmonic coefficients:

$$\langle a_{lm} a_{l'm'}^{*} \rangle = \delta_{ll'} \delta_{mm'} C_l, \tag{1.14}$$

where C_l is the ensemble average power spectrum and the Kronecker delta functions are a result of isotropy. For our sky, the power spectrum is

$$C_l = \frac{1}{2l+1} \sum_{m=-l}^{l} \left\langle |a_{lm}|^2 \right\rangle. \tag{1.15}$$

The error in this estimation, $\Delta C_l = \sqrt{\frac{2}{2l+1}}$, depends on the number of points in the sample, and is referred to as cosmic variance. For a Gaussian distribution of temperature fluctuations, the distributions of a_{lm} are also Gaussian with mean $\langle a_{lm} \rangle = 0$ and variance C_l.

The power spectrum of the CMB temperature fluctuations is usually plotted as $D_l = \frac{l(l+1)}{2\pi} C_l$. l generally ranges from $l = 2$ to a given maximum value corresponding to the resolution of the instrument. The first term, the monopole ($l = 0$), is excluded since this relates to the whole sky, whose temperature fluctuations should average to 0. The monopole temperature term, although a valuable bit of information, cannot be reliably determined due to cosmic variance, i.e. we cannot be sure that the value we measure locally is actually the same as the average temperature of the universe. The second term, the dipole ($l = 1$, $\alpha = 180°$), is affected by our motion in space and redshift. This results in an anisotropy at this angular scale, which dominates over the true cosmic dipole signal, and is thus also excluded from the power spectrum.

The power spectrum can be calculated as either an auto-power spectrum or cross-power spectrum. The former is proportional to $\sum_m |a_{lm}|^2$, while the latter is proportional to $\sum_m a_{lm}^i a_{lm}^{j*}$, where i and j denote two independent maps of the CMB (e.g. taken at different bandpowers). The advantage of the cross-power spectrum is that biases from uncorrelated noise can be eliminated.

The angular power spectrum is one of the most informative measurements of the CMB (Hu et al., 1997; Aghanim et al., 2008; Challinor, 2013; Bucher, 2015; Balashev et al.,

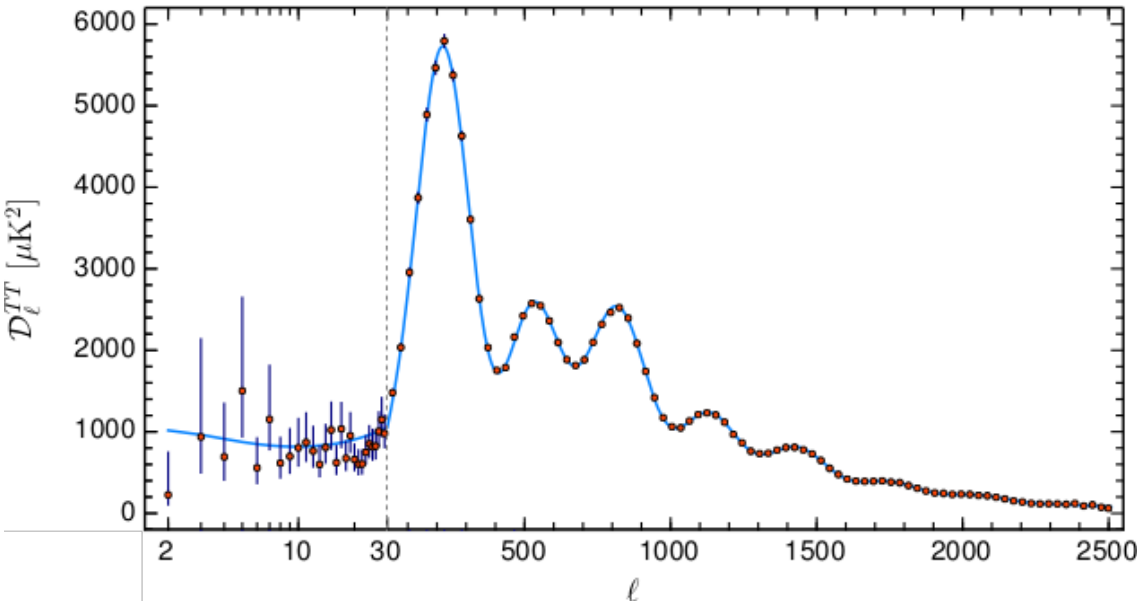

Figure 1.2: Angular power spectrum of CMB temperature anisotropies as observed by Planck. The best fit to the theoretical ΛCDM spectrum is plotted as the light blue line. The red dots and blue error bars are the measurements and their errors, respectively. Credit: ESA/Planck Collaboration (Planck Collaboration et al., 2018a).

Table 1.1: The cosmological parameters from the latest Planck estimates (Planck Collaboration et al., 2018a).

Planck Collaboration 2018 cosmological parameters	
Dark energy density parameter, Ω_Λ	0.685 ± 0.007
Matter density parameter, Ω_m	0.315 ± 0.007
Spatial curvature density parameter, Ω_k	0.0007 ± 0.0019
Hubble parameter, H_0	67.4 ± 0.5 km s^{-1} Mpc^{-1}
Amplitude of matter fluctuations at 8 Mpc h^{-1}, σ_8	0.811 ± 0.006
Spectral scalar index, n_s	0.965 ± 0.004
Optical depth due to reionisation, τ	0.054 ± 0.007

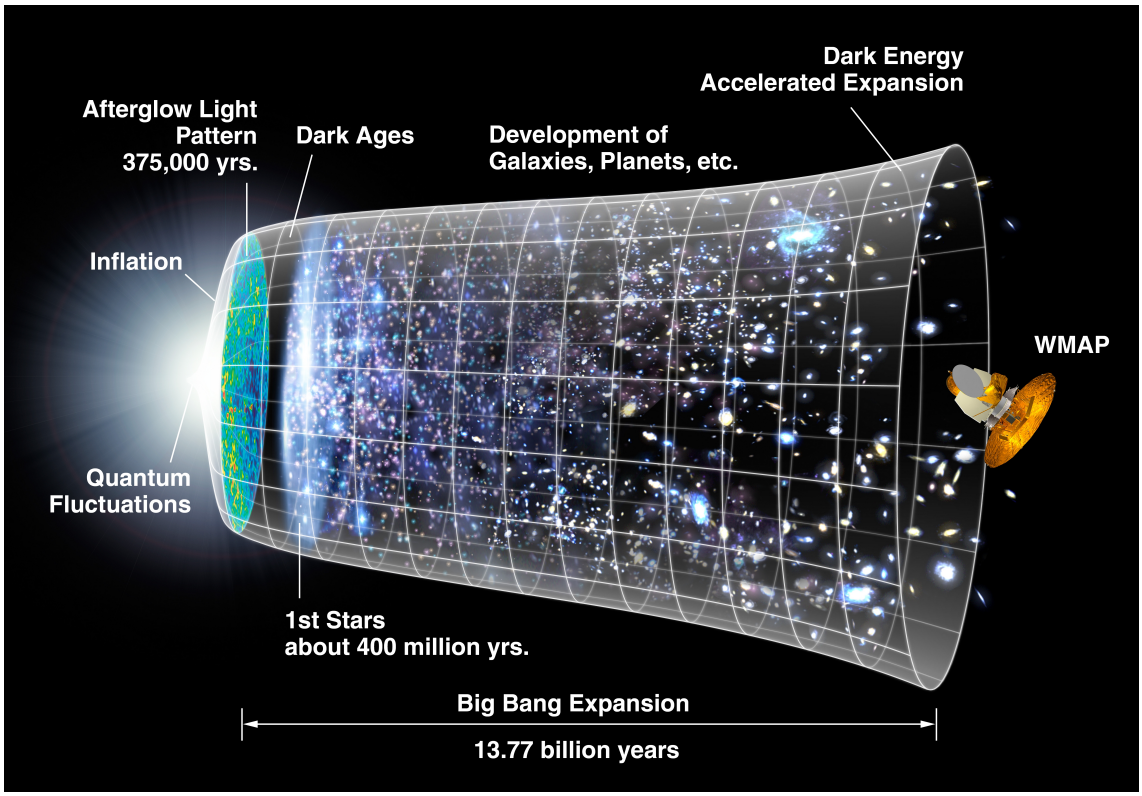

Figure 1.3: The evolution of the universe as described by the Big Bang theory. At the start, inflation causes the universe to rapidly expand to at least 10^{78} times its previous size. Quantum fluctuations at its birth give rise to density fluctuations which become the seeds of structures, such as stars and galaxies. At later epochs, dark energy dominates and drives the expansion of the universe. Credit: NASA/WMAP Science Team

2015; De Zotti et al., 2016). It has enabled us to place constraints on the cosmological parameters. In Figure 1.2 we show the angular power spectrum of the CMB measured by the Planck[1] survey, and in Table 1.1, we list the cosmological parameters constrained by the latest Planck release (Planck Collaboration et al., 2018a).

1.3 History of the Universe

In Figure 1.3, we show a cartoon timeline of the evolution of the universe as is generally accepted. The majority consensus agrees that the Big Bang theory best describes the original state of the observable universe. Tracing the FLRW metric back to the beginning of time suggests that all contents of the universe occupied the same space, i.e. there was no distance between them. It also suggests a scale factor of $a = 0$, meaning all objects would have had an infinitesimal size. All contents would have been crushed into a single hot

[1] https://www.cosmos.esa.int/web/planck/

point, with infinite density, where the laws of physics break down. Hence, the Big Bang is also referred to as the initial singularity. Although there are problems and inconsistencies which arise from this theory, it is still the best description we have of our universe.

In 1981, Alan Guth proposed inflation as a solution to the problems with the Big Bang (Guth, 1981). The theory states that the Universe underwent a period of rapid accelerated expansion, where the scale factor increased by a factor of at least 10^{27}. This expansion ended $< 10^{-32}$ seconds after the Big Bang. An inflating universe traps quantum fluctuations within it. These irregularities are subjected to gravitational instabilities, and eventually give rise to the large-scale structure that we see today.

After inflation, 10^{-12} seconds after the Big Bang, the quark epoch began. During this time, the Universe consisted of quarks, leptons and their antiparticles. This plasma was too hot for these particles to bind together to form baryons. This hadron synthesis happened at 10^{-6} seconds post Big Bang. 1 second after the Big Bang, nucleosynthesis, the period when the Universe was cool enough for the lightest elements (hydrogen, helium and lithium) and their isotopes to form, occurred. For the next $\sim 350,000$ years, matter and radiation are coupled through scattering of photons with baryonic matter.

As the Universe cooled and expanded, neutral atoms began to form in a process called recombination. As this was occurring, the mean free path of the photons increased, due to less scattering. Eventually, at some point, photons no longer scattered with the baryons. This process, decoupling, allows the photons to propagate freely, hence making the Universe transparent to electromagnetic radiation for the first time ever. As they traverse through the Universe, the photons get redshifted from a temperature of 3000 K to the microwave band at present. These microwave photons are the earliest radiation which we can observe, and are referred to as the CMB, also called the surface of last scattering.

Decoupling caused the Universe to become transparent to light. However, there were no luminous sources yet. The period between decoupling and the "first light" is called the dark ages, and lasted about 400 million years. With the absence of structures, the physics of the universe during the dark ages was relatively simple since cosmic evolution followed linear perturbation theory.

As baryons were no longer coupled to radiation, they could fall into the potential wells of dark matter haloes. Clouds of hydrogen gas formed as a result of these denser regions. The timing of the birth of the first stellar objects is still unknown and a subject of research, but is of the order of a few hundred million years, and would have marked the end of the dark ages. It is thought that the first stars, Population III (Pop III) stars,

formed from these clouds. Unlike stars today, Pop III stars contained no metals, but are responsible for producing the first atoms of heavy elements in the Universe and may have had a contribution to reionisation.

As larger luminous structures formed hierarchically, there was more radiation in the universe. The intense radiation they emitted was energetic enough to ionise the neutral hydrogen in their environments. This period is referred to as the epoch of reionisation (EoR). As photons of energy 13.6 eV or higher are required to ionise neutral hydrogen, these objects had to have produced radiation with wavelength 91.2 nm (UV) or shorter. The process of reionising the universe is not instantaneous. At first, the mean free path of ionising photons is short due to dense clouds of neutral hydrogen around haloes. As these slowly ionise, photons can travel further and ionise more distant gas. This results in bubbles of ionised hydrogen forming around radiation sources. Eventually, these bubbles grow and overlap, leaving dense regions of neutral hydrogen which ultimately ionise. The Universe is once again transparent as the mean free path of photons is increased.

Our knowledge of the EoR is still limited. For instance, we do not know the precise time that it started or ended, although quasar (or quasi-stellar object; QSO) absorption spectra suggest it ended late, approximately at $z \gtrsim 6$. Another uncertainty about this epoch is what were the major ionising sources (e.g. galaxies, quasars, Pop III stars).

Beyond this era, galaxies continued to evolve and merge, stars recycled the elements formed by supernova explosions, and the largest cosmic structures formed: galactic clusters. Gravity attracts galaxies together, forming groups (of mass $\sim 10^{13}$ $M_\odot$) and clusters (of mass $> 10^{13}$ $M_\odot$).

1.4 The Epoch of Reionisation

The EoR was the second phase change of the universe, the first being recombination. As luminous sources (e.g. first generation Pop III stars, second generation Population II (Pop II) stars, X-ray binaries, quasars, etc.) formed, their radiation ionised the hydrogen, shifting the IGM from a neutral state to an ionised plasma. Due to the emission of ionising radiation from these sources, the dense neutral regions around them began to ionise. These bubbles of ionised (mainly hydrogen) gas grow as the ionisation fronts of radiation extend outwards. The IGM then contains patchy areas of ionised hydrogen which continue to grow as more luminous sources form. Eventually, the ionised bubbles overlap and the IGM rapidly ionises (Barkana and Loeb, 2001; Loeb and Barkana, 2001; Bromm and Larson, 2004; Ciardi and Ferrara, 2005; Choudhury and Ferrara, 2006; Furlanetto et al.,

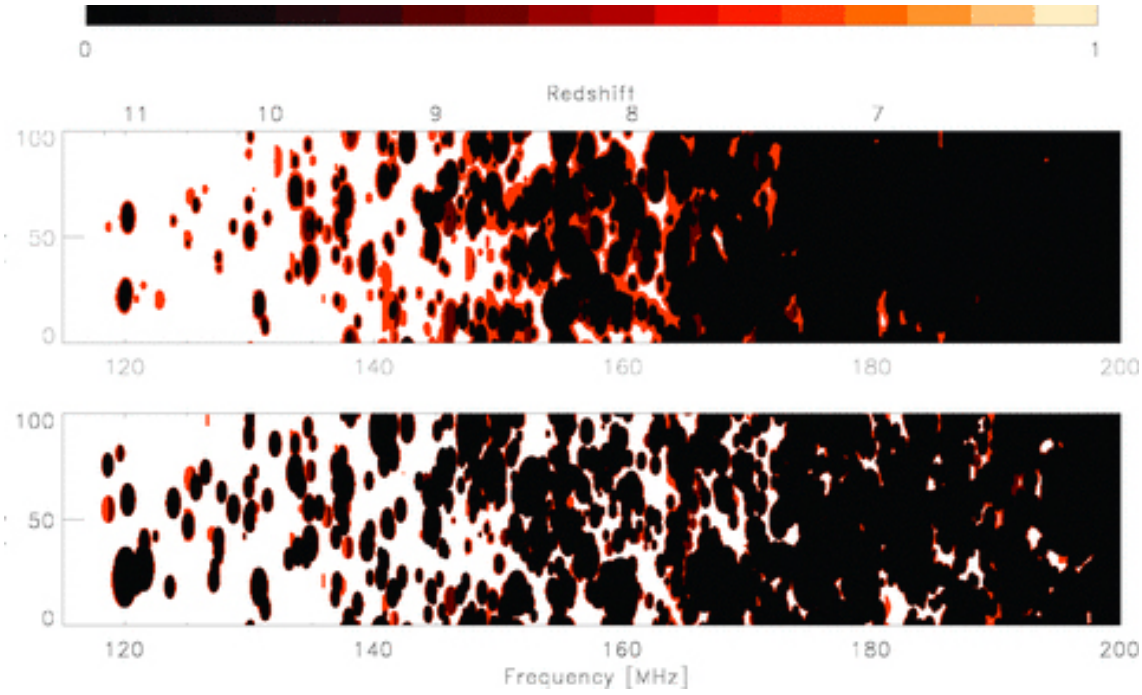

Figure 1.4: A slice through redshift of the neutral hydrogen fraction from a simulation of the EoR. Dark regions represent the ionised gas, white areas show the neutral hydrogen, and the red regions represent partially ionised gas. The plots show results for reionisation driven by quasars (*top*) and stars (*bottom*) (Thomas et al., 2009).

2006; Morales and Wyithe, 2010; Zaroubi, 2013).

Figure 1.4 shows a slice through redshift of two simulations of the EoR (Thomas et al., 2009). Neutral gas is represented as lighter regions, while ionised gas is dark. As time progresses (left to right), the dark ionised bubbles overlap until they ultimately dominate the universe. The last areas to ionise are dense neutral islands. The two slices show the effects of reionisation by quasars only (top panel) and stars only (bottom panel).

However, a lot is still unknown about this cosmic epoch. We have described an inside-out reionisation, where ionising sources ionise their immediate surroundings first before extending outwards into further regions of the IGM. The details of this scenario are yet to be clarified by observations. However, the overall process is supported by large cosmological simulations which are statistically representative of the universe (Iliev et al., 2006b; McQuinn et al., 2007; Trac and Cen, 2007; Iliev et al., 2014).

Another uncertainty is the nature of the ionising sources and the extent to which each type of source was responsible for the EoR. To determine this, we also need to understand how these objects form and how much ionising radiation they emit. The ionisation of the hydrogen atom requires photons with energy of at least 13.6 eV, such

as UV radiation. There are a number of candidates, spanning from quasars and stars to exotic processes like dark matter annihilation and decaying cosmic strings. Although studies have shown the possibility for these exotic processes to ionise neutral hydrogen, constraints on these objects suggest that they most likely were not the dominant ionisers (Chen and Kamionkowski, 2004; Pogosian and Vilenkin, 2004; Kasuya and Kawasaki, 2004; Padmanabhan and Finkbeiner, 2005; Mapelli and Ferrara, 2005; Mapelli et al., 2006; Zhang et al., 2006; Olum and Vilenkin, 2006; Ripamonti et al., 2007; Natarajan and Schwarz, 2010; Oldengott et al., 2016; Liu et al., 2016). There is also a significant amount of uncertainty with respect to the escape fraction of galaxies, $f_{\mathrm{esc},\star}$. This quantity refers to the fraction of ionising photons that escapes the galaxy and travels into the IGM. Constraining this number is imperative to fine-tuning simulations of the EoR. However, measuring the escape fraction from high-redshift galaxies is particularly difficult. Despite the limitations, observations have found its value to be in the range of 0.1 - 0.5 (Steidel et al., 2001; Giallongo et al., 2002; Inoue et al., 2005; Shapley et al., 2006; Iwata et al., 2009).

Quasars, which reside in the massive black holes at the centres of galaxies, produce large amounts of UV and X-rays. It is possible that these objects could have been responsible for the EoR (Meiksin and Madau, 1993; Meiksin, 2005; Giallongo et al., 2015; Puchwein et al., 2015). In fact, quasars have been observed at high redshifts, the furthest one being ULAS J1342+0928 at $z = 7.54$ (Bañados et al., 2018). Unfortunately, as their mass distribution at high redshifts is not known, their role in the EoR is still undetermined.

Another ionising source to consider is the hypothetical Pop III stars (Abel et al., 2002; Schaerer, 2002; Bromm et al., 2002; Bromm and Larson, 2004; Glover, 2005; Yoshida et al., 2003, 2012). These are thought to be the first generation of stars to have formed, and therefore consist of just hydrogen and helium, virtually lacking metals. As a result of their primordial chemical compositions, Pop III stars are expected to be massive ($\sim 100\ M_{\odot}$), extremely luminous and short-lived. The radiation produced by these early stars would have been able to ionise the IGM. However, since they have never been observed, their possible contribution to the EoR is not known (see review by Ciardi and Ferrara, 2005).

1.4.1 The Initial Mass Function

One important aspect we must examine when considering the feasibility of these sources for ionising the Universe is their photon production. In the case of stars, this is generally determined by the initial mass function (IMF), which describes the stellar mass distribu-

tion at birth, and the star formation history (SFH), which traces the evolution of stellar formation. As stars are formed when cold, dense gas clouds fragment and collapse, their formation is thus determined by the physical state of the gas. This, in turn, determines the masses of the stars which may form from such clouds. Consequently, the IMF holds a wealth of information about the properties of stellar populations and their environments. It also influences the radiative processes and chemical enrichment within the host galaxy. Thus, the IMF and the SFH determine how galaxies may evolve.

Salpeter (1955) first measured the IMF from the luminosity distribution of nearby stars. While he described the IMF as a power law, $\mathrm{d}N \propto M^{-\alpha}\,\mathrm{d}M$ with $\alpha = 2.35$, over the masses $0.4\ \mathrm{M}_\odot \lesssim M \lesssim 10\ \mathrm{M}_\odot$, subsequent studies (e.g. Miller and Scalo, 1979; Scalo, 1986; Kroupa et al., 1993) have found that, at the lowest masses, this does not hold. For masses $M \lesssim 0.5\ \mathrm{M}_\odot$, the IMF has a flatter slope. As a result, the IMF has three different mass ranges, over which its shape changes. At high masses, it follows the power law relation, with $\alpha \approx 2.3 - 2.4$. At the characteristic mass, $0.1\ \mathrm{M}_\odot \lesssim M \lesssim 1\ \mathrm{M}_\odot$, there is a peak or change in slope. Below this characteristic mass, the slope is flatter, but is less constrained due to the low luminosities of low-mass stellar objects. Figure 1.5 shows the Salpeter IMF along with other variations as determined by more recent studies (Offner et al., 2014).

However, whether the IMF is constant, or varies with environment or over cosmic time, is much debated. For instance, observations of field stars have shown the IMF having a steeper slope at high masses, as compared to stellar clusters. Additionally, at higher redshifts, we expect there to be more high-mass stars, which would indicate a top-heavy IMF, i.e. a steeper slope (Davé, 2008). As the IMF describes the mass distribution of stars, it is essentially a statistical measure, which cannot be directly observed; and observational limitations make it difficult to obtain its true shape across all masses. Limitations in detecting distant or low-luminosity stellar objects, as well as the fact that stars are continuously forming and dying, make it impossible to ever capture the full ensemble of stellar masses in our universe. Nevertheless, it is generally assumed that the IMF is non-varying and universal. For more insight into variations of the IMF, we direct the reader to the review by Bastian et al. (2010).

The shape of the IMF, thus, determines the distribution of stars and their masses. As the relationship between a star's rate of (hydrogen) ionising photon production and its mass is supra-linear, the shape of the IMF can drastically affect the rate of hydrogen ionisation (see e.g. Tumlinson and Shull, 2000; Bromm et al., 2001; Schaerer, 2002; Tum-

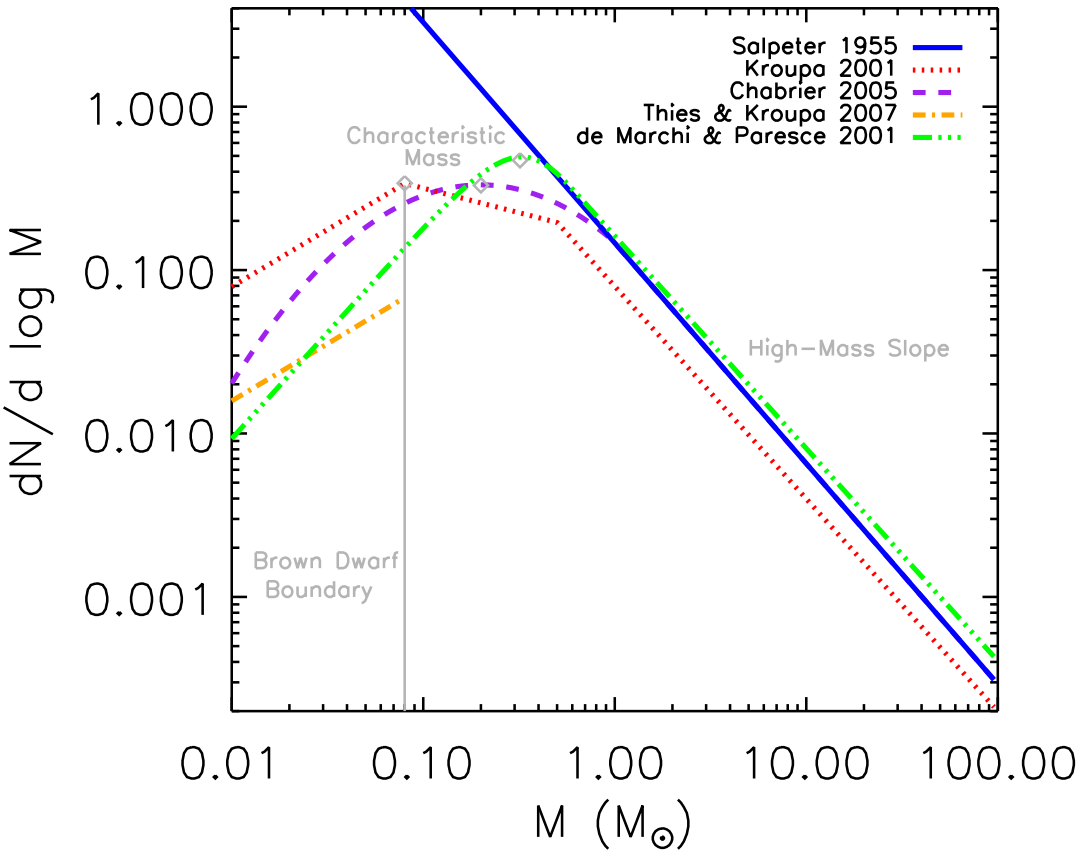

Figure 1.5: Forms of the IMF as proposed by various studies (Salpeter, 1955; Kroupa, 2001; de Marchi and Paresce, 2001; Chabrier, 2003; Thies and Kroupa, 2007) using galactic stellar data (Offner et al., 2014).

linson et al., 2004). Hence, the rate at which reionisation proceeds is especially sensitive to the assumed IMF shape, with a more massive stellar population producing substantially more ionising photons than a population of mostly lower-mass stars. Galaxies comprising of more massive stars would thus emit more ionising photons into the IGM, increasing the photoionisation rate, and resulting in reionisation ending earlier. Hence, the timing and progression of the EoR are fundamentally linked to the IMF slope, which describes the number of massive stars formed.

In addition to the IMF shape, the metallicity of these early stars also affects the number of ionising photons which they produce. Low-metallicity stars (such as Pop III stars) produce more ionising photons per stellar mass than metal-enriched stars. In the absence of metals, stars have a reduced rate of CNO burning. Instead, their energy production is derived from inefficient proton-proton burning in their contracted, hotter ($> 10^8$ K) cores which are required to prevent these massive stars from gravitational collapse. As a result, low-metallicity stars have higher surface temperatures and ionising photon production. The combined effects of the IMF slope and stellar metallicity on the ionising photons produced, and hence the EoR, is demonstrated in Figure 1.6 (Chary, 2008), which shows that steeper slopes and higher metallicity result in lower ionising photon emission.

Hence, the characteristics of the first stars strongly determine how the EoR proceeds. The form of the IMF at high redshifts indicates whether the EoR was driven by Pop II, Pop III, or a combination of stellar types. For more detailed discussions on the stellar IMF, we refer the reader to the reviews by Elmegreen (2009); Bastian et al. (2010); Kroupa et al. (2013); Krumholz (2014); Offner et al. (2014); Hopkins (2018). For more on the early stars and the IMF at the EoR, we refer the reader to Tumlinson and Shull (2000); Tumlinson et al. (2004); Bromm et al. (2001); Schaerer (2002); Chary (2008); Norman (2008); Topping and Shull (2015); Salvador-Solé et al. (2016); Windhorst et al. (2018).

1.4.2 Observational Constraints

Despite these unknowns, we have been able to place constraints on the EoR. The following are some of the mechanisms which we use to do so.

Lyman-α Forest

The Lyman-α (Lyα) forest is an absorption phenomenon occurring in the spectra of background QSOs. Neutral hydrogen residing in the lines of sight of distant QSOs absorb photons emitted by the QSOs at the UV resonance line frequency of 1215.67 Å. In an

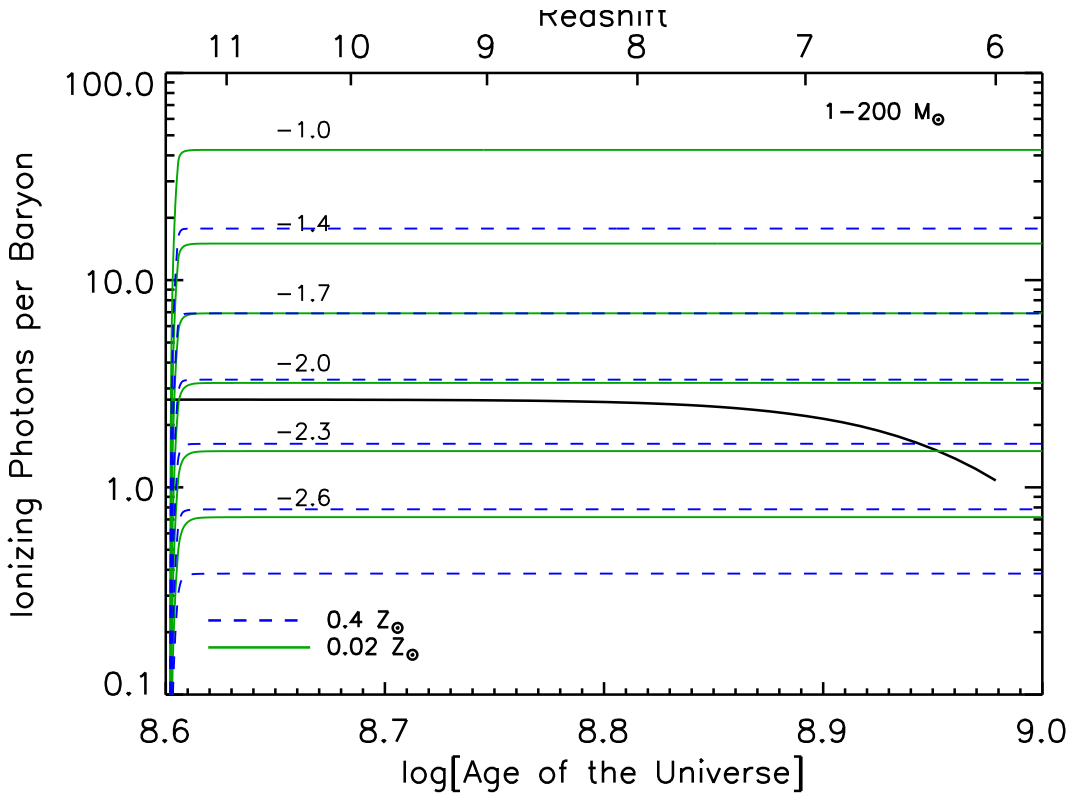

Figure 1.6: Number of ionising photons produced per baryon for non-Salpeter IMFs with a range of slopes ($\alpha = -1.0, -1.4, -1.7, -2.0, -2.3, -2.6$), and spanning masses $1 - 200$ $M_{\odot}$. The solid green line shows the ionising photons for low-metallicity stars, while the dashed blue line shows those for metal-enriched stars. The black solid line represents the minimum number of ionising photons needed for ionising the IGM and accounting for recombinations between the redshift and $z \sim 6$. The EoR is completed when the plots cross the solid black line (Chary, 2008).

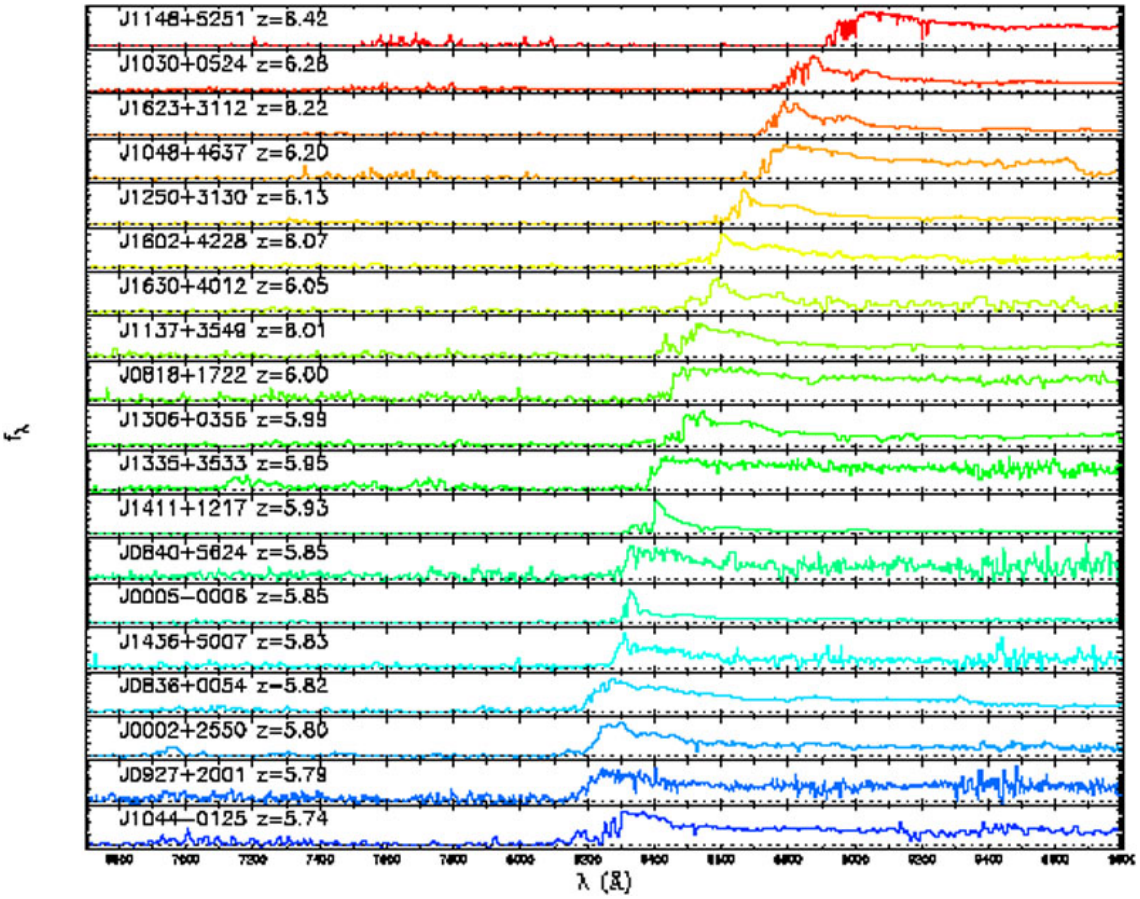

Figure 1.7: Spectra of high-redshift SDSS quasars. The Gunn-Peterson trough is shifted to higher wavelengths with increasing redshifts, indicating an increase in the ionisation fraction with redshift (Fan et al., 2006).

expanding universe, homogeneously filled with gas, the redshifted Lyα line will produce an absorption trough due to neutral hydrogen blueward of the QSOs Lyα emission line (Gunn and Peterson, 1965; Scheuer, 1965; Shklovskii, 1965). This trough is called the Gunn-Peterson trough after Gunn and Peterson (1965) found such an occurrence of reduced flux in the spectrum of a QSO and used it to place upper limits on the amount of HI in the IGM. The large cross-section of the Lyα absorption makes this method very powerful for studying gas in the IGM. Figure 1.7 shows the spectra of 19 high-redshift QSOs from the Sloan Digital Sky Survey (SDSS)[2] where the Gunn-Peterson trough can be seen (Fan et al., 2006).

The Lyα forest is very sensitive to the HI column density, and hence to the neutral fraction as function of redshift along the line of sight. The optical depth for absorption of a Lyα photon, τ_α, is related to the probability of the photon's transmission, $e^{-\tau_\alpha}$, and is

[2] https://www.sdss.org/

given by

$$\tau_\alpha = \int_0^{z_{\rm QSO}} \sigma_\alpha n_{\rm HI} \frac{c\,{\rm d}z}{(1+z)\,H_0\sqrt{\Omega_{\rm m}\,(1+z)^3+\Omega_\Lambda}}, \tag{1.16}$$

where the integral has limits from present ($z = 0$) to the redshift of the QSO ($z_{\rm QSO}$), and $\sigma_\alpha(\nu)$ is the cross-section of the Lyα absorption which is a function of the photon frequency, ν. Evaluating this integral gives the following expression for the neutral fraction:

$$x_{\rm HI} = \frac{n_{\rm HI}}{n_{\rm H}} \approx 10^{-4}\tau_\alpha h\sqrt{\Omega_{\rm m}\,(1+z)^3}. \tag{1.17}$$

As a result, observations of the Lyα forest have been used to constrain the end of reionisation to $z \gtrsim 6$. For reviews of the Lyα forest, we direct the reader to Rauch (1998); Weinberg et al. (2003); Morales and Wyithe (2010).

The 21 cm Line

The 21 cm line originates from the hyperfine splitting of the $1s$ ground state of the hydrogen atom. The electron experiences a spin flip, alternating between having an up or down spin. Since both electron and proton spins have a value of $\frac{\hbar}{2}$, their sum, the total spin angular momentum, can be either 0 (parallel spins) or 1 (antiparallel spins). The latter exists at a slightly higher energy level than the former. The difference between these energy levels is 5.9×10^6 eV, with frequency 1420.4 MHz and wavelength 21.106 cm. The transition from the triplet (antiparallel) state to the singlet (parallel) state is classically forbidden. The probability for a spontaneous transition is given by the Einstein A coefficient, $A_{10} = 2.85 \times 10^{-15}$ s^{-1}, which translates to a lifetime of 1.1×10^7 years for the triplet state. However, despite its low decay rate, the vast abundance of hydrogen in the universe makes the 21 cm transition line an important observational tool.

In radio astronomy, it is conventional to use the brightness temperature, $T_{\rm b}$, of a source, rather than its specific intensity (or brightness), I_ν. The brightness temperature is defined as the corresponding temperature of a blackbody radiator, with spectral distribution, B_ν, of the same brightness, so that $B_\nu(T_{\rm b}) = I_\nu$. Due to the range of frequencies and temperatures which are of importance in 21 cm astronomy, the Rayleigh-Jeans limit is a suitable approximation to the spectral distribution, so that $T_{\rm b} \approx \frac{c^2}{2k_{\rm B}\nu^2} I_\nu$. It is therefore convenient to use the hydrogen spin temperature, $T_{\rm s}$, in this context. The spin temperature indicates the relative number densities of hydrogen atoms in the triplet and singlet states (n_1 and n_0, respectively):

$$\frac{n_1}{n_0} = 3{\rm e}^{-\frac{T_{21}}{T_{\rm s}}}, \tag{1.18}$$

where $T_{21} = 0.0681$ K is the temperature corresponding to the 21 cm wavelength. Three mechanisms compete to set T_s: absorption and emission of CMB photons, collisions with free electrons, protons and other hydrogen atoms, and scattering of Lyα photons via excitation and de-excitation (Wouthuysen, 1952; Field, 1958). Thus, the spin temperature can be expressed as:

$$T_\mathrm{s} = \frac{T_\mathrm{CMB} + y_\mathrm{k} T_\mathrm{k} + y_\alpha T_\alpha}{1 + y_\mathrm{k} + y_\alpha}, \tag{1.19}$$

where T_CMB denotes the temperature of the CMB, T_k is the gas kinetic temperature, T_α is the temperature of ambient Lyα photons, and y_k and y_α are the kinetic and Lyα coupling terms, respectively (Field, 1958). Since collisions and Lyα photons break the coupling between T_s and T_CMB, neutral hydrogen can be observed against the CMB. Thus, the brightness temperature becomes

$$T_\mathrm{b} = T_\mathrm{s} \left(1 - \mathrm{e}^{-\tau_{21}}\right) + T_\mathrm{CMB} \mathrm{e}^{-\tau_{21}}, \tag{1.20}$$

where $\tau_{21} = \int \sigma_{21} n_0 \left(1 - \mathrm{e}^{-\frac{T_{21}}{T_\mathrm{s}}}\right) \mathrm{d}l$ is the optical depth of an HI cloud, with σ_{21} the 21 cm line absorption cross-section. Here, the factor $(1 - \mathrm{e}^{-\tau_{21}})$ gives the emission probability of 21 cm photons from within the HI cloud while the factor $\mathrm{e}^{-\tau_{21}}$ gives the transmission probability of the CMB photons. The observable differential brightness temperature can then be defined as:

$$\delta T_\mathrm{b} = \frac{T_\mathrm{s} - T_\mathrm{CMB}}{1 + z} \left(1 - \mathrm{e}^{-\tau_{21}}\right). \tag{1.21}$$

Different observed frequencies translate to different redshifts, enabling us to probe the 3D distribution of neutral hydrogen in the universe during the EoR and dark ages.

Already, we have been able to measure this signal from the EoR and cosmic dawn and place constraints on the 21 cm power spectrum from these epochs from the LOw Frequency ARray (LOFAR; van Haarlem et al., 2013)[3] data (Patil et al., 2017; Gehlot et al., 2019). The upcoming Square Kilometre Array (SKA)[4] will be able to place even tighter constraints on the evolution of the neutral hydrogen in the universe (Mellema et al., 2013; Koopmans et al., 2015; Weltman et al., 2018). Simulations predicting these results are essential and illustrate the quality of data which will be obtainable by the SKA (see e.g. Mellema et al., 2006; Semelin et al., 2007; Ciardi et al., 2015; Semelin, 2016; Ross et al., 2017, 2019). We direct the reader to Furlanetto et al. (2006) and Pritchard and Loeb (2012) for detailed reviews of 21 cm cosmology.

[3] http://www.lofar.org/

[4] https://www.skatelescope.org/

Thomson Scattering Optical Depth of the CMB

As the universe transitions from a neutral state to an ionised one, the number density of free electrons in the IGM increases. This, in turn, leads to a higher probability that CMB photons will Thomson scatter off these electrons. The likelihood of this occurring is related to the effective optical depth to reionisation,

$$\tau = \int_0^{z_{\rm dec}} \sigma_{\rm T} n_{\rm e} \frac{c\,{\rm d}z}{(1+z)\,H_0\sqrt{\Omega_{\rm m}\,(1+z)^3 + \Omega_\Lambda}}, \tag{1.22}$$

where the integral has limits from present ($z = 0$) to decoupling ($z = z_{\rm dec}$), and $\sigma_{\rm T}$ is the Thomson scattering cross-section. The majority of the electrons come from HII and HeII. The contribution from HeIII at low redshift is only a few percent of the total optical depth. This equation holds for the optical depth along each line of sight and also for the mean electron number density, i.e. the mean optical depth. As the integral is over redshift, the optical depth is insensitive to the evolution of the ionisation fraction. Nevertheless, its value can constrain the approximate end redshift of the EoR. For an EoR which is completed early, the column depth of free electrons increases, and so too will the mean optical depth. The latest constraint on the optical depth is from the Planck survey, with $\tau = 0.054 \pm 0.007$, corresponding to a mid-point EoR redshift of $z_{\rm reion} = 7.7 \pm 0.7$ (Planck Collaboration et al., 2018a).

CMB temperature fluctuations are suppressed on scales smaller than the horizon size at the EoR by the optical depth. The probability of this dampening is proportional to $\mathrm{e}^{-2\tau}$. In addition to this, the EoR is responsible for linearly polarising the CMB on the quadrupole scale. This signal has a peak on scales larger than the horizon size at EoR, and its amplitude is proportional to τ. Measuring this "reionisation bump", although a direct probe of the optical depth to the EoR, is limited by the cosmic variance on large scales (Holder et al., 2003; Lewis et al., 2006; Mortonson and Hu, 2008).

Kinetic Sunyaev-Zel'dovich Effect

The second observable feature of the CMB by the EoR is the kinetic Sunyaev-Zel'dovich effect. However, we will postpone going into this in detail until the next section (Section 1.5), where we describe the Sunyaev-Zel'dovich effect more thoroughly.

1.5 The Sunyaev-Zel'dovich Effect

After last scattering, CMB photons have a mean free path of the Hubble distance. However, as they propagate through the universe, a fraction of them interact with matter along

their way to us. These interactions give rise to the secondary anisotropies of the CMB. In contrast, the primary anisotropies are caused by primordial density fluctuations which were imprinted onto the CMB when matter and radiation were coupled. On large scales, the primary anisotropies dominate the CMB power spectrum. Secondary anisotropies take over on smaller scales. Some of these interactions include the integrated Sachs-Wolfe (ISW) effect (Sachs and Wolfe, 1967), gravitational lensing, polarisation, Thomson scattering, and the Sunyaev-Zel'dovich (SZ) effect (Sunyaev and Zeldovich, 1972, 1980a,b). This thesis focuses on the last effect and its signal from the EoR. For a recent review of the CMB processes and measurements, we direct the reader to Staggs et al. (2018).

The SZ effect arises from the inverse Compton scattering of CMB photons by free energetic electrons. While electrons at rest will produce scatter, the net effect of this cancels out since the number of photons being scattered in each direction is the same. Electrons in motion, however, will produce an overall directional scattering. When CMB photons travel through a cloud of free electrons, the probability that they will scatter is dictated by the optical depth,

$$\tau_{\rm e} = \sigma_{\rm T} \int n_{\rm e}\ {\rm d}l \sim 2 \times 10^{-3} \left(\frac{n_{\rm e}}{10^{-3}\ {\rm cm}^{-3}}\right) \left(\frac{l}{\rm Mpc}\right), \tag{1.23}$$

where the integral is performed over the line-of-sight, $n_{\rm e}$ is the electron number density of the gas, and the values denoted are typical for galaxy clusters, where the SZ effect is commonly observed. Although inverse Compton scattering occurs in a variety of scenarios, the SZ effect refers to the scattering of CMB photons in the GHz to THz range of frequencies by non- or mildly relativistic electrons.

There are two broad types of SZ effect which are essentially determined by the nature of the electron energies. These can be either thermal or kinetic, where the electrons are energetic due to their thermal state or their velocities, respectively. The thermal SZ (tSZ) effect is most noticeably caused when CMB photons are scattered by the hot electrons in galactic clusters whose intra-cluster plasma reach temperatures of 10^7 - 10^8 K. The kinetic SZ (kSZ) effect arises when CMB photons are scattered due to the bulk motion of the electrons in the cluster relative to the photons. In addition to these, electrons with relativistic speeds require relativistic corrections to be taken into account, leading to a relativistic SZ (rSZ) effect. Lastly, a non-thermal SZ (ntSZ) effect is also possible, and arises from non-thermal velocity distributions (e.g. AGN outflows and magnetic fields). The different types of SZ effect all have varying spatial and spectral dependencies due to the physics and astrophysical processes which affect them. As such, they can act as probes of differing astrophysics and cosmological effects. For reviews of the SZ effect, we

direct the reader to Birkinshaw (1999); Rephaeli (1995); Carlstrom et al. (2002); Kitayama (2014); Mroczkowski et al. (2019).

1.5.1 The Kinetic Sunyaev-Zel'dovich Effect

The kSZ effect arises when CMB photons experience a Doppler shift by the bulk velocity of electrons in the universe. This has the result of slightly changing the temperature of the scattered photons, with the temperature shift scaling as $\frac{v}{c} n_{\rm e}$, where v and $n_{\rm e}$ are the line of sight bulk velocity and number density of the electrons. If the ionised gas has motion directed towards the observer, the temperature of the CMB appears hotter, while for ionised gas moving away from the observer, the temperature appears colder.

The kSZ Effect as a Probe of the EoR

The kSZ signal is divided into two components: the homogeneous kSZ signal which is caused by perturbations in the density of the fully ionised universe, and the patchy kSZ signal which is caused by perturbations in the ionisation fraction during the EoR. The amplitude and shape of the latter depends on the duration of the EoR and the distribution of ionised bubble sizes, respectively. These features also have a weak dependence on the average redshift of the EoR. This can be explained qualitatively as the power of the signal being linearly proportional to the number of bubbles along the line of sight. The abundance of bubbles scales with the duration of the EoR. Also, with larger bubbles, the power peaks at larger scales, and vice versa. If the EoR occurs early, when the universe is denser, and lasts for the same duration, this will lead to higher kSZ power. The temperature fluctuation corresponding to the EoR is given by

$$\frac{\Delta T_{\rm CMB}}{T_{\rm CMB}} = \frac{\sigma_{\rm T}}{c} \int n_{\rm e} {\rm e}^{-\tau} \left(\hat{\boldsymbol{n}} \cdot \boldsymbol{v}\right) a \, {\rm d}\eta, \tag{1.24}$$

where $\tau(\eta)$ is the optical depth to Thomson scattering, $\hat{\boldsymbol{n}}$ is the line of sight unit vector, $\boldsymbol{v}$ is the peculiar velocity of the electron cloud, a is the scale factor, and the integral is calculated over the conformal time.

Perfectly homogeneous ionising sources in the EoR can reionise the universe without producing a kSZ effect. On the other hand, inhomogeneous, patchy reionisation will give rise to kSZ power. However, disinguishing between these two scenarios has proved to be non-trivial since they both have the same spectral dependence and similar angular dependencies. There is a large body of literature investigating the kSZ effect arising from the EoR (see e.g. Gruzinov and Hu, 1998; Knox et al., 1998; Santos et al., 2003; Zhang

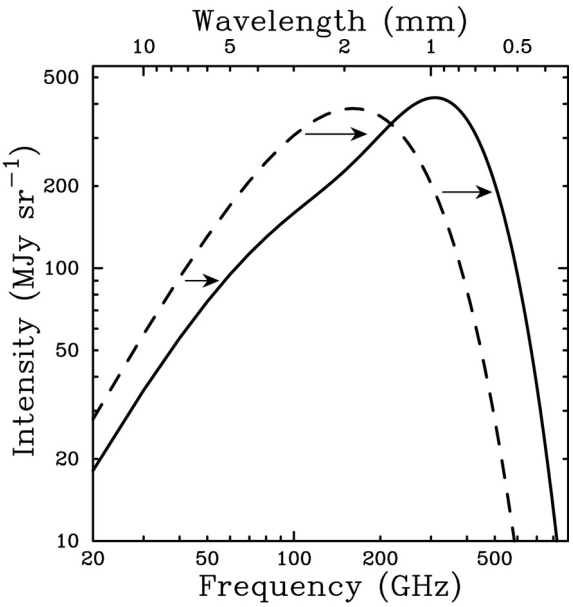

Figure 1.8: The blackbody spectrum of the CMB (dashed line) is shifted to higher frequencies (solid line) via the tSZ effect. The distortion shown here is exaggerated in order to illustrate the effect, for a cluster 1000 times the typical mass of a galaxy cluster. Below 218 GHz, the intensity of the CMB is decreased, and above 218 GHz, the CMB intensity is increased (Carlstrom et al., 2002).

et al., 2004a; Zahn et al., 2005; McQuinn et al., 2005; Iliev et al., 2007, 2008; Mesinger et al., 2012; Zahn et al., 2012; Park et al., 2013; Battaglia et al., 2013a; Calabrese et al., 2014; Park et al., 2016; Alvarez, 2016; Ma et al., 2018).

1.5.2 The Thermal Sunyaev-Zel'dovich Effect

When CMB photons pass through the hot intra-cluster medium (ICM) of a galaxy cluster, there is a $\sim 1\%$ chance that it will interact with one of the energetic electrons in the plasma. The scattered photon experiences an energy boost of $\sim 4\frac{k_{\rm B}T_{\rm e}}{mec^2}$ (see e.g. Rybicki and Lightman, 1979; Sazonov and Sunyaev, 2000). This causes a shift in the CMB spectrum from the low-frequency region to higher frequencies (see Figure 1.8).

The distortion in CMB intensity is given by

$$\Delta I_\nu \approx I_0 y \frac{x^4 \mathrm{e}^x}{(\mathrm{e}^x-1)^2}\left(x\frac{\mathrm{e}^x+1}{\mathrm{e}^x-1}-4\right) \equiv I_0 y g(x), \tag{1.25}$$

where $x = \frac{h_{\rm P}\nu}{k_{\rm B}T_{\rm CMB}} \approx \frac{\nu}{56.8\ \mathrm{GHz}}$ is the dimensionless frequency, y is the Compton y-parameter (defined later), and

$$I_0 = \frac{2\left(k_{\rm B}T_{\rm CMB}\right)^3}{\left(h_{\rm P}c\right)^2} = 270.33\left(\frac{T_{\rm CMB}}{2.73\ \mathrm{K}}\right)^3\ \mathrm{MJy\ sr^{-1}}. \tag{1.26}$$

If $\frac{\Delta I_\nu}{I_\nu} \ll 1$, the signal can be expressed in terms of the CMB temperature, using the derivative of the Planck function with respect to temperature:

$$\frac{\Delta T_{\rm CMB}}{T_{\rm CMB}} \approx y \left(x \frac{{\rm e}^x + 1}{{\rm e}^x - 1} - 4 \right) = y f(x), \tag{1.27}$$

where $f(x)$ is the frequency dependence of the tSZ spectrum in terms of $\Delta T_{\rm CMB}$. When there are electrons with energies in the relativistic regime, a factor $\delta_{\rm SZ}(x, T{\rm e})$ is incorporated, and $f(x)$ becomes

$$f(x) = \left(x \frac{{\rm e}^x + 1}{{\rm e}^x - 1} - 4 \right) \left(1 + \delta_{\rm SZ} \left(x, T{\rm e} \right) \right). \tag{1.28}$$

For more detailed interpretations of the relativistic corrections to the tSZ effect, see Challinor and Lasenby (1998); Nozawa et al. (2006); Chluba et al. (2013). In the non-relativistic and Rayleigh-Jeans limit, $f(x \ll 1) \to -2$, while at high frequencies, $f(x \gg 1) \to x - 4$. The frequency dependence of ΔI_ν is shown in Figure 1.9.

The spectral signature of the tSZ can be separated from the kSZ effect, whose peak is near the null of the tSZ effect, and other temperature fluctuations due to its frequency dependence. Hence, multi-frequency measurements are necessary to distinguish them. Additionally, the tSZ signal dominates over the kSZ effect roughly by an order of magnitude for clusters. This is due to the thermal velocity of electrons ($\sim 10^4$ km s^{-1}) being much higher than the bulk velocity ($\lesssim 10^3$ km s^{-1}).

We can see from Equation 1.27 that the change in the CMB temperature is proportional to the Compton y-parameter. This quantity can therefore be used to measure the magnitude of the tSZ signal. It is defined as the line of sight integral of the electron pressure,

$$y \equiv \frac{k_{\rm B}}{m_{\rm e} c^2} \int T_{\rm e} \, {\rm d}\tau_{\rm e} = \frac{k_{\rm B} \sigma_{\rm T}}{m_{\rm e} c^2} \int n_{\rm e} T_{\rm e} \, {\rm d}l = \frac{\sigma_{\rm T}}{m_{\rm e} c^2} \int p_{\rm e} \, {\rm d}l, \tag{1.29}$$

where $T_{\rm e}$ is the temperature of the electrons, and $p_{\rm e}$ is the pressure due to the electrons. It is important to note that, as the Compton y-parameter is an integral over the line of sight, it is redshift independent. This can also be explained by considering that $\Delta T_{\rm CMB}$ (and ΔI_ν) is redshifted the same way as $T_{\rm CMB}$ (and I_ν). Hence, the tSZ effect does not experience a loss in intensity with redshift (dimming), making it a useful tool for measuring large-scale structure in the universe. The ICM of typical clusters have electron temperatures of 5 - 10 keV. For massive clusters with central optical depth $\sim 10^{-2}$, $y \sim 10^{-4}$. More generally, the y-parameter for clusters is typically $y \gtrsim 10^{-5}$.

Integrating over the solid angle of a galaxy cluster allows for a temperature-weighted estimate of the number of electrons in the cluster to be calculated. Thus, the thermal

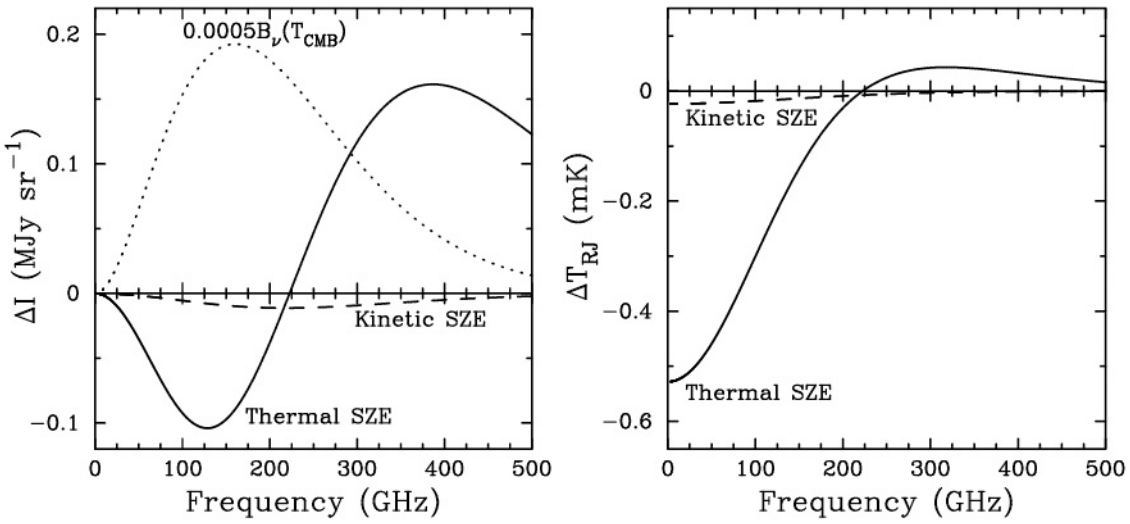

Figure 1.9: The spectral distortion of the CMB by the tSZ (solid line) and kSZ (dashed line) effects. The SZ effect is calculated for a realistic massive cluster with $T_\mathrm{e} = 10$ keV, $y = 10^{-4}$ and peculiar velocity of 500 km s^{-1}. The spectrum is plotted in units of intensity (*left*) and Rayleigh-Jeans brightness temperature (*right*). The dotted line is the CMB blackbody spectrum scaled by 5×10^{-4} and is shown for comparison (Carlstrom et al., 2002).

energy of the cluster can be measured. This solid angle integral is given by

$$\int \Delta T_\mathrm{CMB}\ \mathrm{d}\Omega \propto \frac{N_\mathrm{e}\,\langle T_\mathrm{e}\rangle}{D_\mathrm{A}^2} \propto \frac{M\,\langle T_\mathrm{e}\rangle}{D_\mathrm{A}^2}, \tag{1.30}$$

where $\mathrm{d}\Omega = \frac{\mathrm{d}A}{D_\mathrm{A}^2}$ is the solid angle segment, D_A is the angular diameter distance, N_e is the total number of electrons in the cluster, $\langle T_\mathrm{e}\rangle$ is the average temperature of the electrons, and M is the mass of the cluster. Here, the cluster mass can be either the gas mass or total mass since $M_\mathrm{gas} = f_\mathrm{g} M_\mathrm{total}$, where f_g is the gas mas fraction. Although the integrated tSZ flux is dependent on the angular diameter distance of the cluster, D_A changes slowly with redshift, especially at higher z. In addition to this, at higher redshifts, clusters are denser and hotter ($\Omega_\mathrm{m} \propto (1+z)^3$), enabling SZ surveys to detect galaxy clusters above a given mass limit without redshift having a significant impact.

In practice, all clusters above a mass cutoff in a given area of sky can be detected with the tSZ effect using CMB frequency maps of the y-parameter. Their redshifts can then be estimated using optical data. Finally, their mass can be calculated with X-ray observations, the galaxy velocity dispersion or weak lensing.

In addition to y-parameter maps, the angular power spectra of the tSZ signal is also a useful measurement. Komatsu and Seljak (2002) found that the tSZ angular power spectrum is cosmology dependent, with $D_l \propto \sigma_8^7 \Omega_\mathrm{b}^2 h^2$. However, more recently, Shaw

et al. (2010) have shown

$$D_l \propto \sigma_8^{8.3} \Omega_{\rm b}^{2.8} h^{1.7}. \tag{1.31}$$

This dependence makes the power spectrum of the tSZ signal a powerful tool for constraining these cosmological parameters (see e.g. Barbosa et al., 1996; Sievers et al., 2013; Crawford et al., 2014; Hill et al., 2014; George et al., 2015; Planck Collaboration et al., 2015; Horowitz and Seljak, 2017). The tSZ power spectrum is also affected by astrophysical processes, such as AGN feedback, shock heating, radiative cooling, etc. Komatsu and Seljak (2002); Battaglia et al. (2010); Sehgal et al. (2010); Shaw et al. (2010); Trac et al. (2011) have produced templates for the tSZ power spectrum, fitted for WMAP ΛCDM cosmology, while probing its dependence on cosmological and astrophysical effects.

While these studies investigate the tSZ signal in the context of galaxy clusters, the purpose of this thesis is to determine the tSZ effect arising from the EoR. For such a goal, it is more appropriate to consider the mean value of the y-parameter, $\langle y \rangle$. The tightest constraint on this measurement was done by the COBE-FIRAS experiment and found $\langle y \rangle < 1.5 \times 10^{-5}$ at the 95% confidence level (Fixsen et al., 1996).

Refregier et al. (2000) performed hydrodynamic simulations comprising only gravitational forces (with no star formation) as well as analytic calculations with the Press-Schechter (PS) formalism (Press and Schechter, 1974) to compute the tSZ signal. For ΛCDM cosmology, they found $\langle y \rangle = 1.67 \times 10^{-6}$ (simulation) and 2.11×10^{-6} (PS), both values being about an order of magnitude below the COBE-FIRAS upper limit. Their projected maps of the y-parameter showed clusters having $y > 10^{-5}$, and groups and filaments having $y \sim 10^{-7}$ - 10^{-5}. However, they note that projecting a number of simulation boxes along the line of sight on the sky would cause the filamentary objects to be averaged out (da Silva et al., 2001; Seljak et al., 2001). They also find that the majority of the tSZ signal arises from low redshifts ($z < 2$). Their angular power spectra show the tSZ effect having comparable power to the primary CMB at $l \sim 2,000$, while groups and filaments contributed $\sim 50\%$ of the power at $l = 500$ with $\sim 50\%$ of that power being produced at $z \lesssim 0.1$.

By combining hydrodynamic simulations and analytic models, Zhang et al. (2004b) estimated $\langle y \rangle = 2.6 \times 10^{-6} \left(\frac{\sigma_8}{0.84}\right)^{4.1-2\Omega_{\rm m}} \left(\frac{\Omega_{\rm m}}{0.268}\right)^{1.28-0.2\sigma_8}$ for a flat ΛCDM WMAP cosmology, with the dominant contribution coming from $z \sim 1$. More recently, Hill et al. (2015) used analytic calculations (including an ICM model (Hill et al., 2014), relativistic corrections (Arnaud et al., 2005) and a reionisation model (Battaglia et al., 2013b)) to compute the total mean Compton paramter of the universe. They found $\langle y \rangle_{\rm ICM} = 1.58 \times 10^{-6}$,

$\langle y \rangle_{\rm IGM} = 8.9 \times 10^{-8}$ and $\langle y \rangle_{\rm EoR} = 9.8 \times 10^{-8}$ for the contributions from the ICM, IGM and EoR, respectively, which gave a total mean value of $\langle y \rangle_{\rm total} = 1.77 \times 10^{-6}$. The signals from the IGM and EoR are sub-dominant to the ICM signal. However, an accurate measurement of $\langle y \rangle$ is crucial for providing constraints on galaxy formation models, feedback mechanisms and the thermal history of the universe.

To date, the tightest constraint on $\langle y \rangle$ is the COBE-FIRAS measurement. While the tSZ effect is very well understood, it is not traditionally applied to the EoR. Therefore, the EoR contribution to the global tSZ effect is not well constrained. Conversely, there has been extensive research on the kSZ effect that arises during the EoR. Our study is the first of its kind where hybrid N-body and hydrodynamic simulations are used to calculate the EoR contribution to the tSZ effect. We do this by constructing maps of the Compton y-parameter, PDFs of the values of y in the IGM during EoR, and angular power spectra of the maps. It is our objective to contribute to the body of research that encompasses these topics by providing numerical simulation results.

Second Order Doppler Distortions

Zeldovich et al. (1972) showed that the spectral distortions produced by thermally energetic electrons give rise to a spectrum which can be described as a superposition of blackbodies with a Compton y-parameter, $y = \mathcal{O}(v^2)$. This y-parameter depends on the second order of the electron velocities, v, essentially making it the equivalent of a tSZ effect due to the bulk flow. Hu et al. (1994) investigated the significance of this quadratic Doppler distortion during the EoR. They showed that when this contribution to the y-parameter is included, Equation 1.29 becomes

$$y = \frac{\sigma_{\rm T}}{m_{\rm e} c^2} \int \left(\frac{1}{3} m_{\rm e} n_{\rm e} \left\langle v^2 \right\rangle + p_{\rm e} \right) \, {\rm d}l. \tag{1.32}$$

They also suggest that the bulk flow contribution would be dominated by the tSZ effect. According to their estimations which are based on a CDM cosmology with $\Omega_0 = 1$, that the contribution from the EoR would be $\sim 10^{-8}$.

1.6 Thesis Outline

In Chapter 2, we describe the numerical methods and simulation code used in this study. In Chapter 3, we outline out methodology. We begin by summarising the simulations used in our analyses, their reionisation histories, and parameters used to perform the runs. We then describe the procedure used to construct lightcones using the data from

our runs and how we obtain the Compton y-parameter from them. We present the results in Chapter 4 and discuss their significance. Finally, we conclude with a summary of the study, discussing the implications of our findings, and possibilities for further work on this topic in Chapter 5.

Chapter 2

Simulating the EoR

The EoR is still being understood. Despite the limitations in observational technology, simulations can shed a light on this cosmological era. By inputting the physics of gravitation, gas dynamics and radiative transfer into complex codes, we can replicate the reionisation of the universe, and thus gain a better understanding of the processes involved at the start and duration of this cosmic period.

In order to grasp a complete understanding of the processes involved during the EoR, simulations need to cover a large range of length scales (of orders of magnitude ~ 7 or larger!) and mass scales (of orders of magnitude ~ 16). The act of reionising the universe involves an interplay between ionisations and recombinations, where the former ultimately exceeds the latter. At small scales (of orders of kpc), there are galaxies and Lyman limit systems. These sources act as either sources or sinks of ionising radiation, respectively. On even smaller scales, we have stars. Fortunately, a thorough knowledge of stellar synthesis is often not required when designing simulations, as crude estimations often suffice. Simulation boxes also need to have a sufficiently large size in order to accurately represent the distribution of galaxies and ionisation bubbles (at least 100 Mpc), and include rare quasars (at least 100s of Mpc). In terms of mass scales, simulations need to range from the masses of stars and supernovae to halo masses. In practice, simulations can use stellar particles of fixed mass, representing multiple stars. Similarly, dark matter particles are modelled in this way. We direct the reader to Lidz (2016) for a review on the physics involved in modelling the EoR, Trac et al. (2011) for a review on simulating the EoR, and Bertschinger (1998) and Springel et al. (2006) for reviews on large-scale structure simulations.

N-body Algorithms

N-body simulations model the gravitational dynamics of massive particles. The algorithm solves for Newtonian gravity acting on N particles of fixed mass with known position and velocity vectors. N-body simulations are used to model dark matter particles which are collisionless and solely require gravitational processes. However, these codes are computationally expensive since they solve for the force on a particle exerted by each of its neighbours for every time step, and particle numbers can range in the trillions (e.g. Teyssier et al., 2009; Kim et al., 2009).

Hydrodynamic Algorithms

Hydrodynamic codes factor in fluid dynamics, thus are used to investigate baryonic matter and radiation, the latter of which can be modelled as a fluid. The fluid equations can be solved in one of two ways: Eulerian or Lagrangian. In the Eulerian scheme, the equations of conservation of mass, momentum and energy are solved on a grid of cells. The grid can be either structured or unstructured. Cells have a dynamic mass, which makes this technique suitable for large-scale simulations which contain regions of both over- and under-dense gas. However, although they can have a wide range of masses, uniform grids are limited in their spatial scales, making probing small scale physics problematic. Adaptive mesh refinement (AMR) solves this problem. AMR allows us to zoom in on regions of interest (e.g. galaxies) with higher resolution. This said, it is not practical to perform zoom-ins on every galaxy in a simulated cosmic box. A compromise must be made, choosing a limited number of special interest regions. In the Lagrangian method, instead of a grid, fixed-mass particles are used. Smooth particle hydrodynamics (SPH) are used to trace their paths (Gingold and Monaghan, 1977; Lucy, 1977). Neighbouring particles are smoothed over and the fluid equations are solved for them. SPH algorithms are suitable for simulating small scale regions.

Hybrid N-body and Hydrodynamic Algorithms

Hybrid codes incorporating both N-body and hydrodynamics have also been developed. The N-body aspect traces the dark matter particles which collapse to form dark matter haloes. The hydrodynamical side then solves for the gas particles, which follow the gravitational potential of the dark matter haloes, and collapse to form dense clouds of gas which birth stars and galaxies. These two computations are run simultaneously and couple the dark matter and gas via their mutual gravitational dependence. Cosmological simula-

tions of reionisation also incorporate atomic processes, such as ionisation, recombination, cooling and heating.

Radiative Transfer Algorithms

Radiative transfer codes solve for the propagation of the radiation field. They involve processes such as emission, absorption and scattering. They solve a seven-dimensional differential equation for the specific intensity to compute the evolution of the radiative field. The equation is a function of 3D position, 2D angular coordinates, time and frequency. This complexity makes calculating the direct solutions computationally expensive. Additionally, for cosmological simulations, the number of sources increases exponentially with volume, increasing the complexity of the problem. In order to deal with this, radiative transfer codes need to apply some physical approximations. There are three general methods for treating this problem: Monte Carlo, which employs a probabilistic technique to trace the discretised radiation field using photon packets emitted by each source; ray tracing, where rays are generated from each source and cast into segments as they propagate to each cell; and a moments-based approach, where the radiation is treated as a field using a system of conservative equations for the photon energy density and flux to describe the field as a fluid. Iliev et al. (2006a, 2009) performed a series of simple tests on several radiative transfer codes, showing that these different methods broadly agree.

2.1 RAMSES

RAMSES[1] is a fully coupled N-body and hydrodynamics code which utilises tree-based AMR and moments-based radiative transfer (Teyssier, 2002).

2.1.1 N-body Solver

Collisionless dark matter particles make up the N-body system which is treated using the Vlasov-Poisson equations

$$\frac{\mathrm{d}x_p}{\mathrm{d}t} = v_p, \quad \frac{\mathrm{d}v_p}{\mathrm{d}t} = -\nabla_x \phi, \text{ where } \nabla^2 \phi = 4\pi G \rho. \tag{2.1}$$

Here, the subscript p denotes the given particle, and ϕ represents the gravitational potential. For a grid-based N-body setup, the mass density on the particle mesh is first calculated using a cloud in cell (CIC) interpolation scheme. The gravitational potential and acceleration on the mesh are then computed using the Poisson equation. An inverse

[1] https://bitbucket.org/rteyssie/ramses/

CIC interpolation scheme is then used to calculate the acceleration of each particle in the mesh. The velocity and position of each particle can thus be updated.

2.1.2 Hydrodynamics Solver

For the gas dynamics, the Euler equations are solved in their conservative form using a second-order un-split Godunov solver:

$$\frac{\partial \rho}{\partial t} + \nabla \cdot (\rho u) = 0 \tag{2.2}$$

$$\frac{\partial}{\partial t}(\rho u) + \nabla \cdot (\rho u \otimes u) + \nabla p = -\rho \nabla \phi \tag{2.3}$$

$$\frac{\partial E}{\partial t} + \nabla \cdot [(E + p)u] = -\rho u \cdot \nabla \phi + \Lambda(\rho, \epsilon), \tag{2.4}$$

where ρ is the gas density, u is the bulk velocity of the fluid, p is the pressure, E is the gas total energy density, and Λ represents the radiative heating (positive) and cooling (negative) terms. These thermochemistry terms are functions of the gas density, temperature and ionisation state. For optically thin plasma, collisional ionisation equilibrium (CIE) is assumed. This allows for the ionisation states to be calculated as functions of the gas density and temperature, and are therefore not required to be tracked quantities. E is comprised of thermal and kinetic energy density (ϵ) components:

$$E = \frac{1}{2}\rho u^2 + \epsilon. \tag{2.5}$$

The set of Euler equations is closed with an equation of state relating the pressure and thermal energy,

$$p = (\gamma - 1)\epsilon, \tag{2.6}$$

where γ is the ratio of specific heats and is set to $\frac{5}{3}$ (for an ideal monatomic gas) by default. The ideal gas law relates the temperature to the internal energy by

$$\epsilon = \frac{3}{2} n k_{\mathrm{B}} T, \tag{2.7}$$

where n is the number density of gas particles and k_{B} is the Boltzmann constant. Assuming the gas is hydrogen only (H, H^+, e^-), the ideal gas law can be rewritten as:

$$\epsilon = \frac{3}{2} \frac{\rho}{\mu m_{\mathrm{H}}} k_{\mathrm{B}} T, \tag{2.8}$$

where μ is the mean molecular weight.

The Euler equations with gravitational source terms can be numerically discretised by the expression

$$\frac{\partial \mathcal{U}}{\partial t} + \nabla \mathcal{F}(\mathcal{U}) = \mathcal{S}, \tag{2.9}$$

where $\mathcal{U}$ is the conservative state vector and is the numerical approximation of the cell-averaged value of $(\rho, \rho u, E)$, $\mathcal{F}(\mathcal{U})$ is the time-centred flux vector across cell interfaces $(\rho u, \rho u \otimes u + p, (E+P)u)$, and $\mathcal{S}$ is the non-stiff gravitational source vector $(0, -\rho\nabla\phi, -\rho u \cdot \nabla\phi)$. The thermochemistry source term, Λ, is neglected as it is separated from the rest of the Euler equations in the numerical implementation. This makes modifying the thermochemistry solver (setting it to equilibrium or non-equilibrium) trivial. When metallicity is included, the conservative state vector also tracks the cell metal mass density ρZ, i.e. $\mathcal{U} = (\rho, \rho u, E, \rho Z)$.

2.1.3 Radiative Transfer

RAMSES has the advantage of performing coupled radiative transfer and hydrodynamics. This can be done with the ATON (Aubert and Teyssier, 2008) and RAMSES-RT (Rosdahl et al., 2013) modules, which both use a moments-based radiative transfer process with the M1 closure relation. ATON uses graphical processing units (GPUs) to post-process the radiative transfer after each hydrodynamic time-step. Since GPUs are very fast, they allow for ATON to utilise the full speed of light. However, to achieve this, the data outputs must be optimally structured onto a Cartesian grid, so that cells are arranged close in space and memory. Because of this, ATON is not suitable for AMR, posing a restriction in resolution. Nevertheless, it is well-suited for cosmological volumes and large-scale problems, such as reionisation, as opposed to small-scale galaxy formation simulations.

Moments-based Radiative Transfer

The radiative transfer equation is expressed as:

$$\frac{1}{c}\frac{\partial I_\nu}{\partial t} + \boldsymbol{n} \cdot \nabla I_\nu = -\kappa_\nu I_\nu + \eta_\nu, \tag{2.10}$$

where c is the speed of light, $I_\nu(\boldsymbol{x}, \boldsymbol{n}, t)$ is the radiation specific intensity, $\boldsymbol{n}$ is the direction of propagation, $\kappa_\nu(\boldsymbol{x}, \boldsymbol{n}, t)$ is the absorption coefficient, and $\eta_\nu(\boldsymbol{x}, \boldsymbol{n}, t)$ is the source function (Mihalas and Mihalas, 1984). The quantities I_ν, κ_ν and η_ν all depend on position, angle, frequency and time. For ionising radiation, the absorption coefficient is given by

$$\kappa_\nu = n_{\mathrm{HI}}\sigma_\nu, \tag{2.11}$$

where n_{HI} is the number density of neutral hydrogen and σ_ν is the photoionisation cross-section. The first two momenta of Equation 2.10 yields the two coupled equations,

$$\frac{\partial E_\nu}{\partial t} + \nabla \mathbf{F}_\nu = -\kappa_\nu c E_\nu + S_\nu, \tag{2.12}$$

and

$$\frac{\partial \mathbf{F}_\nu}{\partial t} + c^2 \nabla \mathbb{P}_\nu = -\kappa_\nu c \mathbf{F}_\nu, \tag{2.13}$$

where S_ν is the source term, E_ν is the radiation energy (the zeroth-order momentum of the intensity) given by

$$E_\nu(\boldsymbol{x}, t) = \frac{4\pi}{c} J_\nu = \frac{1}{c} \oint I_\nu \, \mathrm{d}\boldsymbol{\Omega}, \tag{2.14}$$

$\mathbf{F}_\nu$ is the radiation flux (the first-order momentum of the intensity) given by

$$\mathbf{F}_\nu(\boldsymbol{x}, t) = \oint I_\nu(\boldsymbol{x}, \boldsymbol{n}, t) \boldsymbol{n} \, \mathrm{d}\boldsymbol{\Omega}, \tag{2.15}$$

and $\mathbb{P}_\nu$ is the momentum pressure tensor (the second-order momentum of the intensity) given by

$$\mathbb{P}_\nu(\boldsymbol{x}, t) = \frac{1}{c} \oint I_\nu(\boldsymbol{x}, \boldsymbol{n}, t) \boldsymbol{n} \cdot \boldsymbol{n} \, \mathrm{d}\boldsymbol{\Omega}, \tag{2.16}$$

where $\mathrm{d}\boldsymbol{\Omega}$ is the solid angle. The four equations 2.10 - 2.13 define the set of conservation laws for the radiation fluid. The lower dimensionality of the equations and their conservative form make a numerical treatment appropriate.

Equations 2.12 and 2.13 can be rewritten in more suitable forms, in terms of number densities, by dividing them by a single photon energy, $h\nu$. They then become

$$\frac{\partial N_\nu}{\partial t} + \nabla \mathbf{F}_\nu = -\kappa_\nu c N_\nu + S_\nu, \tag{2.17}$$

and

$$\frac{\partial \mathbf{F}_\nu}{\partial t} + c^2 \nabla \mathbb{P}_\nu = -\kappa_\nu c \mathbf{F}_\nu, \tag{2.18}$$

where N_ν is the photon number density. For the sake of simplicity, we have kept the same notation for the photon flux and photon pressure tensor as for the energy flux and energy pressure tensor, respectively, although the latter have been divided by $h\nu$. The source term contains two contributions: stellar and quasar radiation, and diffuse radiation from recombination from HII,

$$S_\nu = \dot{N}_\nu^\star + \dot{N}_\nu^{\mathrm{rec}}, \tag{2.19}$$

where $\dot{N}_\nu^{\mathrm{rec}} = n_{\mathrm{e}} n_{\mathrm{HII}} \dot{\epsilon}_\nu(T)$. Both sources are assumed to be isotropic and, thus, there is no source term in the flux equation.

A single species, hydrogen, and single photon group, i.e. all photons whose energies are greater than the threshold energy for hydrogen, are considered for the sake of simplicity. This scheme can be extended to incorporate a more realistic assortment of species and multi-frequency photons by using the approach described in Rosdahl et al. (2013).

In order to close the system of equations, an expression for the pressure tensor must be provided. To do this, the time evolution of the hydrogen ionisation fraction and the gas

temperature must be solved. We need to consider the physical processes that influence the chemical evolution of neutral hydrogen: collisional ionisation, photoionisation and collisional recombination,

$$\frac{\mathrm{D}}{\mathrm{D}t}\left(n_{\mathrm{HI}}\right) = \alpha_{\mathrm{A}} n_{\mathrm{e}} n_{\mathrm{HII}} - \beta n_{\mathrm{e}} n_{\mathrm{HI}} - \Gamma_{\gamma\mathrm{HI}} n_{\mathrm{HI}}, \tag{2.20}$$

where $\alpha_{\mathrm{A}}(T)$ is the recombination coefficient of ionised hydrogen for case A taken from the fits in Hui and Gnedin (1997), $\Gamma_{\gamma\mathrm{HI}}$ is the hydrogen atom photoionisation rate (defined as $\Gamma_{\gamma\mathrm{HI}} = c\sigma_{\gamma}N_{\gamma}$, where $\sigma_{\gamma} = 1.63 \times 10^{-18}$ cm^2 and N_{γ} is the ionising photon number density); as well as charge conservation (i.e. $n_{\mathrm{e}} = n_{\mathrm{HII}}$) and hydrogen nuclei conservation (i.e. $n_{\mathrm{HII}} + n_{\mathrm{HI}} = n_{\mathrm{H}}$).

Solving the gas-thermal energy equation takes into account the radiative cooling and photoionisation heating:

$$\rho\frac{\mathrm{D}}{\mathrm{D}t}\left(\frac{e}{\rho}\right) = \mathcal{H} - \mathcal{L}, \tag{2.21}$$

where $e = \frac{3}{2}n_{\mathrm{tot}}k_{\mathrm{B}}T$. The cooling rate, $\mathcal{L}$, is calculated using standard collisional cooling processes from hydrogen recombination, collisional ionisation and excitation of hydrogen and Bremsstrahlung. The fits used for the cooling rates are taken from Hui and Gnedin (1997); Maselli et al. (2003) and references therein. The photoionisation heating rate is given by $\mathcal{H} = n_{\mathrm{HI}}\dot{\epsilon}_{\mathrm{HI}}$, where $\dot{\epsilon}_{\mathrm{HI}} = c\int_{\nu_{\mathrm{HI}}}^{\infty}\left(h\nu - h\nu_{\mathrm{HI}}\right)\sigma_{\nu}N_{\nu}\mathrm{d}\nu = c\epsilon_{\gamma}\sigma_{\gamma}N_{\gamma}$.

Aubert and Teyssier (2008) implement the simple closure relation to cosmological reionisation, the M1 approximation (Levermore, 1984). It solves the radiative transfer equations in the optically thick limit, while retaining some accuracy in the optically thin regime. The assumption is made that the angular distribution of the radiation is axisymmetric around $\mathbf{F}$. Thus, the Eddington tensor, $\mathbb{P} = \mathbb{D}N$, can be written in the general form

$$\mathbb{D} = \frac{1-\chi}{2}\mathbf{I} + \frac{3\chi - 1}{2}\boldsymbol{u}\otimes\boldsymbol{u}, \tag{2.22}$$

where $\boldsymbol{u}$ is a unit vector in the direction of the flux, and χ is the Eddington factor,

$$\chi = \frac{3 + 4|\boldsymbol{f}|^2}{5 + 2\sqrt{4 - 3|f|^2}}, \tag{2.23}$$

where $\boldsymbol{f}$ is the reduced flux, $\boldsymbol{f} = \frac{\mathbf{F}}{cN} = f\boldsymbol{u}$.

Numerical Implementation

The set of equations previously described can now be solved numerically. This is done in three steps which are performed in order for the the same time step, Δt:

1. the *photon injection step*, where ionising radiation from stellar and radiative sources are injected into the grid;

2. the *transport step*, where photons are propagated into space, and the hyperbolic system of equations are solved;

3. the *thermochemistry step*, where the photons and gas couple, thus the photon densities and fluxes, and ionisation state and gas temperature are evolved, and the right-hand side of the radiation transport model is solved.

For the injection step, photons can originate from stellar sources as well as other point sources (e.g. AGNs) and continuous volume sources (see e.g. Rosdahl and Blaizot, 2012). For the transport step, the right-hand sides of the hyperbolic system are set to 0:

$$\frac{\partial N_\nu}{\partial t} + \nabla \mathbf{F}_\nu = 0, \tag{2.24}$$

$$\frac{\partial \mathbf{F}_\nu}{\partial t} + c^2 \nabla \mathbb{P}_\nu = 0. \tag{2.25}$$

These can be expressed in vector form,

$$\frac{\partial \mathcal{U}}{\partial t} + \nabla \mathcal{F}(\mathcal{U}) = 0, \tag{2.26}$$

with $\mathcal{U} = [N_\nu, \mathbf{F}_\nu]$ and $\mathcal{F}(\mathcal{U}) = \left[\mathbf{F}_\nu, c^2 \mathbb{P}_\nu\right]$. This equation can be solved using various intercell flux functions. We direct the reader to Aubert and Teyssier (2008) and Rosdahl et al. (2013) for more detailed descriptions of the functions used and of the thermochemical step in ATON (Aubert and Teyssier, 2008) and RAMSES-RT (Rosdahl et al., 2013).

2.1.4 Time Step Control

The time steps have to abide by the constraint imposed by the Courant-Friedrichs-Lewy (CFL) condition. The CFL condition states that the time step must be less than a given time during which a wave can propagate through the fluid element. In other words, the numerical domain of dependence must include the physical (or analytical) domain of dependence. It ensures that the information has enough time to propagate across a spatial interval, in order to prevent the simulation from producing incorrect results. This time step is given by

$$\Delta t = C \frac{\Delta x}{\max\left(|u_x| + c, |u_y| + c, |u_z| + c\right)}, \tag{2.27}$$

where $C < 1$ is the Courant factor, and $|u_x|$, $|u_y|$ and $|u_y|$ are the magnitudes of the x-, y- and z-components of the velocity.

2.1.5 Cosmological Settings

For cosmological simulations, such as the ones in our study, both N-body and hydrodynamics solvers use conformal time as the time variable. This way, comoving coordinates can be easily implemented. The original equations need to be adjusted for the comoving coordinate system. Essentially, these super-comoving variables (Martel and Shapiro, 1998) are:

$$\mathrm{d}\tilde{t} = \frac{H_0}{a^2}\mathrm{d}t, \tag{2.28}$$

$$\tilde{x} = \frac{1}{aL}x, \tag{2.29}$$

$$\tilde{\rho} = \frac{a^3}{\Omega_\mathrm{m}\rho_\mathrm{c}}\rho, \tag{2.30}$$

$$\tilde{p} = \frac{a^5}{\Omega_\mathrm{m}\rho_\mathrm{c}H_0^2L^2}p, \tag{2.31}$$

and

$$\tilde{u} = \frac{a}{H_0L}u, \tag{2.32}$$

where H_0 is the Hubble constant, L is the box size, Ω_m is the matter density parameter, and ρ_c is the critical density. Using these variables in lieu of the physical ones accounts for cosmological expansion, while the relevant equations remain unchanged.

2.1.6 Star Formation

Cosmological simulations are still very limited in the resolution down to which they can go. As a result, star formation has to be treated using a sub-grid approach. In RAMSES, gas is converted into stellar particles in each cell following a standard Schmidt law. When the gas density in a cell is larger than a specified gas over-density, $\delta_\star$ (or hydrogen number density, $n_\star$), and the temperature is lower than a set temperature threshold, $T_\star = 2 \times 10^4$ K, a new star particle is formed at a rate of

$$\dot{\rho}_\star = \epsilon_\star \frac{\rho_\mathrm{gas}}{t_\mathrm{ff}}, \tag{2.33}$$

where $\epsilon_\star$ is the star formation efficiency per free fall time, $t_\mathrm{ff} = \sqrt{\frac{3\pi}{32G_\rho}}$. When these criteria are met, $N_\star$ equal-mass, collisionless stellar particles are spawned stochastically via a Poisson distribution with probability,

$$P(N_\star) = \frac{\lambda_\mathrm{P}}{N_\star!}\mathrm{e}^{-\lambda_\mathrm{P}}, \tag{2.34}$$

with a mean value

$$\lambda_\mathrm{P} = \left(\frac{\rho\Delta x^3}{m_\star}\right)\frac{\Delta t}{t_\star}, \tag{2.35}$$

where Δx^3 is the volume of the cell, and Δt is the simulation time step. The star particle mass is taken to be an integer multiple of $m_\star = \frac{\rho_0 \Delta x^3_{\rm min}}{1+\eta_{\rm SN}+\eta_{\rm W}}$ (see Section 2.1.7 for more on the parameters $\eta_{\rm SN}$ and $\eta_{\rm W}$). For more details on the star formation algorithm adopted in RAMSES, see Rasera and Teyssier (2006).

2.1.7 Supernova Feedback

During star formation, some gas mass is depleted and converted into stellar particles:

$$\Delta m_{\rm gas} = m_\star \left(1 + \eta_{\rm SN} + \eta_{\rm W}\right), \tag{2.36}$$

where $\eta_{\rm SN}$ is the supernova mass fraction, and $\eta_{\rm W}$ is the mass loading factor which determines the mass of gas carried in the supernova ejecta. A supernova explosion is triggered 10 Myr after the birth of a star particle. When this occurs, $\eta_{\rm SN} = 10\%$ of the star particle's mass goes to the supernova, and kinetic energy,

$$E_{\rm debris} = \eta_{\rm SN} \frac{m_\star}{M_{\rm SN}} E_{\rm SN}, \tag{2.37}$$

where $M_{\rm SN} = 10\ {\rm M}_\odot$ is the progenitor mass and $E_{\rm SN} = 10^{51}$ erg is the energy of the supernova, is released into the gas by the debris. $\eta_{\rm W}$ is a free parameter and can be as low as 0, depending on the gas density of adjacent cells. After the explosion, the remaining stellar population is represented by a low mass, long-lived star particle with mass

$$M_\star = \left(1 - \eta_{\rm SN}\right) m_\star. \tag{2.38}$$

See Dubois and Teyssier (2008) for more details of the supernova feedback employed in RAMSES.

2.2 Initial Conditions

Initial conditions are used to specify the starting values of the variables in the simulation such that the code produces a desired output. For structure formation, the cosmological model must be specified, e.g. H_0, density parameters and the nature of dark matter (e.g. CDM). Cosmological simulations of reionisation assume a spatially flat universe ($\Omega_{\rm k} = 0$). Fluctuations in the density fields of baryons and dark matter are mapped onto Gaussian random fields using their power spectra, $P(k)$. For an initial 3D Gaussian random field, $\delta(\boldsymbol{x})$, with Fourier transform, $\delta(\boldsymbol{k})$, the power spectrum is given by

$$P(k)\delta_D(\boldsymbol{k} - \boldsymbol{k}') = \left\langle \delta(\boldsymbol{k})\delta^*(\boldsymbol{k})' \right\rangle, \tag{2.39}$$

for fields with zero mean-squared amplitude. Uncorrelated, random Gaussian noise is generated in Fourier space, and then the amplitudes are scaled to match the input power spectrum (Pen, 1997; Bertschinger, 2001; Prunet et al., 2008).

2.3 Running RAMSES

In order to perform a simulation using RAMSES, initial conditions must first be generated. This can be done using codes specifically made for this, e.g. the MUlti-Scale cosmological Initial Conditions (MUSIC)[2] code (Hahn and Abel, 2013). A configuration file is made, which specifies the input parameters: box length, starting redshift, minimum and maximum resolution levels, cosmological parameters, etc. While MUSIC can be used for multiple levels of resolution (AMR), it can also be utilised for uniform grids by setting the same value for the minimum and maximum resolution levels.

Next, a namelist file (`.nml`) containing the run time parameters for RAMSES needs to be created. Within this input file the location of the initial conditions file needs to be specified. Additionally, the RAMSES module to be used and the types of solvers are specified here. The number or frequency of outputs and end time are set in the output parameters. Under the physics parameters, cooling (e.g. by metals), star formation (e.g. stellar particle mass, star formation timescale, star formation efficiency, etc.), and feedback (e.g. by supernovae) parameters are specified.

For cosmological simulations of the EoR, the basic parameters which control reionisation are: the physics parameters `eps_star` ($\epsilon_\star$), which is the efficiency of mass collapse for star formation, `del_star` ($\delta_\star$), which is the star formation density threshold in critical density, and `n_star` ($n_\star$), which is the star formation density threshold in hydrogen number density; and radiation parameter `rad_escape_fraction` ($f_{\mathrm{esc},\star}$), which is the stellar particle escape fraction.

For a more detailed description for compiling and running RAMSES, we direct the reader to its online documentation at `https://bitbucket.org/rteyssie/ramses/wiki/`.

There are a few tools available to read and analyse the data produced by RAMSES. These are also listed in the RAMSES Wiki page. For this study, we use a package developed by David Sullivan, `seren3`[3], which is a Python module that utilises a modified version of PyMSES[4].

[2] `https://bitbucket.org/ohahn/music/`
[3] `https://github.com/sully90/seren3/`
[4] `http://irfu.cea.fr/Projets/PYMSES/`

Chapter 3

Finding the tSZ Effect from the EoR

3.1 Introduction

The EoR marks the most recent global phase transition of the universe. It is the period in cosmic history during which the first luminous objects (stars, galaxies, and quasars, etc.) formed. The UV radiation emitted by these objects ionised the neutral gas in the IGM.

Although current and upcoming surveys (e.g. LOFAR, SKA, JWST[1]) will give us more insight into this epoch, much remains unknown. For instance, it is still unclear what the main drivers of reionisation are, we are yet to obtain observational evidence to support that it was an inside-out process, and we lack tight constraints on the timing of its start and duration. Low-frequency radio surveys will allow us to obtain the 21 cm tomographical signal from the neutral hydrogen gas during the dark ages and cosmic dawn, while infrared imaging will shed more light on bright luminous sources at higher redshifts than previously done. Additionally, the EoR imprints information in the CMB. While the primary anisotropies of the CMB store information about the primordial density fluctuations at last scattering, the secondary anisotropies are due to interactions between the CMB photons and matter along their paths to us. The secondary anisotropies in the CMB can thus shed light on the structures and physics in the universe. One of the contributors of these fluctuations is the SZ effect.

The SZ effect (Sunyaev and Zeldovich, 1972, 1980a,b) arises from the inverse Compton scattering of photons by energetic electrons. This effect distorts the CMB spectrum from that of a pure black-body. There are two types of SZ effect: the tSZ effect is caused by

[1] https://www.jwst.nasa.gov/

electrons which are thermally energised, while the kSZ effect arises from electrons whose energies are due to their velocities from large-scale structure bulk motions. An example of these effects can be seen with galactic clusters. When low frequency photons travel through a cluster, they can be scattered by the hot (10^7 - 10^8 K) intra-cluster gas (tSZ effect) and by the bulk velocity of the cluster as a whole (kSZ effect).

The kSZ effect has been used as a probe of the EoR (see e.g. Iliev et al., 2007, 2008; Mesinger et al., 2012; Park et al., 2013), whereby during reionisation inhomogeneities in the electron density and velocity fields produce temperature fluctuations in the CMB. These works have shown that EoR has appreciable contribution to the small-scale ($\ell > 3000$) CMB anisotropies.

In contrast, to our knowledge, no previous work has been done to calculate the tSZ signal from the EoR using numerical simulations. The tSZ effect is most commonly used in studies of clusters. Due to its characteristic spectral signature (the tSZ effect lowers the intensity of the photons at frequencies < 218 GHz, and raises it at frequencies > 218 GHz), the tSZ effect is used as redshift-independent approach to detect clusters. It is also useful for measuring the thermal energy of clusters since the integral of the tSZ flux over the solid angle of the cluster is proportional to the cluster mass.

The tSZ effect is a measure of the integrated electron pressure along the line of sight. During the EoR the galaxy clusters would not have yet formed, and the typical electron gas temperatures caused by photoionisation are of order tens of thousands of K, rather than millions of K found in clusters. However, the matter density of both halos and IGM are much higher than at later times ($\propto (1+z)^3$), due to the effects of Hubble expansion. We can therefore reasonably expect that the EoR-produced electron pressure can provide a non-trivial contribution to the total observed effect. Furthermore, since the tSZ effect from the EoR has some contribution from the diffuse IGM in the ionised patches, the spatial structure of the temperature fluctuations should be different from the one produced by clusters, potentially providing a new interesting probe of cosmic reionisation. The aim of this study is to investigate the strength of this effect and its detectability.

3.2 Simulations

We investigate the tSZ signal arising from the EoR by analysing the data produced by a series of radiation-hydrodymanics simulations run using the RAMSES-CUDATON code (Teyssier, 2002; Aubert and Teyssier, 2008). This version of RAMSES does not utilise AMR; instead, it uses a fixed grid. The largest of these is Cosmic Dawn II (CoDa II; Ocvirk

et al., 2018). The results of fifteen smaller auxiliary simulations are used to investigate the effects of volume, spatial resolution and star formation parameters on the tSZ signal. The parameters and setup of the simulations are summarised in Tables 3.1 and 3.2.

3.2.1 Cosmic Dawn II

CoDa II (Ocvirk et al., 2018) is a large fully-coupled radiation and hydrodynamics simulation of the EoR and galaxy formation. Its large volume and high resolution make it particularly important in the field of large-scale simulations. A Planck 2014 cosmology (Planck Collaboration et al., 2014) was used for CoDa II: $\Omega_\Lambda = 0.693$, $\Omega_m = 0.307$, $\Omega_b = 0.045$, $H_0 = 67.77$, and power spectrum normalisation $\sigma_8 = 0.8288$ and slope $n = 0.963$. CoDa II was run on the Titan supercomputer at the Oak Ridge Leadership Computational Facility (OLCF)[2] in Tennessee, USA. The comoving box is 64 h^{-1} Mpc (94.4 Mpc) on a side with a fixed grid of 4096^3 cells for gas and radiation fields, and 4096^3 dark matter particles. CoDa II starts at redshift $z = 150$ and ends at $z = 5.80$.

For storage purposes, data for the full-resolution grid was reduced to a coarser grid of 2048^3 cells. Full-box low-resolution data for the gas properties, ionising flux density, and dark matter density field were kept for all snapshots, as well as a catalogue of the stellar particles. It is the full-box, low-resolution data that we use for this project. For a more detailed description of CoDa II, we direct the reader to Ocvirk et al. (2018).

3.2.2 10, 50, 100 h^{-1} Mpc Simulations

Seven smaller auxiliary simulations were run as part of a Partnership for Advanced Computing in Europe (PRACE)[3] Tier-0 project. The initial conditions were produced by the Constrained Local UniversE Simulations (CLUES) project[4] (Gottloeber et al., 2010). We used a cosmology consistent with the latest constraints from the Planck survey (Planck Collaboration et al., 2018a): $\Omega_\Lambda = 0.682$, $\Omega_m = 0.318$, $\Omega_b = 0.045$, $H_0 = 67.1$, and power spectrum normalisation $\sigma_8 = 0.833$ and slope $n = 0.9611$. These simulations vary in volume, spatial resolution and star formation parameters, but all have a fixed grid of 1024^3 cells with 1024^3 dark matter particles.

There are four boxes with sides 100 h^{-1} Mpc (149.0 Mpc), one box with side 50 h^{-1} Mpc (74.5 Mpc), and two boxes with sides 10 h^{-1} Mpc (14.9 Mpc). We use the abbreviations 100-δ20-f0.25-ϵ3.5, 100-δ20-f0.3-ϵ5, 100-δ20-f0.25-ϵ6 and 100-δ20-f0.3-ϵ8

[2] https://www.olcf.ornl.gov/

[3] http://www.prace-ri.eu/

[4] https://www.clues-project.org/

Table 3.1: Summary of the simulation setup for CoDa II and the auxiliary simulations.

	CoDa II	100-δ20-f0.25-$e^{3.5}$	100-δ20-f0.3-e^{5}	100-δ20-f0.25-e^{6}	100-δ20-f0.3-e^{8}	50-δ30-f0.25-$e^{2.5}$	10-δ200-f0.2-$e^{3.5}$	10-δ200-f0.25-$e^{3.5}$-η^{15}	25-δ30-f0.1-e^{4}	25-δ30-f0.14-e^{4}	25-δ30-f0.2-e^{4}	25-δ30-f0.2-e^{2}	25-δ30-f0.2-e^{2}-η^{15}	25-δ30-f0.25-$e^{2.5}$	25-δ50-f0.3-e^{3}	25-δ50-f0.5-e^{1}
Number of nodes (GPUs)	16384	128				128	128		8							
Grid size	4096^3	1024^3				1024^3	1024^3		512^3							
Box size, $L_{\rm box}/h^{-1}$ Mpc	64	100				50	10		25							
Grid cells per node	$128 \times 128 \times 64$	$256 \times 256 \times 128$				$256 \times 256 \times 128$	$256 \times 256 \times 128$		$256 \times 256 \times 256$							
Spatial resolution, $\mathrm{d}x/h^{-1}$ kpc	15.6	97.7				48.8	9.8		24.4							
DM particle number, $N_{\rm DM}$	4096^3	1024^3				1024^3	1024^3		512^3							
DM particle mass, $M_{\rm DM}/\mathrm{M}_\odot$	4.07×10^5	1.05×10^8				1.31×10^7	1.05×10^5		1.32×10^7							
Initial redshift, $z_{\rm start}$	150	80				80	80		80							
End redshift, $z_{\rm end}$	5.8	4.0	0.0	4.1	1.0	0.0	6.4	6.7	5.0							
Number of snapshots	92	135	260	134	207	260	81	75	138							

Table 3.2: Summary of the Physics parameters for CoDa II and the auxiliary simulations.

	Density threshold, $\delta_\star$	Efficiency, $\epsilon_\star$	Mass fraction, $\eta_{\rm SN}$	Stellar particle escape fraction, $f_{{\rm esc},\star}$
CoDa II	$50\,\langle\rho\rangle$	0.02	10%	0.42
100-δ20-f0.25-ϵ3.5	$20\,\langle\rho\rangle$	0.035	10%	0.25
100-δ20-f0.3-ϵ5	$20\,\langle\rho\rangle$	0.05	10%	0.3
100-δ20-f0.25-ϵ6	$20\,\langle\rho\rangle$	0.06	10%	0.25
100-δ20-f0.3-ϵ8	$20\,\langle\rho\rangle$	0.08	10%	0.3
50-δ30-f0.25-ϵ2.5	$30\,\langle\rho\rangle$	0.025	10%	0.25
10-δ200-f0.2-ϵ3.5	$200\,\langle\rho\rangle$	0.035	10%	0.2
10-δ200-f0.25-ϵ3.5-η15	$200\,\langle\rho\rangle$	0.035	15%	0.25
25-δ30-f0.1-ϵ4	$30\,\langle\rho\rangle$	0.04	10%	0.1
25-δ30-f0.14-ϵ4	$30\,\langle\rho\rangle$	0.04	10%	0.14
25-δ30-f0.2-ϵ4	$30\,\langle\rho\rangle$	0.04	10%	0.2
25-δ30-f0.2-ϵ2	$30\,\langle\rho\rangle$	0.02	10%	0.2
25-δ30-f0.2-ϵ2-η15	$30\,\langle\rho\rangle$	0.02	15%	0.2
25-δ30-f0.25-ϵ2.5	$30\,\langle\rho\rangle$	0.025	10%	0.25
25-δ50-f0.3-ϵ3	$50\,\langle\rho\rangle$	0.03	10%	0.3
25-δ50-f0.5-ϵ1	$50\,\langle\rho\rangle$	0.01	10%	0.5

for the 100 Mpc boxes with $\epsilon_\star = 0.035$, 0.05, 0.06 and 0.08, respectively. The 10 Mpc boxes also have different stellar escape fractions, but the same star formation efficiency. We use the abbreviations 10-δ200-f0.2-ϵ3.5 and 10-δ200-f0.25-ϵ3.5-η15 for the 10 Mpc boxes with escape fractions $f_{\mathrm{esc},\star} = 0.2$ and 0.25, respectively. Note that, although we use abbreviated annotations for the boxes, their parameters differ more than the annotations might imply. A notable feature of 10-δ200-f0.25-ϵ3.5-η15 is that it has a higher supernova mass fraction ($\eta_{\mathrm{SN}} = 15\%$) than the other boxes and CoDa II ($\eta_{\mathrm{SN}} = 10\%$), i.e. a larger fraction of the stellar particle mass will go supernova at the end of the massive stellar lifetime.

With the exception of 10-δ200-f0.25-ϵ3.5-η15, all simulations run from $z = 80$ to the end of the EoR or later. 10-δ200-f0.25-ϵ3.5-η15 was stopped early since its ionisation fraction was evolving much faster than expected and reionisation was due to be completed too early and sooner than observations suggest. 100-δ20-f0.3-ϵ5 and 50-δ30-f0.25-ϵ2.5 were run on the Piz Daint supercomputer at the CSCS Swiss National Supercomputing Centre[5] in Switzerland. 100-δ20-f0.25-ϵ3.5, 100-δ20-f0.25-ϵ6, 100-δ20-f0.3-ϵ8, 10-δ200-f0.2-ϵ3.5 and 10-δ200-f0.25-ϵ3.5-η15 were performed on the Jureca supercomputer at the Jülich Supercomputing Centre (JSC)[6] in Germany. The full-resolution data for these simulations were kept in addition to halo catalogues.

3.2.3 25 h^{-1} Mpc Simulations

A series of eight smaller simulations was also run, to investigate the effects of the Physics parameters responsible for the reionisation history on the tSZ effect. The initial conditions were generated with MUSIC, using the cosmological parameters of the simulations in Section 3.2.2. Each run was performed on 8 GPU nodes on the Apollo2 HPC at the University of Sussex, and took just over 2 days to complete. These boxes are 25 h^{-1} Mpc (37.3 Mpc) on a side, with a resolution of 512^3 cells and 512^3 dark matter particles. Each run starts at redshift $z = 80$ and ends after reionisation, at $z = 5$. The simulation parameters which were varied were the density threshold, $\delta_\star$, stellar particle escape fraction, f_{esc}, star formation efficiency, $\epsilon_\star$, and supernova mass fraction, η_{SN}. Each simulation is named in the same style as the previous auxiliary simulations, according to the parameters which were changed. Full-resolution data was used for these simulations.

[5] https://www.cscs.ch/

[6] https://www.fz-juelich.de/ias/jsc/

The main differences between these simulations and CoDa II are the feedback mechanisms and star formation parameters. For instance, the temperature threshold, $T_\star$, for the interstellar gas is switched off in CoDa II, i.e. there is no temperature limit below which the cells need to be for stars to be formed. However, it is turned on in our auxiliary simulations, and has the default value of $T_\star = 2 \times 10^4$ K. Above this temperature, the hydrogen gas is fully ionised and unable to efficiently cool, thus, suppressing star formation. The justification for doing this in CoDa II is that, at higher resolution, in ionised cells, there can still exist cold neutral regions which may still be capable of forming stars.

The advantage that the suite of 25 Mpc simulations has over the others is that we can directly compare the effects of the timing of reionisation and the Physics simulation parameters on the tSZ effect arising during the EoR. This is possible since we have eliminated the effects of resolution, box size and other differences that exist among the larger simulations.

3.2.4 Calibrations Using Global Quantities

In order to test that the simulations are realistic, we compare their reionisation histories with observational constraints. In Figures 3.1 - 3.5, we plot the evolution of the mean global neutral hydrogen fraction, ionised hydrogen fraction, ionisation rate, optical depth and average star formation rate density, respectively, along with their observational constraints. These are the basic quantities with which to gauge the success of an EoR simulation.

Global Reionisation History

Figures 3.1 and 3.2 show the evolution of the mean neutral and ionised hydrogen fractions, respectively, as well as their observational constraints. We have grouped the reionisation histories of the four 25 Mpc boxes that reionise earlier in the rose-brown band: 25-δ30-f0.14-ϵ4, 25-δ30-f0.2-ϵ4, 25-δ30-f0.25-ϵ2.5 and 25-δ50-f0.3-ϵ3. The blue band represents the four 25 Mpc simulations that are later to reionise: 25-δ30-f0.1-ϵ4, 25-δ30-f0.2-ϵ2, 25-δ30-f0.2-ϵ2-η15 and 25-δ50-f0.5-ϵ1. Below $z = 7$, the mean neutral fraction sharply decreases down to $\langle x_{\rm HI} \rangle \lesssim 10^{-4}$, and then becomes shallower in gradient. This transition marks the end of reionisaton. In the ionised fraction plots, this is roughly the points at which the slopes flatten. Hence, we see from the neutral fractions, that the simulations finish reionising between $z \sim 6.6$ and $z \sim 5.5$. As the two 10 Mpc simulations (dashed lines) were not run until reionisation was completed, their lines stop short, at $z \sim 6.3$ (10-δ200-f0.2-ϵ3.5) and $z \sim 6.7$ (10-δ200-f0.25-ϵ3.5-η15).

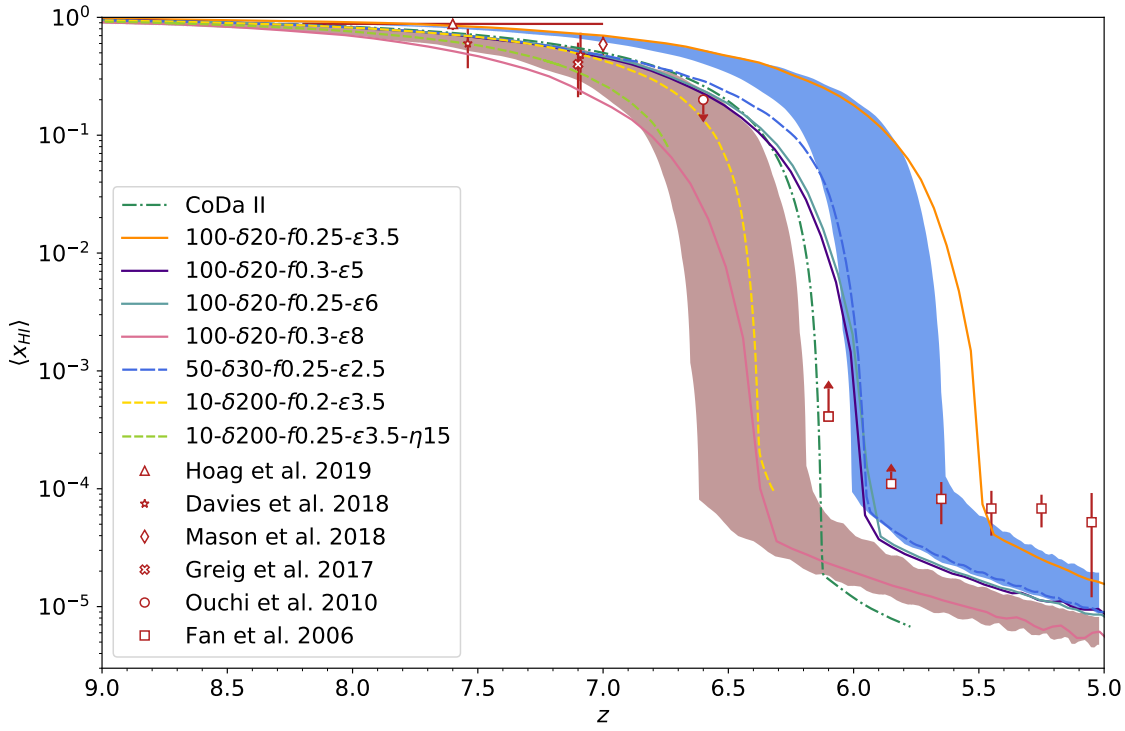

Figure 3.1: Evolution of the globally averaged neutral hydrogen fraction and its observational constraints (Hoag et al., 2019; Davies et al., 2018; Mason et al., 2018; Greig et al., 2017; Ouchi et al., 2010; Fan et al., 2006). The rose-brown band includes the reionisation histories for 25-δ30-f0.14-ϵ4, 25-δ30-f0.2-ϵ4, 25-δ30-f0.25-ϵ2.5 and 25-δ50-f0.3-ϵ3, and the blue band includes those for 25-δ30-f0.1-ϵ4, 25-δ30-f0.2-ϵ2, 25-δ30-f0.2-ϵ2-η15 and 25-δ50-f0.5-ϵ1.

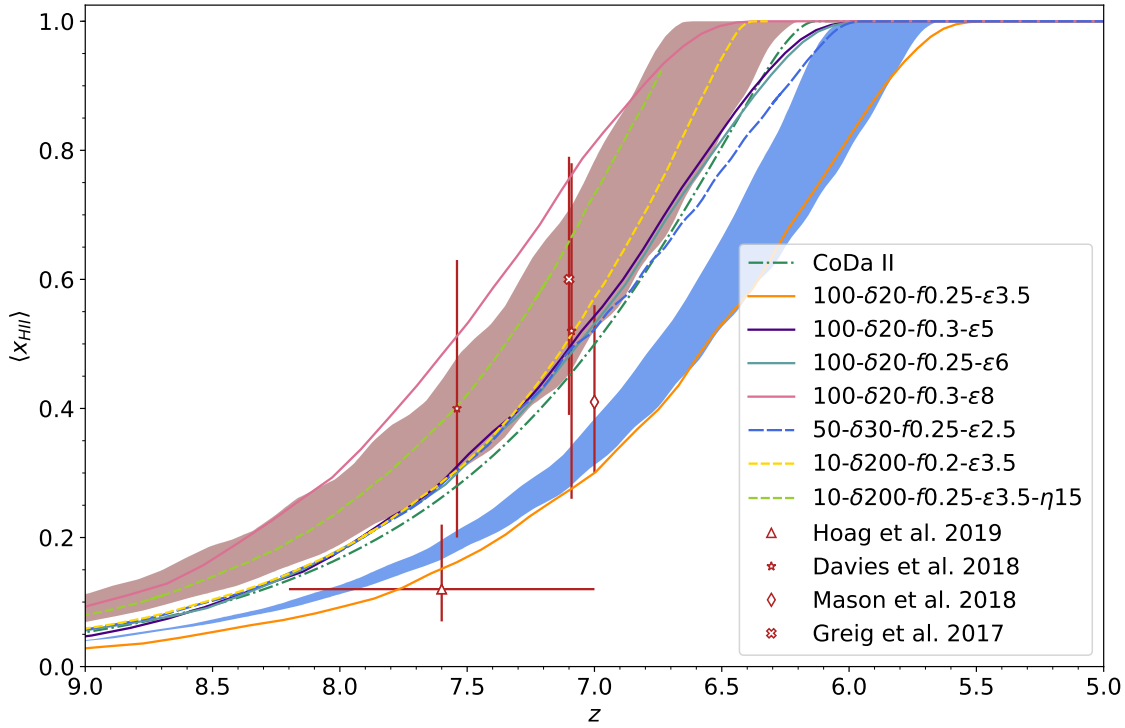

Figure 3.2: Evolution of the globally averaged ionised hydrogen fraction and its observational constraints (Hoag et al., 2019; Davies et al., 2018; Mason et al., 2018; Greig et al., 2017). The coloured bands represent the same simulations as in the previous figure.

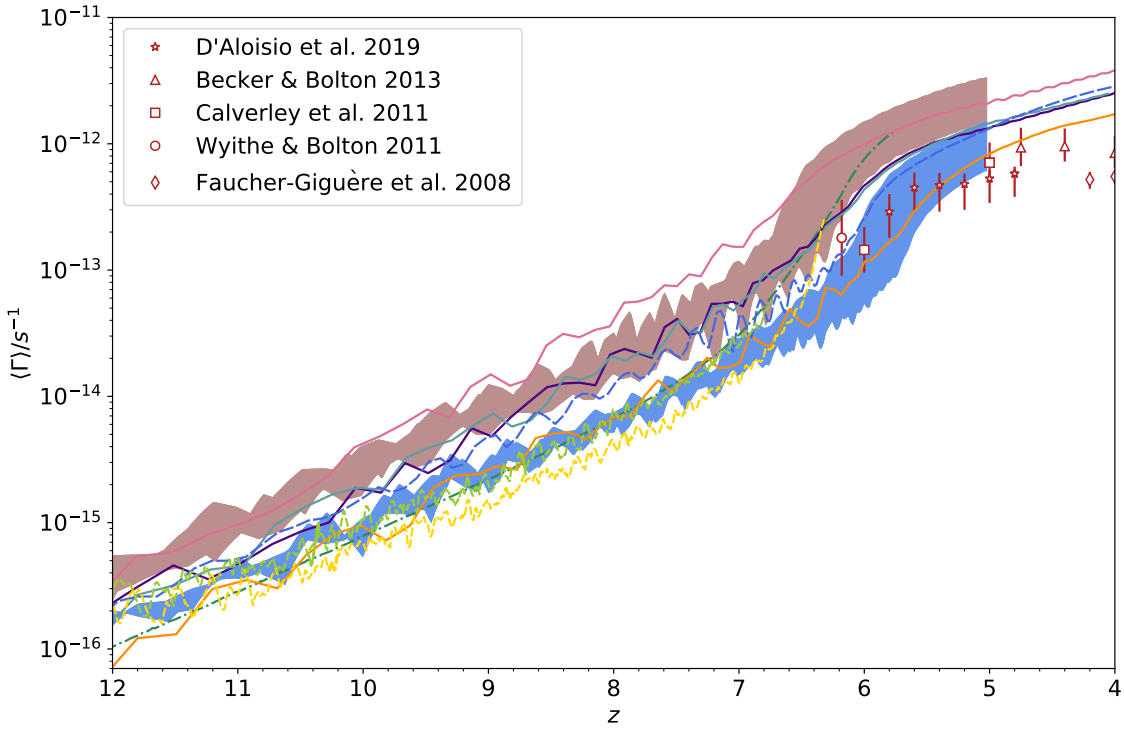

Figure 3.3: Evolution of the globally averaged photoionisation rate and its observational constraints (D'Aloisio et al., 2019; Becker and Bolton, 2013; Calverley et al., 2011; Wyithe and Bolton, 2011; FaucherGiguère et al., 2008). The lines and coloured bands represent the same simulations as in the previous figures.

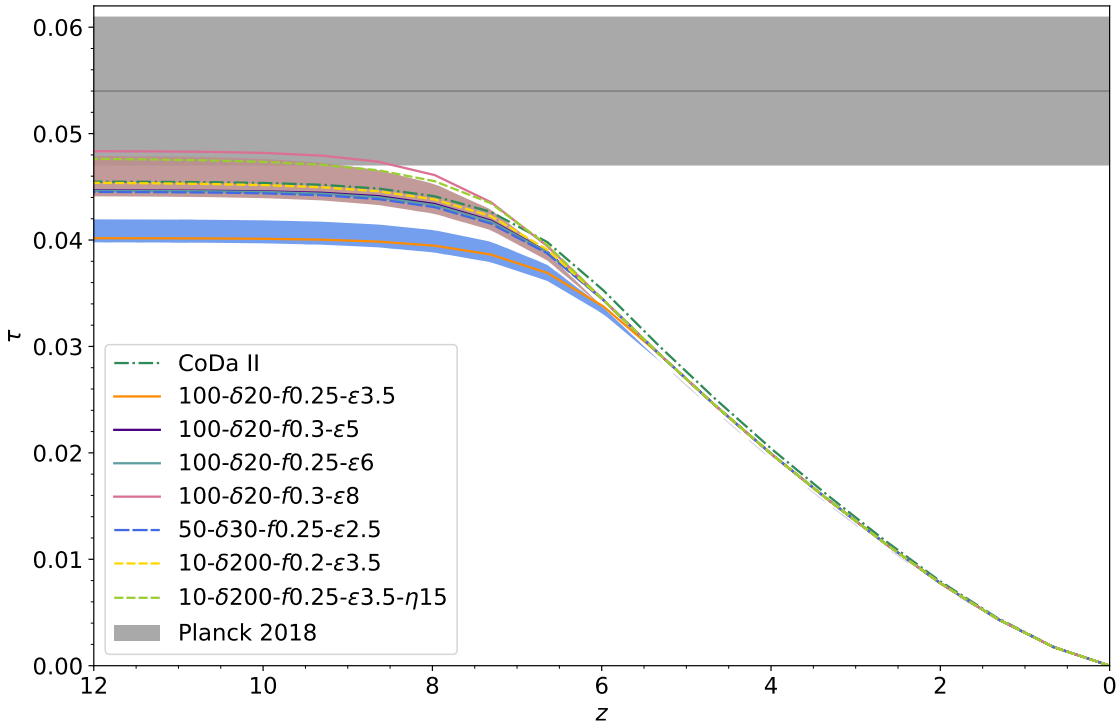

Figure 3.4: Evolution of the Thomson-scattering optical depth to reionisation. The latest measurement from the Planck Collaboration (Planck Collaboration et al., 2018a) including its 1σ error (grey shaded area) is plotted for comparison. The coloured bands represent the same simulations as in the previous figures.

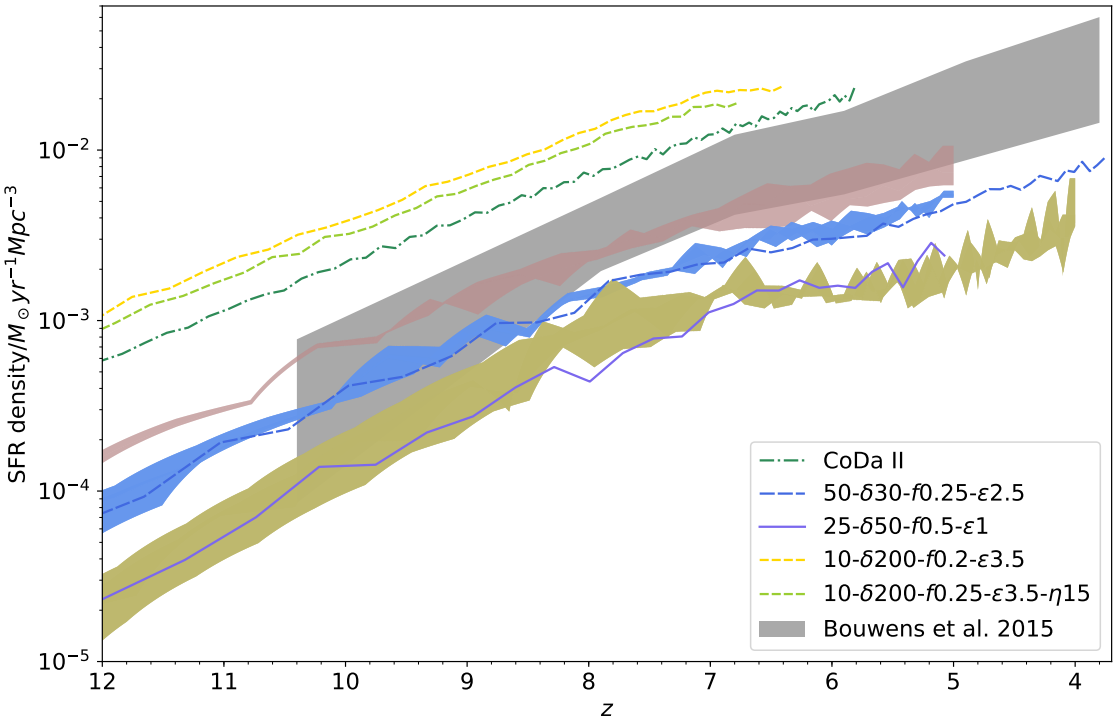

Figure 3.5: Evolution of the global star formation rate density. The dust-corrected and dust-uncorrected observations from Bouwens et al. (2015) are indicated by the grey shaded region. The rose-brown band includes the SFR densities of 25-δ30-f0.1-ϵ4, 25-δ30-f0.14-ϵ4 and 25-δ30-f0.2-ϵ4, the blue band includes those of 25-δ30-f0.2-ϵ2, 25-δ30-f0.2-ϵ2-η15, 25-δ30-f0.25-ϵ2.5 and 25-δ50-f0.3-ϵ3, and the yellow band includes those of the four 100 Mpc boxes.

The observations by Fan et al. (2006) suggest that the EoR ends at $z \sim 6$. The simulations which are most in agreement with this are CoDa II, 100-δ20-f0.3-ϵ5, 100-δ20-f0.25-ϵ6, 50-δ30-f0.25-ϵ2.5and 25-δ50-f0.5-ϵ1. However, having simulations which reionise slightly earlier and later than this will allow us to probe the effects of the timing of the EoR on the tSZ signal.

Global Photoionisation Rate

The lines and coloured bands in Figure 3.3 represent the same simulations as those in the plots of the reionisation histories. The evolution of the mean photoionisation rate of the simulations, save for the 10 Mpc boxes, roughly follow the same pattern as the reionisation histories. The boxes which are quick to reionise have higher photoionisation rates as their background UV flux densities are higher. More ionising photons in the IGM allows for reionisation to proceed more rapidly in these runs. Conversely, the simulations that reionise later have lower rates of photoionisation.

Around $z \sim 6$, there is a noticeable upturn in the slopes. This corresponds to the end of reionisation, where there is a drop in ionising photon absorption as the neutral hydrogen in the boxes are ionised, increasing the background UV flux. While the slopes match the pattern of the observational data, most of the simulations overshoot the observations. This discrepancy is responsible for those simulations having neutral fractions lower than those observed. However, the blue band of 25 Mpc simulations which best match with the neutral fraction observations also agree with the observed data for the photoionisation rates.

Optical Depth to Reionisation

We used `seren3` to estimate the optical depth to reionisation. `seren3` interpolates the ionisation fraction of helium based on Iliev et al. (2005). It assumes that, if the ionisation fraction of hydrogen is above 0.95 between $3 < z \leqslant 6$, then helium is singly-ionised; and helium is doubly-ionised if the hydrogen ionisation fraction is above 0.95 below $z = 3$. It then integrates the electron number density from $z = 0$ to $z = 99$ to obtain the optical depth.

Figure 3.4 shows the Thomson-scattering optical depth to reionisation for our simulations, as well as the Planck CMB optical depth, $\tau = 0.054 \pm 0.007$ (grey line and shaded area; Planck Collaboration et al., 2018a). Again, the lines and coloured bands represent the same simulations as in the previous graphs. The optical depth is a direct indicator of

the end of reionisation, and as such, the plots roughly reflect this. The boxes which are later to reionise have lower optical depths, as there is less free electrons in the IGM along the line of sight between the end of the EoR and the present day; and vice versa. The simulations whose optical depths fall into the 1σ range of the Planck 2018 measurement are 100-δ20-f0.3-ϵ8, 25-δ30-f0.2-ϵ4 and 10-δ200-f0.25-ϵ3.5-η15. The other simulations fall lower than this threshold, with $\tau \sim 0.040 - 0.047$. This is somewhat unavoidable, since a later end of reionisation will produce a lower optical depth.

Global Star Formation Rate Density

In Figure 3.5, we present the evolution of the global star formation density. The grey shaded area shows the dust-corrected and dust-uncorrected star formation rate (SFR) densities from Bouwens et al. (2015). Here, the rose-brown band represents the values for 25-δ30-f0.1-ϵ4, 25-δ30-f0.14-ϵ4 and 25-δ30-f0.2-ϵ4, the blue band represents those for 25-δ30-f0.2-ϵ2, 25-δ30-f0.2-ϵ2-η15, 25-δ30-f0.25-ϵ2.5 and 25-δ50-f0.3-ϵ3, and the yellow band represents the four 100 Mpc simulations. We see, like the observations, the general trend of the SFR densities for all simulations increases at all times.

The variation in the SFR of the simulations is mainly governed by the parameters $\delta_\star$ and $\epsilon_\star$. Since $\delta_\star$ indicates the minimum gas over-density required to trigger star birth, its value is tied to the spatial resolution of the box. Setting $\delta_\star$ too high will result in fewer stars being formed since the simulation will be unable to resolve many high-density gas clouds in its grid. On the other hand, low $\epsilon_\star$ values will result in a too low SFR, as it causes the gas to be poorly converted into stars. Hence, we must play a balancing act between these two parameters in order to get the SFR to correspond with the observational data.

Unlike the previous plots, the SFR by itself does not directly indicate the progression of the EoR, i.e. the relationship between them is not as straightforward. The amount of ionising photons emitted into the IGM by the stellar population is dictated by the value of $f_{\mathrm{esc},\star}$. This parameter can be adjusted to ensure that the timing of the EoR coincides with observations. Thus, it is possible for a simulation to have a low SFR but still complete reionisation at a reasonable time. For example, 25-δ50-f0.5-ϵ1 has one of the lowest SFRs, due to its high $\delta_\star$ and low $\epsilon_\star$, but because its $f_{\mathrm{esc},\star}$ is quite high, a greater proportion of photons are emitted into the IGM per stellar particle, increasing the photoionisation rate, and allowing reionisation to end at $z \sim 6$. Another example of how the SFR history alone does not govern the timing of the EoR is the fact that the simulations which have similar SFR histories (grouped together in the three coloured bands) end reionisation at different

times. Within each coloured band, there are simulations which finish reionising as early as $z \sim 6.5$ and those which complete reionisation as late as $z \sim 5.5$. Again, this is a direct result of the different $\delta_\star$, $\epsilon_\star$ and $f_{\mathrm{esc},\star}$ parameters used for them.

We see that increasing η_{SN} by 5% has only a small influence on the EoR, and a negligible change in the SFR. 25-δ30-f0.2-ϵ2 completes reionisation slightly sooner ($z \sim 5.8$) than 25-δ30-f0.2-ϵ2-η15 ($z \sim 5.7$), and their SFR density histories are almost identical. Hence, this small increase in supernova feedback minimally influences the reionisation process.

We also note the high SFR of CoDa II. In addition to the different values used for $\delta_\star$, $\epsilon_\star$ and $f_{\mathrm{esc},\star}$, CoDa II has different simulation settings compared to the others. One of these differences is the switching off of the temperature threshold for star formation. By turning off this setting, all cells, regardless of their temperature, are eligible for star formation if they are above the density threshold. This means that the conditions for star formation are solely based on $\delta_\star$ and $\epsilon_\star$. This results in there being more regions where star formation is possible. While radiative suppression of star formation still occurs in CoDa II, it is not as intense as it would be if the temperature threshold was turned on. This is one of the reasons why CoDa II is not always comparable to the other simulations.

3.3 Methodology

3.3.1 Electron Pressure Lightcones

RAMSES comes with an array of post-processing tools for a variety of languages, including Fortran and Python. The tool which we used for this study is `amr2cube`. This code reads the AMR output files and creates a 3D Cartesian cube of one of the gas variables: x-, y- or z- velocity component, density, pressure, ionisation fraction, and metallicity. We can then use the necessary cubes to perform our calculations.

For CoDa II, we used full-box, reduced-resolution cubes of the hydrodynamic properties. These cubes were already constructed as part of the CoDa II project and already available for us to use. For the other simulations, we used full-resolution cubes which we generated using the `amr2cube` utility. For the latter, we used the volume-weighted gas pressure and ionisation fraction, whereas for CoDaII we used the available volume-weighted gas pressure and mass-weighted ionisation fraction files. These fields were used to calculate the Comptonisation parameter y (Equation 1.29). In order to do this, we constructed lightcones of the electron pressure. Assuming purely hydrogen gas, the electron pressure is $p_{\mathrm{e}} = \frac{x_{\mathrm{HII}}}{1+x_{\mathrm{HII}}} p_{\mathrm{gas}}$. We derive this expression later, in Section 3.3.4.

When making the lightcone, let us consider a photon travelling along a line of sight, cell by cell, from redshift z_1 at the start of the lightcone to z_e at the end. The age of the universe, t_1, at z_1 can be calculated (see Equation 30 in Hogg, 1999). We then convert the cell size from comoving length to physical length by using the scale factor a_1, at redshift z_1, and thus calculate the time it will take the photon to cross the cell, dt. The age of the universe after this cell crossing is now $t_i = t_1 + dt$. Assuming an Einstein-de Sitter universe, the photon is now at redshift $z_i = (1 + z_1)\left(\frac{t_1}{t_i}\right)^{\frac{2}{3}} - 1$. We can now calculate the electron pressure of the cell at z_i by interpolating the data at the snapshots on either side of this redshift, say z_1 and z_2 corresponding to snapshots 1 and 2, respectively.

The electron pressure is interpolated using a Sigmoid function given by

$$p_{ei} = (1 - g)p_{e1} + gp_{e2}, \tag{3.1}$$

where p_{ei} is the interpolated electron pressure at z_i, and p_{e1} and p_{e2} are the electron pressure of the cell at z_1 and z_2 (snapshots 1 and 2), respectively. The factor g is

$$g = \frac{1}{1 + \mathrm{e}^{-\beta z_p}}, \tag{3.2}$$

where $\beta = 2$ and $z_p = -10 + 20\left(\frac{z_i - z_2}{z_1 - z_i}\right)$. We then repeat the process, calculating the cell size at z_i, the time taken for the photon to cross it, and so on. This allows us to obtain a lightcone of the electron pressure: a 3D grid of the field where each slice in the direction of light propagation reflects the state of the universe at that moment in time.

After the lightcone is constructed, we perform an integration in order to obtain the Comptonisation parameter, y. For each light crossing, we numerically integrate the pressure over all lines of sight along each axis and along the direction of light propagation using the composite Simpson's rule. As we calculated the time intervals between each cell in the lightcone (dt) during the interpolation process, we use these values for dt in the integral. In order to avoid artificial amplification of the y-parameter due to structural repetition, the box was randomly shifted and rotated during the integration stage. From this, we obtained a 2D grid of the y-parameter.

With the exception of the 10 Mpc boxes, we created lightcones for the same range of redshift for each simulation, i.e. $z \sim 6$ to 12, corresponding to the duration of the EoR. As the 10 Mpc boxes were not run to redshift 6, we constructed lightcones from their last snapshots to $z \sim 12$. In the case of 10-δ200-f0.2-ϵ3.5, this was in the range of $z \sim 6.38$ to 12, and for 10-δ200-f0.25-ϵ3.5-η15, this was $z \sim 6.74$ to 12.

For CoDa II, the lightcone comprised of 17.2 light crossings through the box, from snapshots 32 to 88. For the 50-δ30-f0.25-ϵ2.5 box, the lightcone was made of 21.4 light

Table 3.3: Summary of lightcone parameters.

Simulation	Snapshot number		Redshift		Number of
	start	end	start	end	light crossings
CoDa II	32	88	12.11	5.99	17.2
100-δ20-f0.25-ϵ3.5	27	72	12.13	6.00	10.9
100-δ20-f0.3-ϵ5	27	73	12.13	6.01	10.8
100-δ20-f0.25-ϵ6	27	73	12.13	6.00	10.8
100-δ20-f0.3-ϵ8	27	73	12.13	6.01	10.8
50-δ30-f0.25-ϵ2.5	32	88	11.95	5.98	21.4
10-δ200-f0.2-ϵ3.5	32	81	12.10	6.38	97.8
10-δ200-f0.25-ϵ3.5-η15	32	75	12.10	6.74	88.4
25-δ30-f0.1-ϵ4	41	119	12.01	5.98	44.0
25-δ30-f0.14-ϵ4	41	119	12.05	5.99	44.1
25-δ30-f0.2-ϵ4	41	119	12.06	6.00	44.0
25-δ30-f0.2-ϵ2	41	116	12.02	6.00	43.8
25-δ30-f0.2-ϵ2-η15	41	119	12.02	6.00	43.9
25-δ30-f0.25-ϵ2.5	41	116	12.06	6.00	44.0
25-δ50-f0.3-ϵ3	41	115	12.02	6.00	43.8
25-δ50-f0.5-ϵ1	41	109	12.00	6.01	43.6

crossings, from snapshots 32 to 88. The 100 Mpc boxes produced lightcones of ~ 10.8 light crossings. The reduced redshift range of the 10 Mpc boxes resulted in lightcones of ~ 97.8 (10-δ200-f0.2-ϵ3.5) and ~ 88.4 (10-δ200-f0.25-ϵ3.5-η15) light crossings. The parameters for the lightcones are summarised in Table 3.3.

We present the results in the form of maps of the y-parameter, probability density functions of y and angular power spectra of the signal in Chapter 4. The maps are simply the images of the 2D y-parameter grids obtained from the integration. We plot the full-resolution results along with smoothed maps. For smoothing, we apply Gaussian beams with FWHM of 1.2 arcmin and 1.7 arcmin. These beams correspond to the resolution of the South Pole Telescope (SPT)[7] (Carlstrom et al., 2011) at 150 GHz and 95 GHz, respectively. We do not use the SPT 220 GHz beam as the tSZ effect disappears near this frequency. To smooth the data, we converted the angular resolutions of the beams to comoving Mpc at the redshift of the lightcone at the end of each light crossing. Then, we

[7] https://pole.uchicago.edu/

calculated the number of cells spanning this size and use this value as our FWHM for the Gaussian beam. As angular size varies negligibly at high redshifts, we ignore this effect when constructing the lightcones. If one were to take this into account, they would have to construct the lightcones in such a way to include the scale of the cells with distance.

We also plot the distributions of the y-parameter for each redshift of the lightcone for CoDa II in order to determine the period when most of the signal appears during reionisation. For these PDFs, we plot the distribution of the y-values for the start of the lightcone to each redshift, i.e. from $z \sim 12$ to 11, $z \sim 12$ to 10, etc. We compute the angular power spectra of the maps and present them with the Shaw et al. (2010) power spectrum template scaled to fit the cosmological parameters as done by George et al. (2015), and the SPT observations of the total CMB power spectrum at the 95 GHz and 150 GHz bandpowers.

3.3.2 Density Lightcones

Since the electron pressure is dependent upon the gas density, temperature and ionisation fraction, we investigated the contributions of these fields to the y-parameter for CoDa II. To do this, we used the volume-weighted gas density and mass-weighted ionisation fraction. We first removed the fluctuations in the temperature field by using a fixed global value for the temperature, $T_\mathrm{e} = 30,000$ K. We then constructed an electron density lightcone via the same steps as for the electron pressure lightcones in Section **??** for the redshift range $z \sim 6$ to 12, and using the expression

$$\rho_\mathrm{e} = \frac{x_\mathrm{HII}}{1 + x_\mathrm{HII}} \rho_\mathrm{gas} \tag{3.3}$$

for the electron density.

After the lightcone was constructed, we numerically integrated the electron density over all lines of sight along each axis and along the direction of light propagation, as before. The integral for the density lightcone becomes

$$y = \frac{\sigma_\mathrm{T} k_\mathrm{B}}{m_\mathrm{e} m_\mathrm{p} c} T_\mathrm{e} \int \frac{x_\mathrm{HII}}{1 + x_\mathrm{HII}} \rho_\mathrm{gas} \, \mathrm{d}t, \tag{3.4}$$

where m_p is the proton mass and comes from converting the electron mass density to number density $\left(n_\mathrm{e} = n_\mathrm{HII} = \frac{\rho_\mathrm{HII}}{m_\mathrm{p}}\right)$. We also randomly shifted and rotated the box to avoid artificially boosting the signal. Again, this gave us a 2D grid of y-parameter values for the box.

Next, we removed the patchiness of the EoR in addition to the temperature fluctuations, by using a globally averaged value of the ionisation fraction for each light crossing.

We made a lightcone of gas density using only the volume-weighted gas density files for CoDa II for the interpolation process, for the redshift range $z \sim 6$ to 12.

In this case, Equation 3.4 becomes

$$y = \frac{\sigma_{\mathrm{T}} k_{\mathrm{B}}}{m_{\mathrm{e}} m_{\mathrm{p}} c} T_{\mathrm{e}} \langle x_{\mathrm{HII}} \rangle \int \rho_{\mathrm{gas}} \, \mathrm{d}t, \tag{3.5}$$

where $\langle x_{\mathrm{HII}} \rangle$ is the globally averaged ionisation fraction. This average ionisation fraction came from the `averages.txt` file. We used the value of $\langle x_{\mathrm{HII}} \rangle$ from this file which corresponded to the redshift of the box at the end of each light crossing. Once again, we randomly shifted and rotated the box during integration, obtaining a 2D map of the y-parameter.

We present the results of this part of the investigation in a plot of the PDFs of the Comptonisation parameter and compare them to those calculated using the electron pressure lightcone for CoDa II in Chapter 4.

3.3.3 Tests

Analytic Check

In order to determine whether our results were realistic, we made a pen-on-paper prediction for the y-parameter. As part of our assumptions concerning the IGM, we assumed that reionisation was instantaneous, the temperature of the IGM had a uniformed average value, and the density of the IGM was also uniform and scaled with redshift. We do not consider the temperature as changing with redshift in our assumption since during the redshift range considered ($z = 12$ to $z = 6$), the universe does not expand significantly enough to result in a noticeable amount of cooling.

To perform the calculation, we consider Equation 1.29. As we are concerned with the redshift evolution of the IGM density, we must rewrite the integral with respect to redshift. We start with the Friedmann equation:

$$H^2 = \left(\frac{\dot{a}}{a}\right)^2 = H_0^2 \left[\Omega_{\mathrm{r},0} \left(1+z\right)^4 + \Omega_{\mathrm{m},0} \left(1+z\right)^3 + \Omega_{\mathrm{k},0} \left(1+z\right)^2 + \Omega_{\Lambda,0}\right]. \tag{3.6}$$

For a flat universe, $\Omega_{\mathrm{k},0} = 0$. At the EoR, $\Omega_{\mathrm{r},0} \sim 0$ and $\Omega_{\mathrm{m},0} \gg \Omega_{\Lambda,0}$. Thus, the Friedmann equation reduces to

$$\left(\frac{\dot{a}}{a}\right)^2 = H_0^2 \left[\Omega_{\mathrm{m},0} \left(1+z\right)^3\right]. \tag{3.7}$$

But $a = (1+z)^{-1}$ and $\dot{a} = -(1+z)^{-2} \frac{\mathrm{d}z}{\mathrm{d}t}$. Substituting these into Equation 3.7 and rearranging to make $\mathrm{d}t$ the subject, we get

$$\mathrm{d}t = -\frac{1}{H_0 \Omega_{\mathrm{m},0}^{\frac{1}{2}}} (1+z)^{-\frac{5}{2}} \, \mathrm{d}z. \tag{3.8}$$

Substituting Equation 3.8 into Equation 1.29 gives us

$$y = -\frac{\sigma_{\mathrm{T}}}{m_{\mathrm{e}}c^2}\frac{1}{H_0\Omega_{\mathrm{m},0}^{\frac{1}{2}}}\int p_{\mathrm{e}}\,(1+z)^{-\frac{5}{2}}\,c\mathrm{d}z. \tag{3.9}$$

Assuming the IGM is an ideal gas, $p_{\mathrm{e}} = k_{\mathrm{B}} n_{\mathrm{e}} T_{\mathrm{e}}$, where n_{e} and T_{e} are the electron number density and temperature, respectively. For purely hydrogen gas, the electron number density is

$$n_{\mathrm{e}} = n_{\mathrm{HII}} \tag{3.10}$$

$$= \frac{\rho_{\mathrm{HII}}}{m_{\mathrm{H}}} \tag{3.11}$$

$$= x_{\mathrm{HII}}\frac{\rho_{\mathrm{gas}}}{m_{\mathrm{H}}}. \tag{3.12}$$

For instantaneous reionisation, x_{HII} can only be either 0 or 1 if neutral or ionised, respectively. Hence,

$$n_{\mathrm{e}} = \frac{\rho_{\mathrm{gas}}}{m_{\mathrm{H}}}. \tag{3.13}$$

The density of our uniform IGM is described by the expression

$$\rho_{\mathrm{gas}} = \rho_0\Omega_{\mathrm{b},0}\,(1+z)^3\,, \tag{3.14}$$

where $\rho_0 = 10^{-30}$ g cm^{-3} is the mean density of the universe at $z = 0$.

Equation 3.13 now becomes

$$n_{\mathrm{e}} = \frac{\rho_0}{m_{\mathrm{H}}}\Omega_{\mathrm{b},0}\,(1+z)^3\,. \tag{3.15}$$

Converting the integrand from electron pressure to density for an ideal gas, we get

$$y = -\frac{\sigma_{\mathrm{T}}k_{\mathrm{B}}}{m_{\mathrm{e}}m_{\mathrm{H}}c}\frac{\rho_0\Omega_{\mathrm{b},0}}{H_0\Omega_{\mathrm{m},0}^{\frac{1}{2}}}T_{\mathrm{e}}\int (1+z)^{\frac{1}{2}}\,\mathrm{d}z. \tag{3.16}$$

Evaluating this integral for the redshift range of the lightcones ($z = 12$ to 6) and the cosmological parameters for CoDa II, and assuming an IGM temperature of 30,000 K, we obtain a Comptonisation parameter $y = 4.22 \times 10^{-8}$. This value acts as a lower limit value we expect to get, since we omit temperature fluctuations, ignoring the the fact that supernovae will heat regions of the IGM to millions of K, density fluctuations, and patchy reionisation. For the auxiliary simulations, this is $y = 4.18 \times 10^{-8}$.

Helium Reionisaton

So far, we have assumed that the baryonic matter is comprised of hydrogen only, ignoring helium and metals. While the presence of metals is insignificant to this study, the presence

of helium will contribute to the tSZ signal. Neutral helium (He I) requires photons with energy of at least 24.6 eV to be singly ionised to He II, with He II recombining at roughly the same rate as H II. However, He II requires photons of at least 54.4 eV energy to be fully ionised to He III, with a recombination rate $\geqslant 5$ times that of hydrogen. Thus, when accounting for the presence of helium, the sources that ionise hydrogen are also considered to singly ionise helium. On the other hand, the second ionisation of helium occurs at later redshifts, with the reionisation of helium ending at $z \sim 3$ (Barkana and Loeb, 2001).

Therefore, during the redshift range considered in this study, each helium atom will contribute one electron to the IGM. Equation 3.10 thus becomes

$$n_{\rm e} = n_{\rm HII} + n_{\rm HeII}, \tag{3.17}$$

where $n_{\rm HeII}$ is the number density of singly-ionised helium. When accounting for doubly-ionised helium, the term $2n_{\rm HeIII}$ is added.

Assuming the primordial abundances of hydrogen and helium by mass ($X = 0.76$ and $Y = 0.24$, respectively), and ignoring any isotopes, we get

$$n_{\rm e} = x_{\rm HII} X \frac{\rho_{\rm gas}}{m_{\rm H}} + x_{\rm HeII} Y \frac{\rho_{\rm gas}}{4 m_{\rm H}} \tag{3.18}$$

$$= \left(x_{\rm HII} X + x_{\rm HeII} \frac{Y}{4} \right) \frac{\rho_{\rm gas}}{m_{\rm H}}, \tag{3.19}$$

where $x_{\rm HeII} = \frac{n_{\rm HeII}}{n_{\rm He}}$ is the ionisation fraction of singly ionised helium. For instantaneous reionisation, $x_{\rm HII}$ and $x_{\rm HeII}$ immediately change from 0 to 1, and Equation 3.13 becomes

$$n_{\rm e} = 0.82 \frac{\rho_{\rm gas}}{m_{\rm H}}. \tag{3.20}$$

This results in an 18% decrease in the tSZ signal, when compared to a hydrogen-only scenario. The Comptonisation parameters for CoDa II and the auxiliary simulations therefore become $y \approx 3.46 \times 10^{-8}$ and $y \approx 3.43 \times 10^{-8}$, respectively.

In addition, RAMSES-CUDATON tracks the ionisation and cooling processes of atomic hydrogen only. In doing so, it assumes that hydrogen makes up 76% of the baryonic matter, thus preserving its primordial abundance. Nevertheless, the temperature field generated by the simulation is given in units of $\mathrm{K}\mu^{-1}$, as $T_\mu = \frac{T}{\mu}$, where μ is the mean molecular weight. As μ depends on the ionisation fractions,

$$\frac{1}{\mu} = \left(1 + x_{\rm HII}\right) X + \left(1 + x_{\rm HeII} + 2 x_{\rm HeIII}\right) \frac{Y}{4}, \tag{3.21}$$

the temperature field (and, hence, the pressure field) can be updated, in post-processing, to roughly account for helium reionisation, by interpolating μ along a given redshift range.

Phase Diagrams

In order to probe the underlying quantities responsible for the y-parameter values for the simulations, we plot phase diagrams of the gas temperature and density. As the electron pressure is dependent on these quantities, we will be able to better understand the trends in our results. We present these phase diagrams and an interpretation of them with respect to the y-parameter values in Section 4.3.

3.3.4 Electron Pressure

Unfortunately, we initially made the assumption that, for an ideal monatomic (hydrogen only) gas, the electron pressure of the ionised plasma would be the same as the plasma pressure, i.e. $p_{\rm e} = p_{\rm plasma}$. In doing so, we used the expression

$$p_{\rm e} = x_{\rm HII}\ p_{\rm gas} \tag{3.22}$$

for the electron pressure when constructing our lightcones for CoDa II and the seven auxiliary simulations in Section 3.2.2, with the expectation that this would give us an electron pressure which was appropriately proportional to the ionised state of the IGM, e.g. $p_{\rm e} = 0$ for neutral regions ($x_{\rm HII} = 0$).

The result of this assumption was that the PDFs of the y-parameter values for CoDa II were much higher (by approximately half an order of magnitude) than the others, while the PDFs of the other simulations were almost perfectly in agreement. We initially thought that this was a resolution effect. CoDa II has the highest grid resolution and, with the exception of the 10 Mpc boxes, the highest spatial resolution. To test if this was indeed the cause, we coarsened the y-parameter map for CoDa II to correspond to the grid resolution of the other simulations, i.e. 1024×1024. To do this, we took the mean of every 2×2 cells. We then compared the PDF of the coarsened map with that of the full-resolution map. However, this only had the effect of removing part of the high-end tail of the distribution while the rest of the distribution did not shift.

At this point, one of our collaborators noticed that the files for the ionisation fraction in CoDa II, *xion*, were not actually the ionisation fractions, but 1 + the ionisation fraction. We recalculated the y-parameter for CoDa II using $x_{\rm HII} = 1 - xion$. This shifted the distribution lower (to the left) but not enough for CoDa II to be in agreement with the other boxes.

Eventually, one of our collaborators pointed out that the assumption which we made for the electron pressure was inaccurate and ignores the other particles in the IGM. In

order to determine an accurate expression for the electron pressure, we must consider that the ionised gas contains electrons as well as ionised and neutral hydrogen which also contribute to the pressure:

$$p_{\rm gas} = p_{\rm total} = p_{\rm e} + p_{\rm HII} + p_{\rm HI}. \tag{3.23}$$

$p_{\rm e} = p_{\rm HII}$, so the right hand side becomes $2p_{\rm e} + p_{\rm HI}$. For an ideal gas, $p = nk_{\rm B}T$. Also, $n_{\rm HI} = (1 - x_{\rm HII})\, n_{\rm H}$ (similarly, $n_{\rm e} = x_{\rm HII} n_{\rm H}$), where $n_{\rm H}$ is the total (ionised + neutral) hydrogen. Therefore, the gas pressure is

$$p_{\rm gas} = 2p_{\rm e} + (1 - x_{\rm HII})\, n_{\rm H} k_{\rm B} T. \tag{3.24}$$

We can rewrite this in terms of the electron number density:

$$\begin{aligned} p_{\rm gas} &= 2p_{\rm e} + \frac{1 - x_{\rm HII}}{x_{\rm HII}} n_{\rm e} k_{\rm B} T && (3.25)\\ &= 2p_{\rm e} + \frac{1 - x_{\rm HII}}{x_{\rm HII}} p_{\rm e} && (3.26)\\ &= \frac{1 + x_{\rm HII}}{x_{\rm HII}} p_{\rm e}. && (3.27) \end{aligned}$$

Thus, we obtain our expression for electron pressure

$$p_{\rm e} = \frac{x_{\rm HII}}{1 + x_{\rm HII}} p_{\rm gas}. \tag{3.28}$$

Applying this to our calculations remedied the discrepancies between the CoDa II y-parameter results and those of the other simulations. The results of these assumptions and attempted corrections are presented in the next chapter.

Singly-Ionised Helium

Including the presence of neutral and singly-ionised helium in our estimations, Equation 3.23 becomes

$$p_{\rm gas} = p_{\rm e} + p_{\rm HII} + p_{\rm HI} + p_{\rm HeII} + p_{\rm HeI}. \tag{3.29}$$

In this case, $p_{\rm e} = p_{\rm HII} + p_{\rm HeII}$. Thus,

$$\begin{aligned} p_{\rm gas} &= 2p_{\rm e} + n_{\rm HI} k_{\rm B} T + n_{\rm HeI} k_{\rm B} T && (3.30)\\ &= 2p_{\rm e} + \left[(1 - x_{\rm HII})\, X \frac{\rho_{\rm gas}}{m_{\rm H}} + (1 - x_{\rm HeII})\, Y \frac{\rho_{\rm gas}}{4 m_{\rm H}} \right] k_{\rm B} T && (3.31)\\ &= 2p_{\rm e} + \left[(1 - x_{\rm HII})\, X + (1 - x_{\rm HeII}) \frac{Y}{4} \right] k_{\rm B} T \frac{\rho_{\rm gas}}{m_{\rm H}} && (3.32)\\ &= 2p_{\rm e} + \left[(1 - x_{\rm HII})\, X + (1 - x_{\rm HeII}) \frac{Y}{4} \right] \mu p_{\rm gas}. && (3.33) \end{aligned}$$

Substituting the expression for the mean molecular weight (Equation 3.21) and assuming $x_{\rm HeIII} = 0$, the expression for the electron pressure becomes

$$p_{\rm e} = \frac{1}{2}\left[1 - \frac{(1 - x_{\rm HII})\,X + (1 - x_{\rm HeII})\,\frac{Y}{4}}{(1 + x_{\rm HII})\,X + (1 + x_{\rm HeII})\,\frac{Y}{4}}\right] p_{\rm gas}. \tag{3.34}$$

3.4 CoDa I

CoDa II is the successor to a previously run simulation, Cosmic Dawn (hereafter, referred to as CoDa I; Ocvirk et al., 2016). At the time the latter was run, it was the largest GPU-accelerated, fully coupled radiation hydrodynamic simulation. However, due to its low star formation efficiency, CoDa I ended reionisation late, at $z \lesssim 5$. CoDa II is an improvement on the previous simulation, using re-calibrated star formation parameters and a modified star formation algorithm, to ensure that the EoR ends $z = 6$. The cosmological parameters were also updated from a WMAP5 cosmology (Hinshaw et al., 2009) (CoDa I) to a cosmology consistent with Planck observations (Planck Collaboration et al., 2014) (CoDa II). CoDa I uses: $\Omega_\Lambda = 0.721$, $\Omega_m = 0.279$, $\Omega_b = 0.046$, $H_0 = 0.70$, and power spectrum normalisation $\sigma_8 = 0.817$ and slope $n = 0.96$. Unlike CoDa II, CoDa I employs the temperature threshold for star formation, with $T_\star = 2 \times 10^4$ K. We summarise the parameters used in CoDa I in Table 3.4.

In the initial stages of this study, CoDa I was the only simulation being analysed for the tSZ signal during the EoR. This is because the other simulations had either not been run yet or their data were not yet processed. We used the same method described above to calculate the tSZ signal for CoDa I, also using reduced-resolution (2048^3) cubes. However, we assumed that the electron pressure was as Equation 3.22, and the lightcone spanned the redshift range $z = 12.61$ - 4.23 to encompass all of the EoR. We present the results of this analysis in Section 4.5 for the purpose of being thorough.

Table 3.4: Summary of the simulation parameters used in CoDa I.

Setup	
Number of nodes (GPUs)	8192
Grid size	4096^3
Box size, $L_{\rm box}/h^{-1}$ Mpc	64
Grid cells per node	$128 \times 256 \times 256$
Spatial resolution, $\mathrm{d}x/h^{-1}$ kpc	22.2
DM particle number, $N_{\rm DM}$	4096^3
DM particle mass, $M_{\rm DM}/\mathrm{M}_\odot$	3.49×10^5
Initial redshift, $z_{\rm start}$	150
End redshift, $z_{\rm end}$	4.23
Number of snapshots	138
Physics parameters	
Density threshold, $\delta_\star$	$50\,\langle\rho\rangle$
Efficiency, $\epsilon_\star$	0.01
Mass fraction, $\eta_{\rm SN}$	10%
Stellar particle escape fraction, $f_{\rm esc,\star}$	0.5

Chapter 4

Results

4.1 Electron Pressure Lightcones

In this section, we present the main results of our study, the tSZ effect calculated from the electron pressure lightcones in Section 3.3.1. The mean y-parameter values, $\langle y \rangle$, for the sixteen simulations are listed in Table 4.1. All values of $\langle y \rangle$ obtained in this study are of order 10^{-8}, well below the COBE-FIRAS limit of $\langle y \rangle < 1.5 \times 10^{-5}$ (Fixsen et al., 1996), and two orders of magnitude lower than the total mean y-parameter estimated by Refregier et al. (2000); Zhang et al. (2004b); Hill et al. (2015). As galaxy clusters are the dominant contributions to this quantity ($\langle y \rangle_{\rm ICM} = 1.58 \times 10^{-6}$; Hill et al., 2015), this is expected. Compared with the reionisation contribution estimated by Hill et al. (2015) ($\langle y \rangle_{\rm EoR} = 9.8 \times 10^{-8}$), our values are slightly lower, but of the same order of magnitude. This discrepancy is most likely due to differences between our simulations and their reionisation model. Nevertheless, these values for the mean Comptonisation parameter for the EoR are comparable, and thus indicate that our results are reasonable estimations.

4.1.1 The tSZ Signal and the Timing of the EoR

To get a better understanding of these values, we plot the probability density functions (see Figure 4.1). There are two sets of simulations with overlapping PDFs, which we group together in two bands. The turquoise band includes the PDFs for 100-δ20-f0.3-ϵ5, 100-δ20-f0.25-ϵ6, 25-δ30-f0.1-ϵ4, 25-δ30-f0.2-ϵ2, 25-δ30-f0.2-ϵ2-η15 and 25-δ50-f0.5-ϵ1. These simulations have some of the lowest y-parameter values, and also are some of the latest to complete reionisation. The only simulation with a smaller tSZ signal is 100-δ20-f0.25-ϵ3.5, which is the box with the latest EoR. The coral band of PDFs include

Table 4.1: The mean Compton y-parameter for each simulation.

Simulation	$\langle \mathbf{y} \rangle \times \mathbf{10^8}$
CoDa II	3.67
100-δ20-f0.25-ϵ3.5	1.22
100-δ20-f0.3-ϵ5	1.96
100-δ20-f0.25-ϵ6	1.91
100-δ20-f0.3-ϵ8	2.70
50-δ30-f0.25-ϵ2.5	2.47
10-δ200-f0.2-ϵ3.5	2.62
10-δ200-f0.25-ϵ3.5-η15	2.46
25-δ30-f0.1-ϵ4	2.86
25-δ30-f0.14-ϵ4	2.18
25-δ30-f0.2-ϵ4	3.63
25-δ30-f0.2-ϵ2	1.97
25-δ30-f0.2-ϵ2-η15	2.03
25-δ30-f0.25-ϵ2.5	2.96
25-δ50-f0.3-ϵ3	3.09
25-δ50-f0.5-ϵ1	1.82

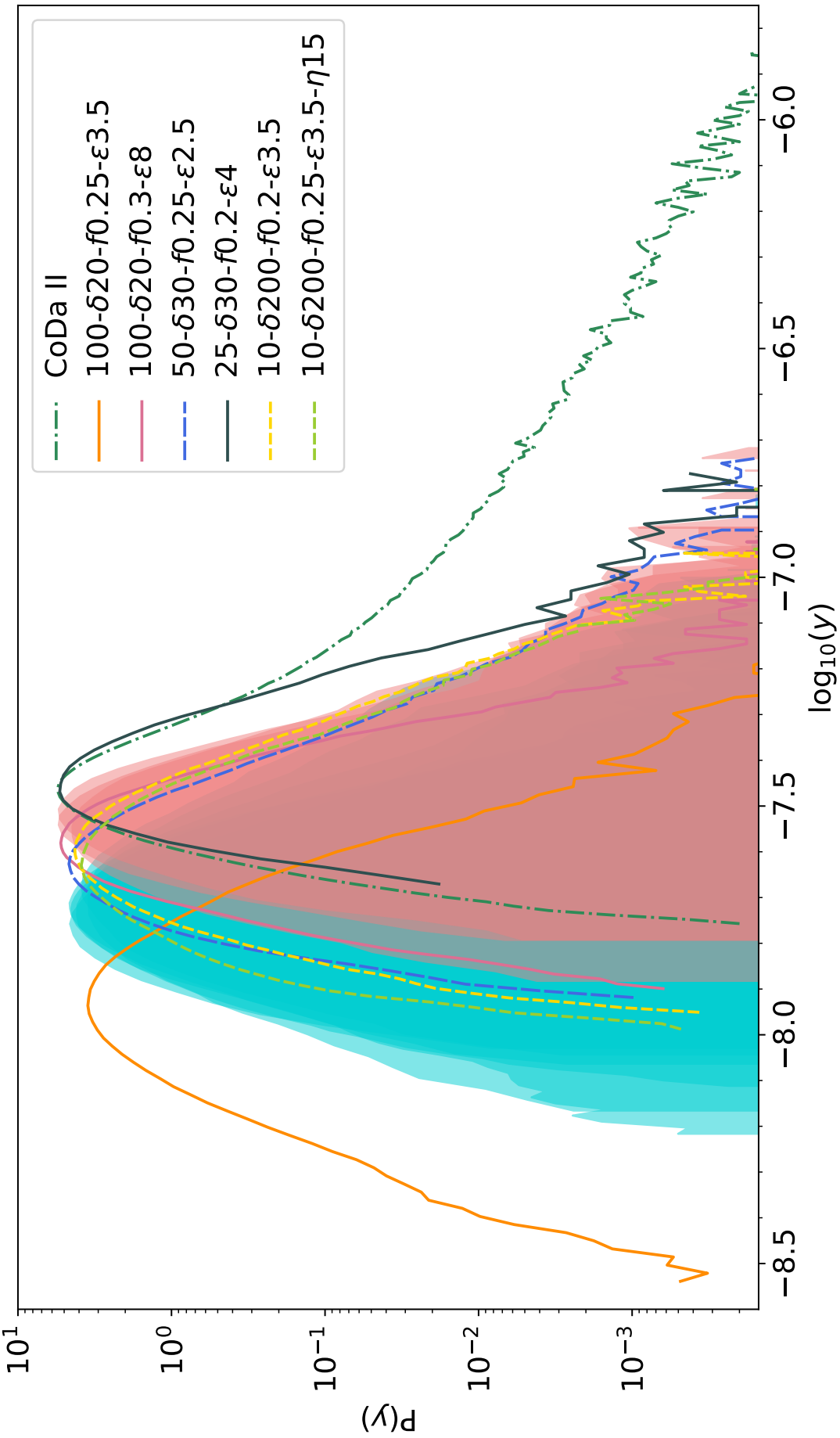

Figure 4.1: The distributions of the Compton y-parameter calculated from the electron pressure lightcones. The turquoise band includes the PDFs for 100-δ20-f0.3-ϵ5, 100-δ20-f0.25-ϵ6, 25-δ30-f0.1-ϵ4, 25-δ30-f0.2-ϵ2, 25-δ30-f0.2-ϵ2-η15 and 25-δ50-f0.5-ϵ1, and the coral band includes those for 25-δ30-f0.14-ϵ4, 25-δ30-f0.25-ϵ2.5 and 25-δ50-f0.3-ϵ3.

25-δ30-f0.14-ϵ4, 25-δ30-f0.25-ϵ2.5 and 25-δ50-f0.3-ϵ3. These are three of the 25 Mpc simulations whose EoRs occur earlier. 25-δ30-f0.2-ϵ4, the simulation with the earliest EoR, has the highest y-parameter values of the auxiliary simulations. Its PDF overlaps with that of CoDa II, save for the tail in the latter. The tail is a result of the high resolution in CoDa II, which can effectively resolve small, high-temperature regions around supernova explosions, which lead to tiny areas of high electron pressure. However, their reionisation histories are not the same, with 25-δ30-f0.2-ϵ4 reionising earlier ($z \sim 6.6$) than CoDa II ($z \sim 6.1$).

We also see that, when the EoR is earlier, the distributions of the y-parameters are narrower, as the gas has had more time to equilibrate, and there are less fluctuations in the ionised hydrogen fraction. These results indicate a link between the timing of the EoR and the magnitude of the tSZ effect stemming from that cosmic period. If reionisation ends earlier, the lightcone will have more free electrons for the same redshift range. Hence, there is higher electron pressure along the lines of sight when the EoR occurs earlier, resulting in a stronger tSZ effect.

In order to better visualise the relationship between the tSZ effect and the timing of the EoR, we plot the modal y-parameter value against the redshift when the average neutral hydrogen fraction reaches 10^{-3}, $z_{\langle x_{\rm HI}\rangle \sim 0.001}$, in Figure 4.2. We see that there is indeed a general trend, where the timing of the EoR influences the strength of its tSZ signal. However, this trend is not very strict. For instance, there are two distinct outliers: CoDa II and 10-δ200-f0.25-ϵ3.5-η15. For CoDa II, this is most likely due to the different simulation settings used in the run. For 10-δ200-f0.25-ϵ3.5-η15, the fact that its lightcone has the shortest redshift range can explain this anomaly, as extending the lightcone down to $z \sim 6$ would raise its modal y-parameter.

We also note some degeneracies in the modal y-parameter. While 25-δ30-f0.14-ϵ4 and 25-δ30-f0.25-ϵ2.5 have similar modal y-parameters, their end-of-reionisation redshifts differ. We also see that while 25-δ30-f0.2-ϵ2 reionises later than 25-δ50-f0.5-ϵ1, the latter has a slightly stronger tSZ signal. Conversely, 25-δ30-f0.2-ϵ4 and 25-δ50-f0.3-ϵ3 have similar $z_{\langle x_{\rm HI}\rangle \sim 0.001}$ values, but the latter has a higher modal y-parameter. As these boxes are all the same size and resolution, we can get a better understanding of the actual physics behind this.

In addition to their different EoR timings, these boxes have differing SFR histories. For two simulations with similar y-parameters but different EoR timings, the SFR of the simulation with a later EoR is higher than that of the one whose EoR ends earlier. This

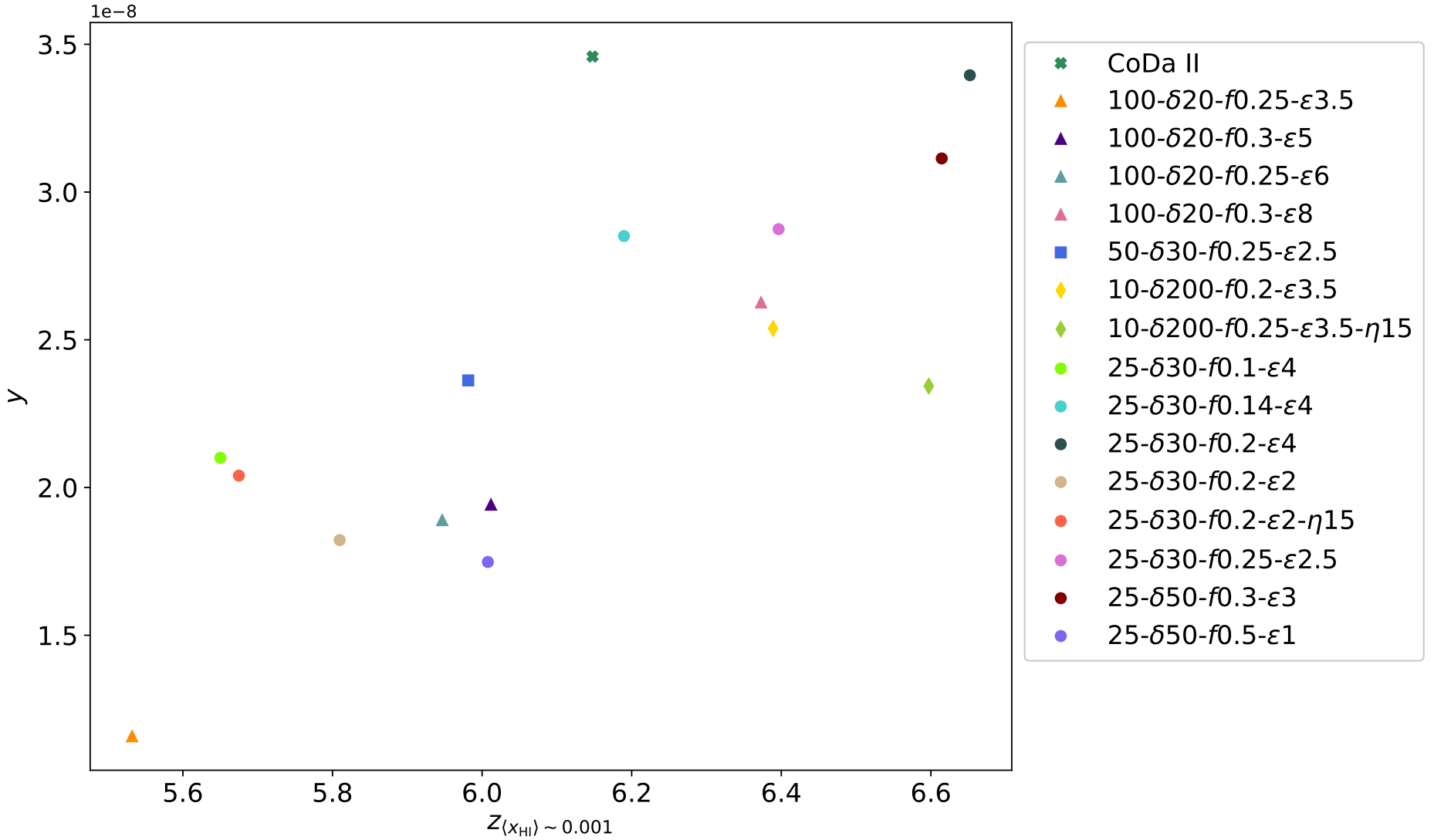

Figure 4.2: The modal y-parameter values calculated from the electron pressure lightcones plotted against the redshift when the mean neutral hydrogen fraction reaches $\langle x_{\rm HI}\rangle \sim 10^{-3}$.

suggests that, although a simulation may reionise later, if the SFR is relatively high, the tSZ effect is boosted. A higher SFR leads to more stars which then go supernova and raise the gas temperature. As the electron temperature increases, there will be more inverse Compton scattering.

We also see that, at $z_{\langle x_{\rm HI}\rangle\sim 0.001} \sim 6$, there is a small variation in the y-parameter modes of 50-δ30-f0.25-ϵ2.5, 100-δ20-f0.3-ϵ5, 100-δ20-f0.25-ϵ6 and 25-δ50-f0.5-ϵ1. The differences in these values can also be explained by the SFRs of the boxes, as well as resolution effects.

4.1.2 Impact on Galaxy Cluster Measurements

Another objective of this study is to probe the effect of the EoR tSZ signal on galaxy cluster measurements. Although the tSZ signal from the EoR is subdominant to that of clusters, we investigate how much error the former contributes toward the latter. To confirm this, we plot y-parameter maps (see Figures 4.3 - 4.6) and their angular power spectra (see Figure 4.7). For each simulation, we present the full-resolution map (left panel) and maps smoothed for Gaussian beams of FWHM 1.2 arcmin (middle panel) and 1.7 arcmin (right panel). The beam resolutions correspond to those of the 150 GHz and 95 GHz SPT channels, respectively. The angular power spectra of the full-resolution maps are plotted along with the Shaw et al. (2010) tSZ template (solid black line) and total CMB power spectrum measured by the SPT (George et al., 2015).

The fluctuations in the full-resolution maps are all in the sub-arcminute scale, with the largest y-parameters reaching $y \sim 10^{-6}$. When the maps are smoothed, these fluctuations grow to ~ 1 arcmin, and peak at $y \sim 10^{-8}$. On the other hand, the y-parameter of galaxy clusters is typically $y \gtrsim 10^{-5}$, and their angular size ranges from from tens of arcsec to tens of arcmin. From the power spectra, we see that, for cluster scales ($l \lesssim 10^4$), the EoR accounts for $< 1\%$ of the cluster signal. The power spectra of our maps are also flatter in shape than the Shaw et al. (2010) cluster template.

On smaller scales ($l > 10^4$), the tSZ signals from CoDa II and the 10 Mpc boxes become stronger. The power spectra of the other simulations do not share this feature as they have lower resolutions. Unfortunately, tSZ templates do not probe these scales, so we are unable to determine the significance of the EoR contribution on small scales. If the total tSZ signal drops by a few magnitudes in power at scales of a few arcsec or smaller, the EoR would become a more considerable source. Consequently, measurements of the tSZ effect on these scales could be used as a constraint for the EoR (for e.g., the timing

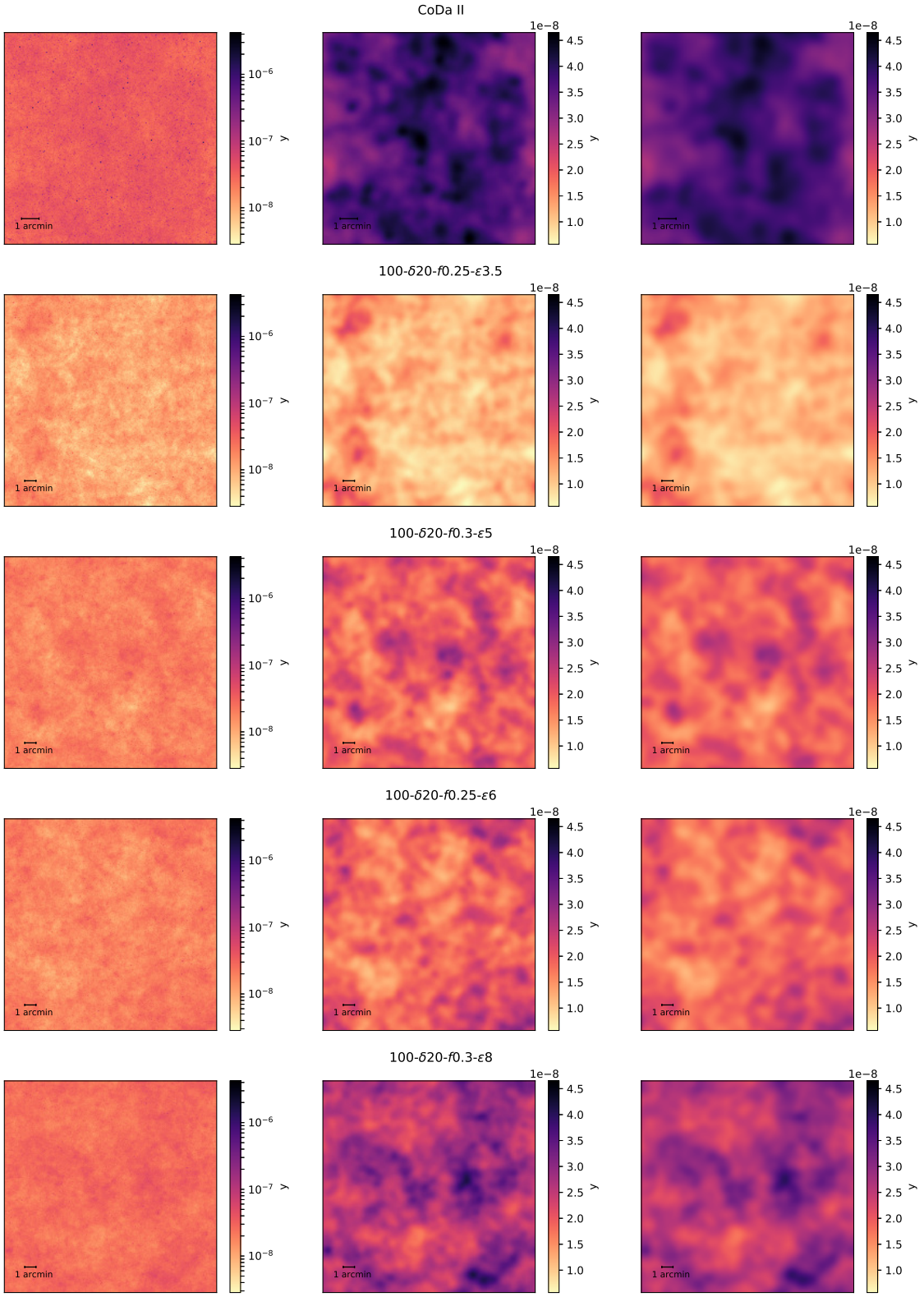

Figure 4.3: Full-resolution (left panel) and smoothed (middle and right panels) maps of the y-parameter for CoDa II and the four 100 Mpc boxes. Smoothed maps are constructed for a Gaussian beam of FWHM 1.2 arcmin (middle) and 1.7 arcmin (right), corresponding to the resolution of the 150 GHz and 95 GHz channels of the SPT, respectively.

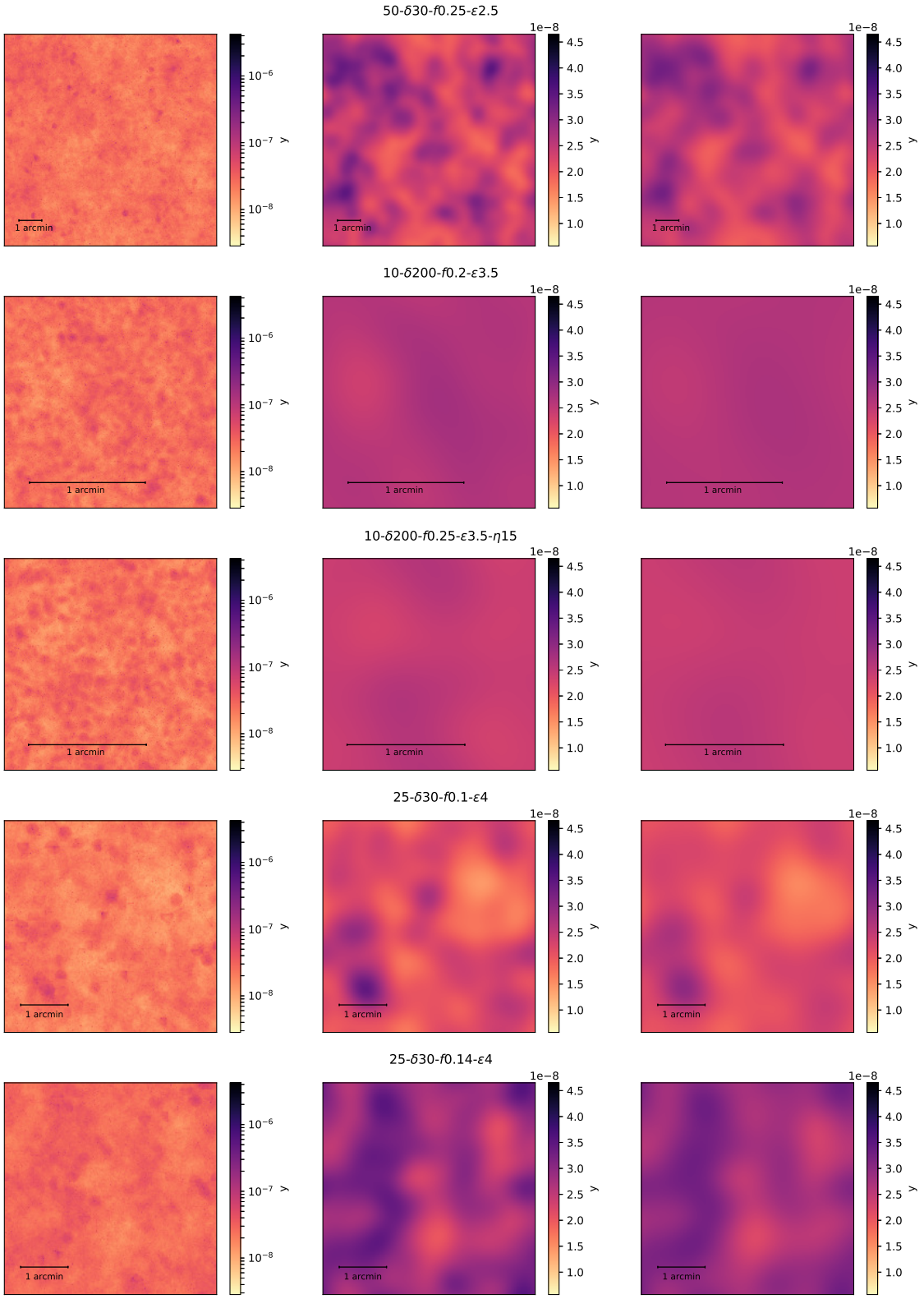

Figure 4.4: Full-resolution (left panel) and smoothed (middle and right panels) maps of the y-parameter for the auxiliary simulations as labelled. Smoothed maps are constructed for a Gaussian beam of FWHM 1.2 arcmin (middle) and 1.7 arcmin (right), corresponding to the resolution of the 150 GHz and 95 GHz channels of the SPT, respectively.

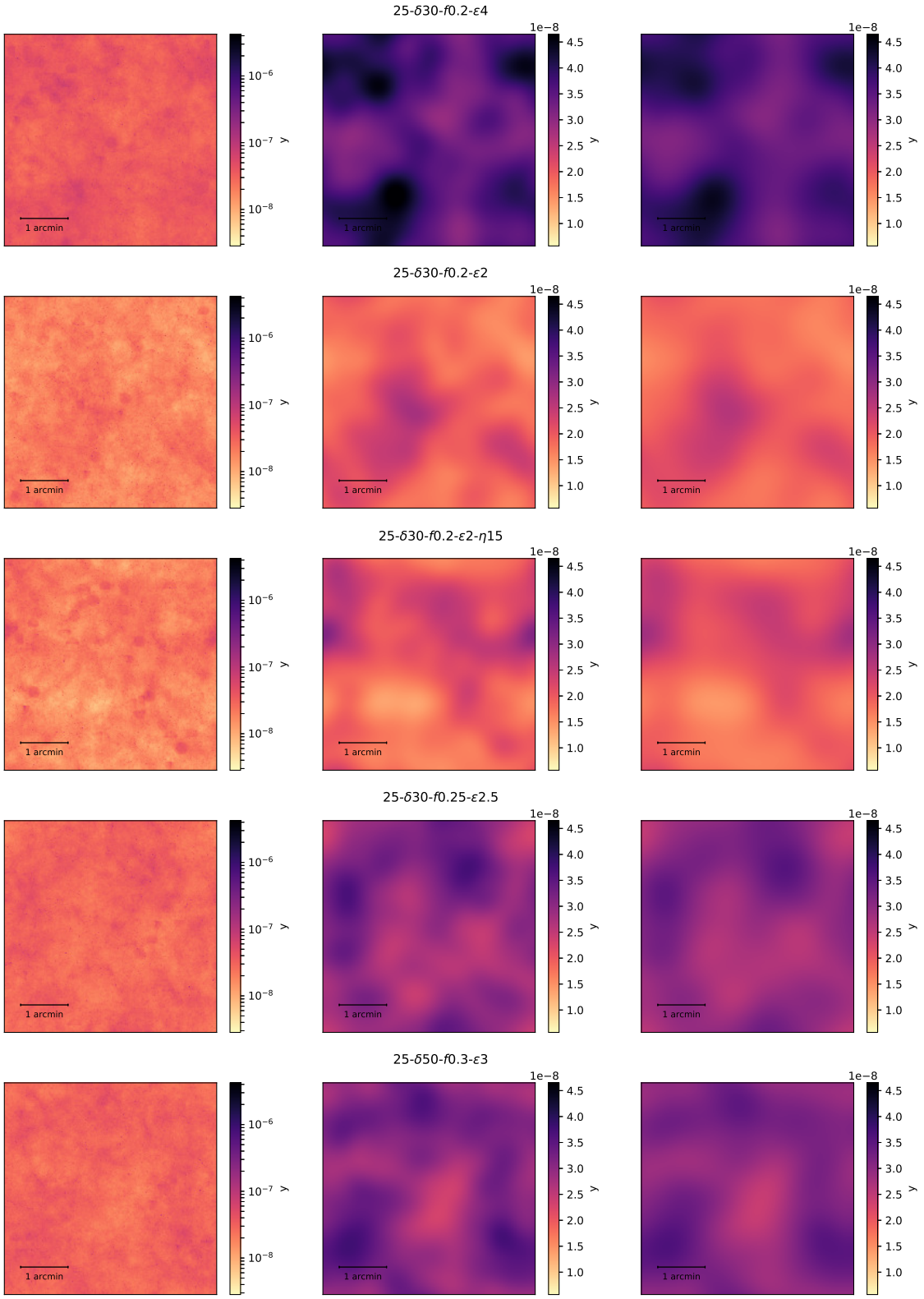

Figure 4.5: Full-resolution (left panel) and smoothed (middle and right panels) maps of the y-parameter for the auxiliary simulations as labelled. Smoothed maps are constructed for a Gaussian beam of FWHM 1.2 arcmin (middle) and 1.7 arcmin (right), corresponding to the resolution of the 150 GHz and 95 GHz channels of the SPT, respectively.

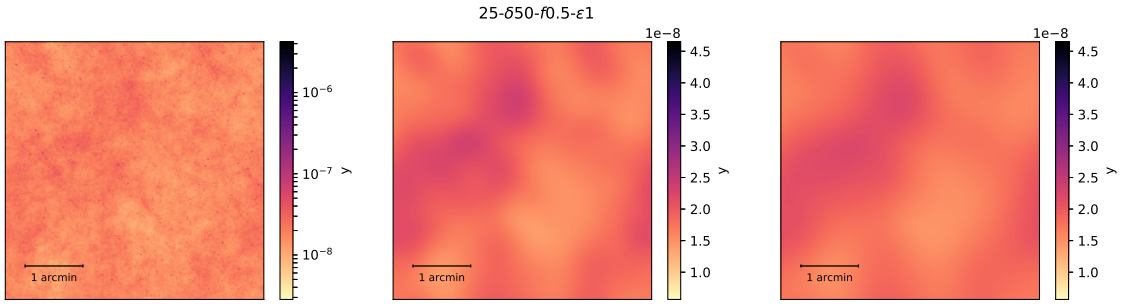

Figure 4.6: Full-resolution (left panel) and smoothed (middle and right panels) maps of the y-parameter for 25-δ50-f0.5-ϵ1. Smoothed maps are constructed for a Gaussian beam of FWHM 1.2 arcmin (middle) and 1.7 arcmin (right), corresponding to the resolution of the 150 GHz and 95 GHz channels of the SPT, respectively.

of the EoR).

For an instrument with an angular resolution of ~ 1 arcmin, like the SPT, the areas of highest electron pressure in the EoR produce a tSZ signal which is about three orders of magnitude smaller than that of clusters. However, a more precise instrument, with arcsec resolution and higher sensitivity, would be able to detect the small regions where $y \sim 10^{-6}$ in our full-resolution maps, and extend the power spectra to $l \sim 10^5$, where the EoR contribution becomes stronger. Although the EoR is a subdominant contributor to the total tSZ effect, when more sensitive instruments are developed, it will nevertheless be important to consider this component for precision cosmology.

4.2 Density Lightcones

We also investigate the effects of patchiness and temperature fluctuations in the IGM on the tSZ signal by integrating the gas density along the lines of sight for CoDa II, as described in Section 3.3.2. We assume a fixed global ionisation fraction for each light crossing through the box and constant global temperature throughout reionisation. In Figure 4.8, we show the distributions of the y-parameters obtained for these lightcones as well as the original electron pressure lightcone. The green line (p_e) is the histogram for the electron pressure, with all fluctuations in the fields present. The blue line (ρ_e) shows the results of integrating the electron density while keeping only the temperature constant at $T_\mathrm{e} = 30,000$ K. The orange line (ρ_{gas}) shows the integral of the gas density field with the temperature and ionisation fraction fluctuations removed. The black dashed line shows the value for y calculated analytically, in Section 3.3.3, for the same redshift range of

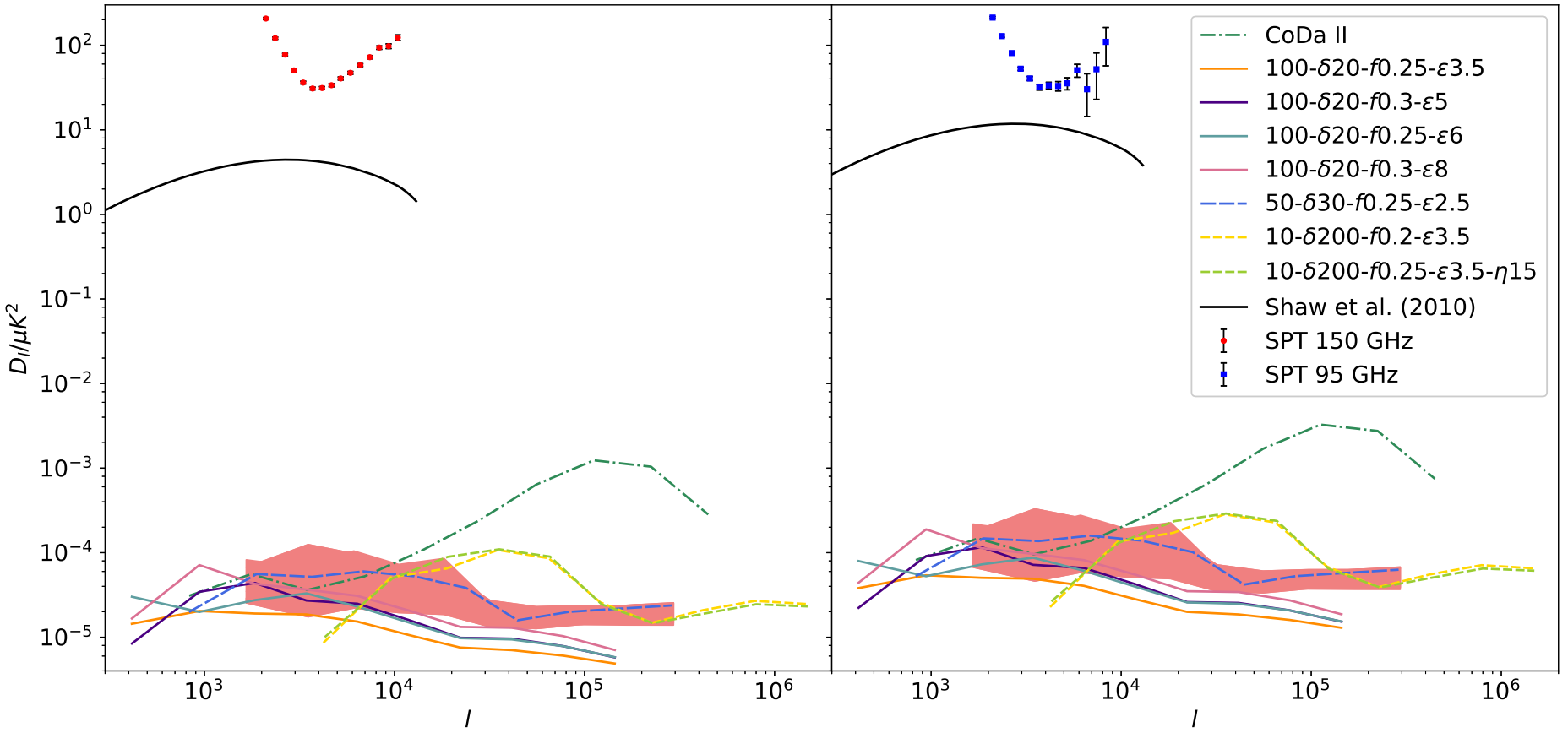

Figure 4.7: The angular temperature power spectra for the tSZ signals of the simulations. The power spectra are calculated for the two SPT bandpowers in which the tSZ effect is visible: 150 GHz (*left*) and 95 GHz (*right*). The coral bands include the power spectra for the eight 25 Mpc boxes. The black solid line is the template of the tSZ signal by Shaw et al. (2010), while the data points with error bars are the SPT data for the total CMB power spectrum at the respective frequencies (George et al., 2015).

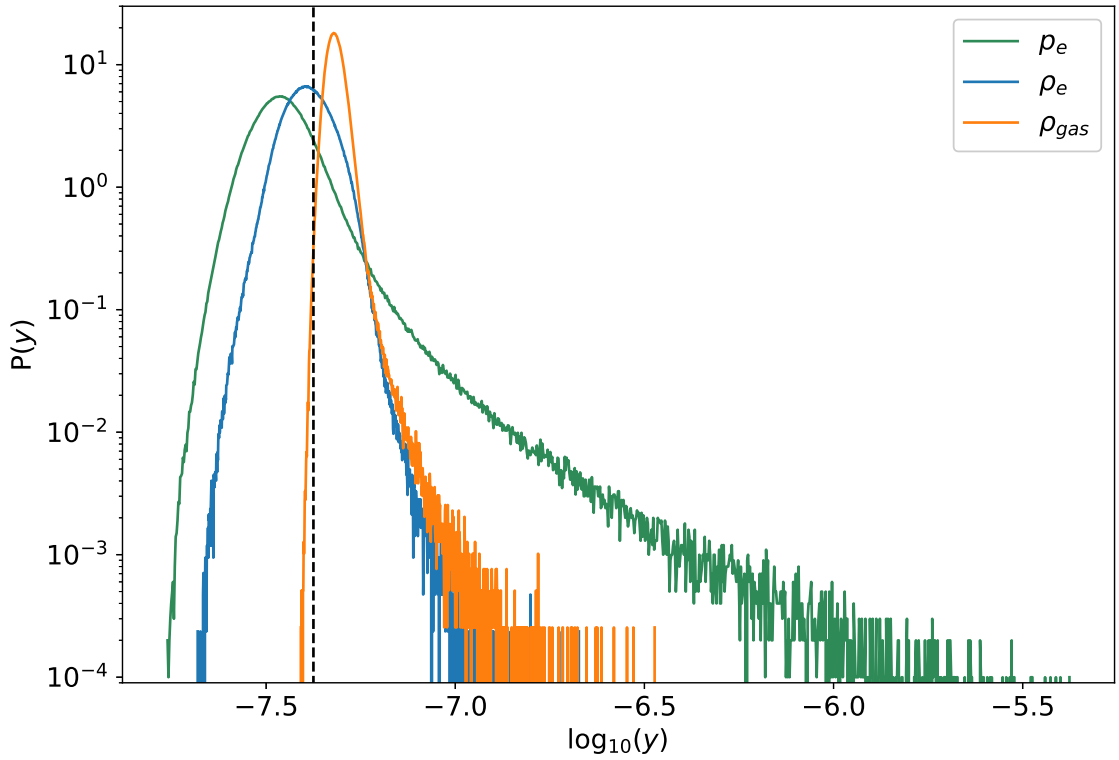

Figure 4.8: The distributions of the y-parameter for CoDa II where we have removed the fluctuations of the temperature and ionisation fraction fields. The green line shows the distribution for y with all fields present in the lightcone. The blue line shows the distribution when only the temperature is kept constant at $T_{\rm e} = 30,000$ K. The orange line is the distribution with $T_{\rm e} = 30,000$ K and a constant global ionisation fraction. The black dashed line shows the analytic result for all fields constant with instantaneous reionisation ($\log_{10} y = -7.38$, $y = 4.22 \times 10^{-8}$).

$z = 12$ to $z = 6$, with constant temperature, ionisation fraction and density, and assuming instantaneous reionisation ($y = 4.22 \times 10^{-8}$). The mean values of the distributions are $\langle y \rangle_{p_e} = \langle y \rangle_{\mathrm{CoDaII}} = 3.67 \times 10^{-8}$, $\langle y \rangle_{\rho_e} = 4.11 \times 10^{-8}$, and $\langle y \rangle_{\rho_{\mathrm{gas}}} = 4.84 \times 10^{-8}$.

The peak of each distribution lies near to the analytic result. However, the two lightcones in which reionisation is patchy (green and blue curves) have peaks just below our prediction. This is due to the presence of cool, neutral cells in these lightcones, compared to the scenarios where reionisation is homogeneous. Removing only the temperature fluctuations (blue line) has the effect of drastically reducing the positive tail and narrowing the distribution. This suggests that the skewing is a result of the contributions of the cells containing supernovae, which reach temperatures of millions of K, to the y-parameter values. We also lose some cells with lower temperatures as the left-hand side of the distribution shifts to the right. Removing both the temperature fluctuations and patchiness of the EoR (orange line) makes the distribution even thinner. Here we are left only with the fluctuations in the density field. Removing the patchiness has the effect of narrowing the distribution, shifting it towards the right and raising the mean y-parameter. In this scenario, the universe is homogeneously ionised. The narrowing of the distribution suggests that the areas with lower ionisation fractions (more neutral areas) are removed. Although removing the fluctuations in the temperature and ionisation fraction fields increases $\langle y \rangle$, we lose the small regions around supernovae where the y-parameter spikes.

4.3 Phase Diagrams

In this section, we present phase diagrams of the gas temperature and density for each simulation (see Figures 4.9 - 4.11). The distributions are taken for the boxes at the last redshift of their lightcones.

From the phase diagram for CoDa II (Figure 4.9a), we can see that there are regions of high temperature and density (yellow-green patch) which are mostly absent in the other boxes. These cells, with gas at higher pressure, are responsible for the small areas where $y > 10^{-7}$ in the CoDa II tSZ signal. Due to its higher resolution, CoDa II has a higher range of densities than all but the 10 Mpc boxes. While the 10 Mpc boxes do reach similar densities and temperatures, they lack cells that are both hot and "dense", and therefore the gas has lower pressures and lower y-parameters are obtained. But we also note that, as the redshifts at the end of their lightcones are earlier, and as the EoR in these simulations has not completed, the gas in these boxes have not yet equilibrated.

Additionally, the bi-modality in the temperature distributions of some of the boxes

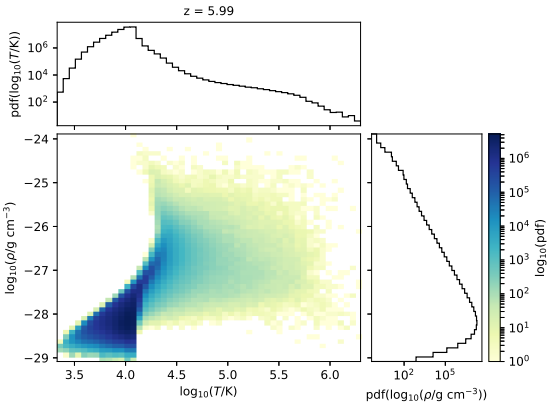

(a) CoDa II

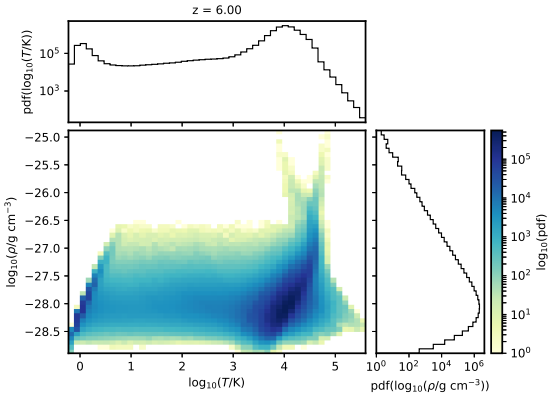

(b) 100-δ20-f0.25-ϵ3.5

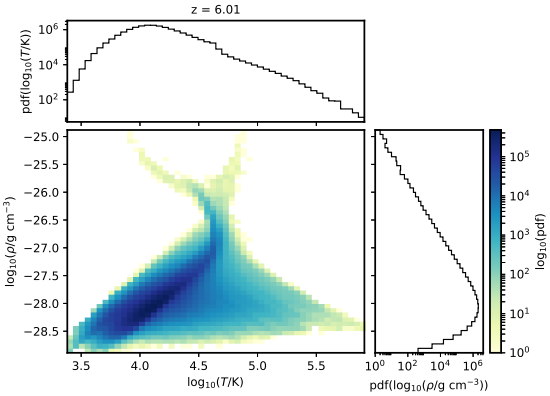

(c) 100-δ20-f0.3-ϵ5

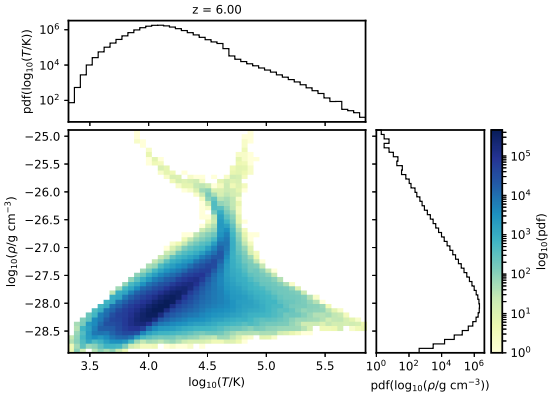

(d) 100-δ20-f0.25-ϵ6

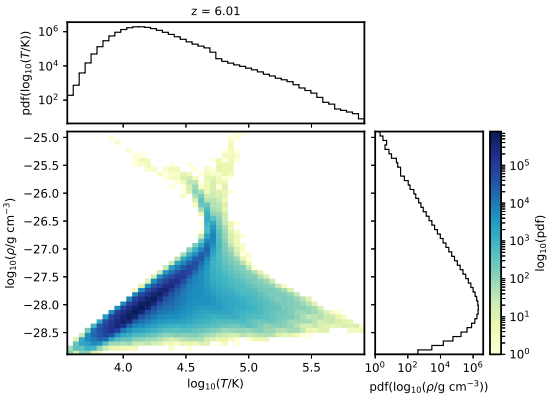

(e) 100-δ20-f0.3-ϵ8

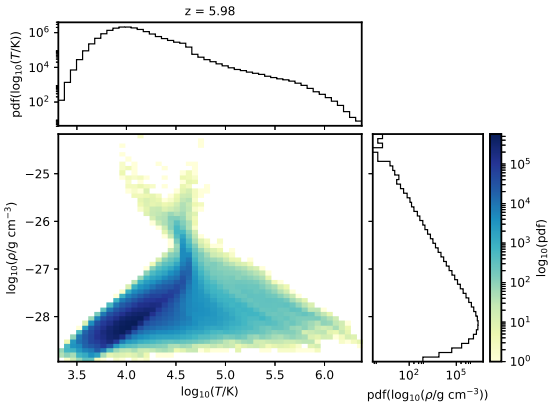

(f) 50-δ30-f0.25-ϵ2.5

Figure 4.9: Phase diagrams showing the gas density and temperature of the simulations, as labelled, at the end of the lightcones ($z \sim 6$).

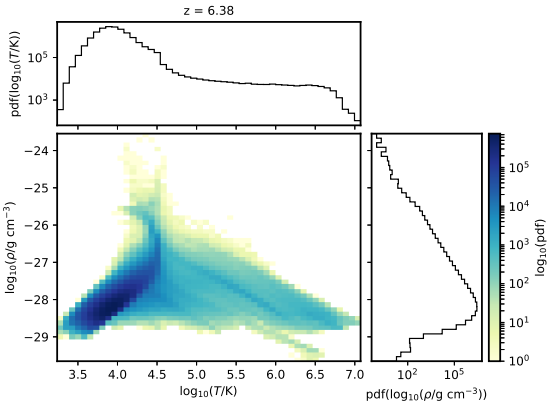

(a) 10-δ200-f0.2-ϵ3.5

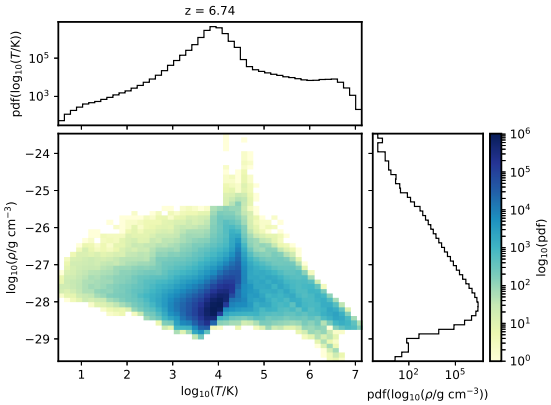

(b) 10-δ200-f0.25-ϵ3.5-η15

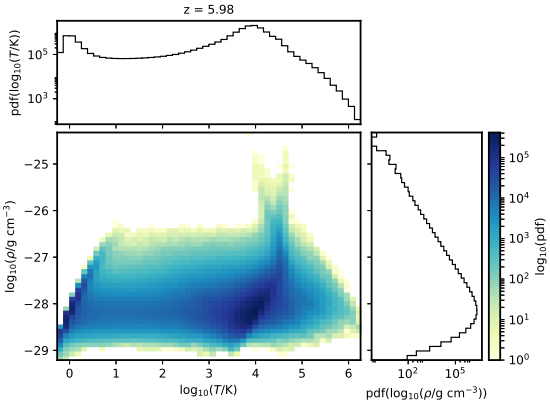

(c) 25-δ30-f0.1-ϵ4

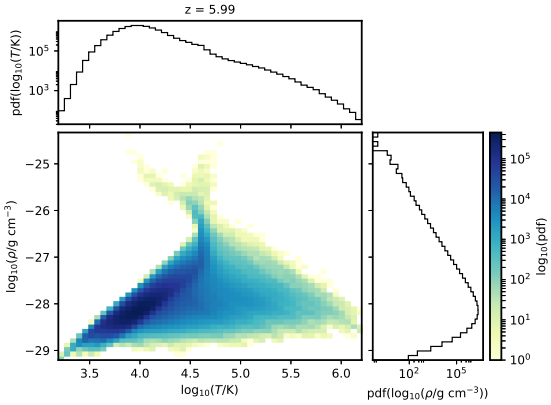

(d) 25-δ30-f0.14-ϵ4

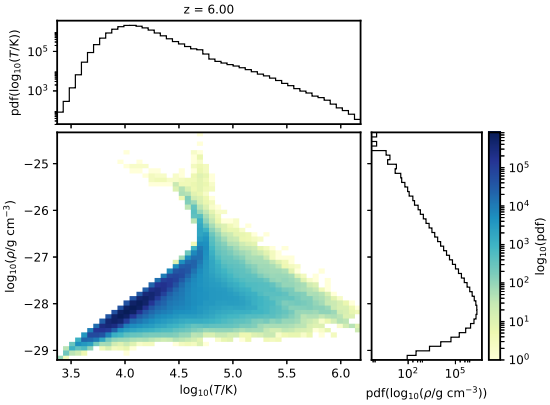

(e) 25-δ30-f0.2-ϵ4

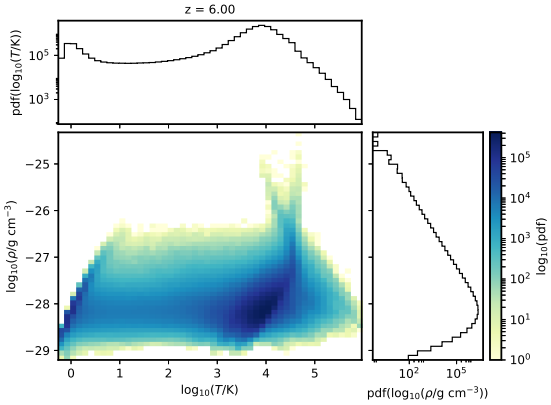

(f) 25-δ30-f0.2-ϵ2

Figure 4.10: Phase diagrams showing the gas density and temperature of the simulations, as labelled, at the end of the lightcones ($z \sim 6$).

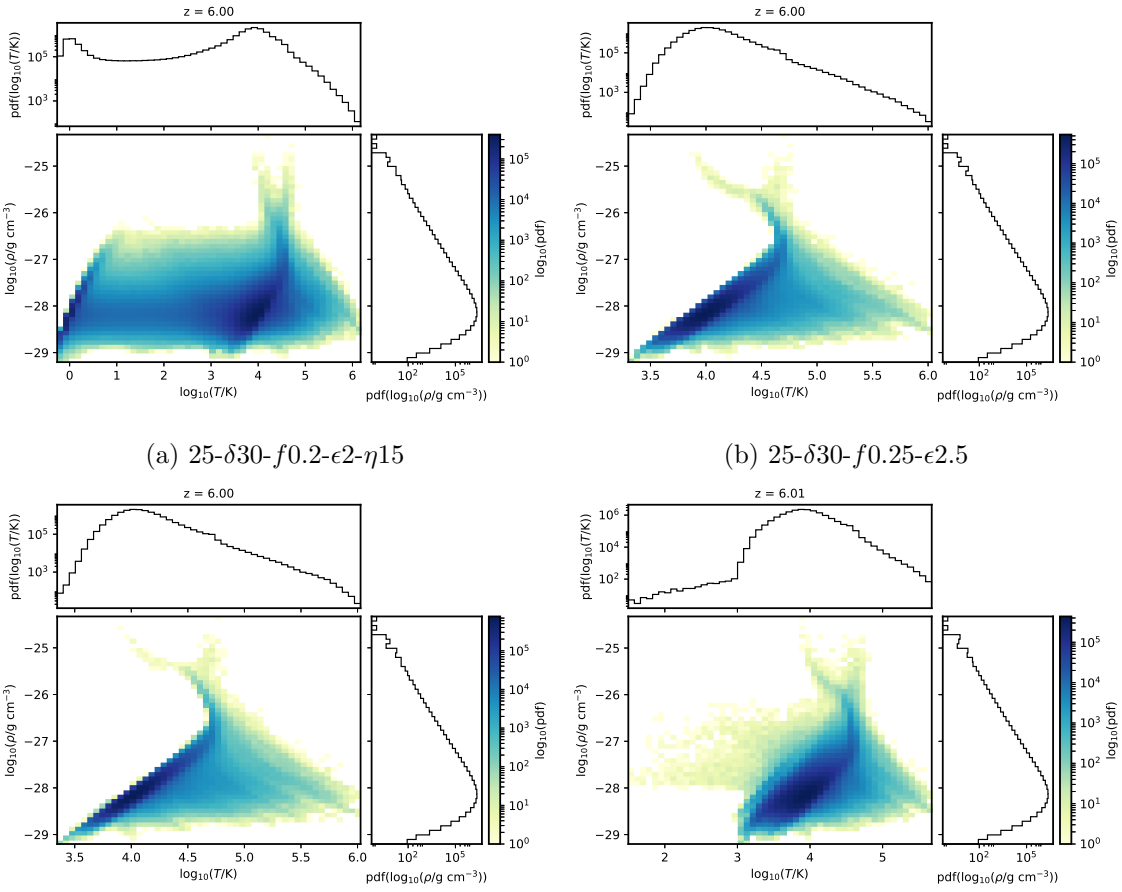

(a) 25-δ30-f0.2-ϵ2-η15

(b) 25-δ30-f0.25-ϵ2.5

(c) 25-δ50-f0.3-ϵ3

(d) 25-δ50-f0.5-ϵ1

Figure 4.11: Phase diagrams showing the gas density and temperature of the simulations, as labelled, at the end of the lightcones ($z \sim 6$).

(100-δ20-f0.25-ϵ3.5, 25-δ30-f0.1-ϵ4, 25-δ30-f0.2-ϵ2, and 25-δ30-f0.2-ϵ2-η15) reflects the ionisation states of the simulations. These four boxes have the latest EoR completion redshifts. At $z \sim 6$, reionisation has not yet finished for them, and so the gas has not reached a state of equilibrium, as there still exist areas of cold neutral gas. Conversely, we can see that the gas in the boxes in which reionisation is completed is more equilibrated; and, as the boxes are fully ionised, they contain no cold, neutral cells.

Thus, the phase diagrams reflect the stage of reionisation that the runs have reached. Consequently, we can directly see that the parameters which accelerate reionisation also lead to the gas becoming hotter and denser, and hence has higher pressure, at $z \sim 6$. This is best demonstrated in the series of 25 Mpc boxes (Figures 4.10c - 4.10f and 4.11a - 4.11d). For instance, those of 25-δ30-f0.2-ϵ4 and 25-δ50-f0.3-ϵ3, which both finish reionising at $z \sim 6.6$, are almost identical, with the exception that the hottest cells in the former are at higher temperatures than those in the latter. We also see that, amongst the boxes that have completed reionisation by $z = 6$, those that reionised earlier have gas which is more equilibrated, i.e. the density-temperature distributions are tighter (for e.g. 25-δ30-f0.25-ϵ2.5 versus 25-δ30-f0.14-ϵ4). These differences in the gas state ultimately lead to the variations in the y-parameters obtained.

Hence, phase space plots serve the purpose of checking that the condition of the gas in the simulation is as expected. Not only can we verify that it is indeed the state of the gas which is responsible for the tSZ signals we have calculated, but we can also determine whether there are one or more quantities that are responsible for the distributions of y-parameters obtained.

4.4 Electron Pressure Correction

In this section, we present the results for the y-parameter values which we originally computed before correcting the approximation for the electron pressure described in Section 3.3.4. Figure 4.12 shows the distributions in y-parameter values for the initial eight simulations. Using $p_{\rm e} = x_{\rm HII} p_{\rm gas}$ for the electron pressure, the results for the seven auxiliary simulations are all similar and seem to agree with each other. However, the distribution of y-parameter values for CoDa II appears as an outlier. Its mean value is $\langle y \rangle_{\rm CoDa\ II} = 1.48 \times 10^{-7}$ while the mean values of the other simulations are an order of magnitude lower ($\langle y \rangle \sim 10^{-8}$). Although the latter distributions initially agreed with each other, their results did not reflect their different reionisation histories.

One attempt to make sense of the difference between the results for CoDa II and the

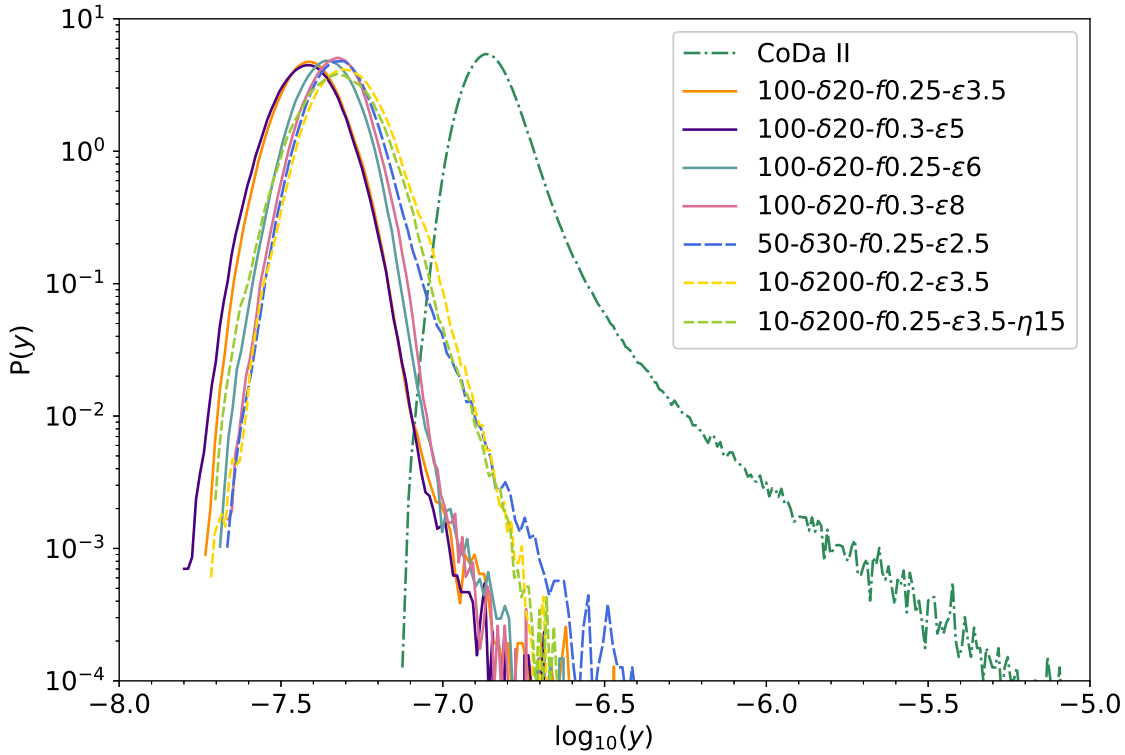

Figure 4.12: The distributions of the y-parameter values initially calculated using the approximation in Equation 3.22 for the electron pressure.

other boxes was to coarsen the high resolution y-parameter map for CoDa II (2048^2) to match the resolution of the others (1024^2) to investigate whether the discrepancy was a resolution effect. However, coarsening the map had negligible effect. As demonstrated in Figure 4.13, the distribution of the y-parameter was only slightly narrowed and did not shift. In Figure 4.14, we also show the full-resolution and coarsened maps. To the human eye, they are identical. These results show that the simulation resolution rather than the post-processing grid coarsening is responsible for the difference between the CoDa II values and the auxiliary simulations.

Finally, after it was pointed out that the files for the ionisation fractions for CoDa II were actually 1 + the ionisation fraction, we corrected for this while still using the initial approximation for the electron pressure. We present the PDFs for the y-parameter obtained for this correction (orange line) as well as the initial results (blue line) and the final, accurate results for CoDa II (green line) in Figure 4.15. While this correction shifted the distribution to the left, it was not sufficient to make the results agree with those of the other simulations. However, upon realising that the expression which we were using for the electron pressure was inaccurate, we reconstructed the lightcones for all the simulations and recalculated their y-parameters. This shifted the distribution for CoDa II even lower

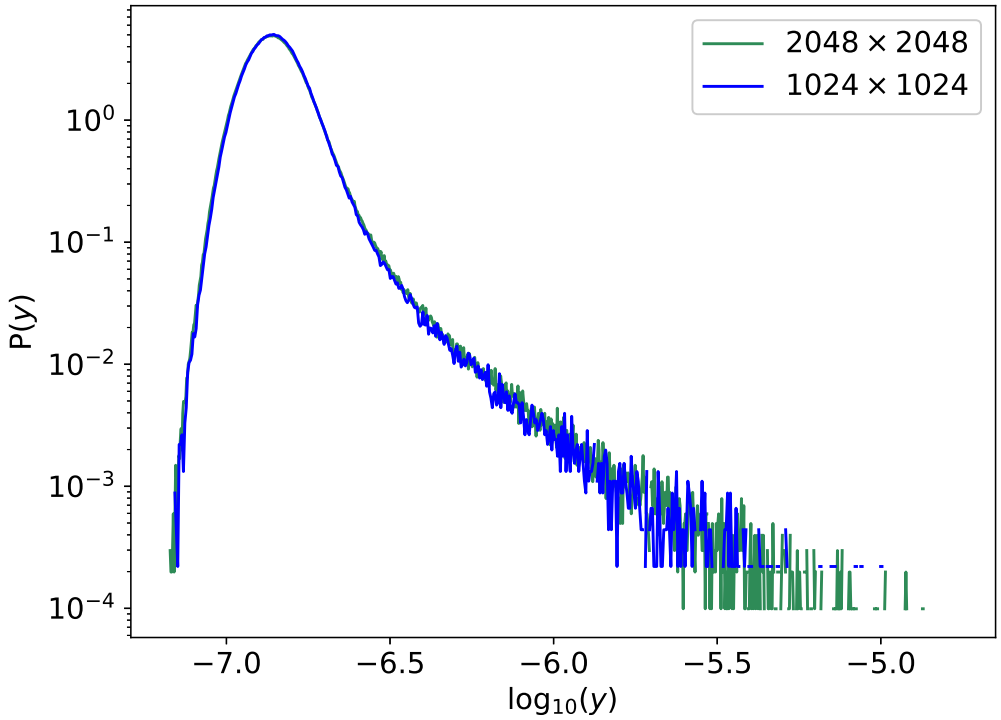

Figure 4.13: The y-parameter values for CoDa II using the initial approximation for electron pressure. The green line represents the distribution of y for the full-resolution map (the same as the curve plotted in Figure 4.12). The blue line represents the distribution of values after coarsening the map to a resolution of 1024^2 to match that of the auxiliary simulations.

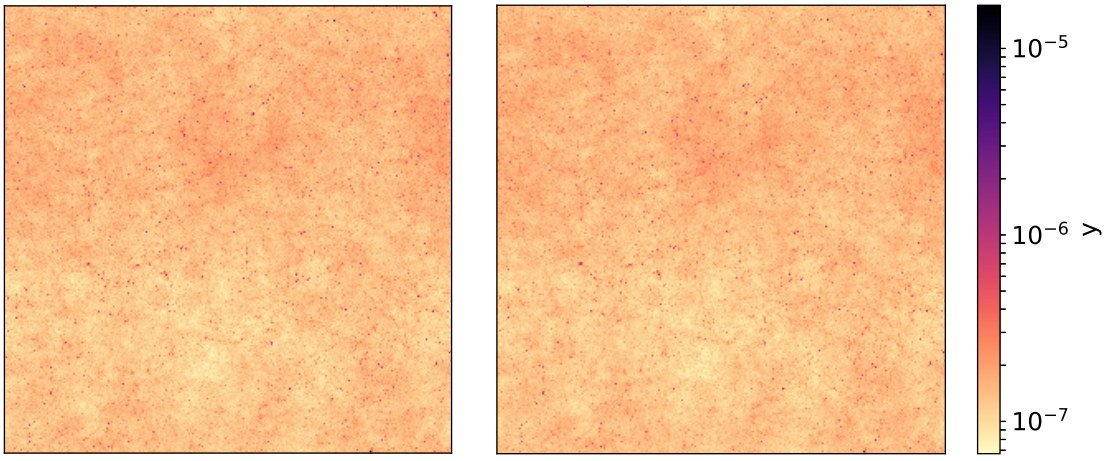

Figure 4.14: y-parameter maps of the initial CoDa II results for the full-resolution (2048^2) grid (*left*) and coarsened (1024^2) grid (*right*).

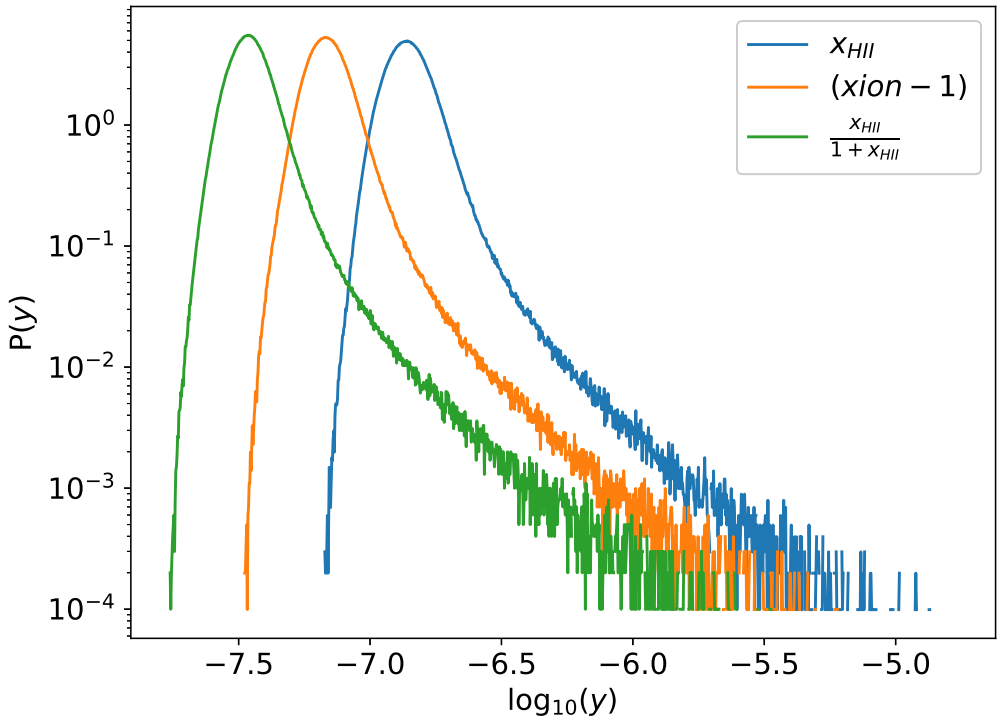

Figure 4.15: The distributions of the y-parameter computed for CoDa II using different expressions for the electron pressure. The blue line shows the results for the first approximation using $p_{\rm e} = x_{\rm HII} p_{\rm gas}$. The orange line shows the values obtained when correcting for the ionisation fraction files being $1 + x_{\rm HII}$ and using $p_{\rm e} = x_{\rm HII} p_{\rm gas}$. The green line is the results obtained when correcting for the ionisation fraction files and using the accurate expression for the electron pressure, $p_{\rm e} = \frac{x_{\rm HII}}{1+x_{\rm HII}} p_{\rm gas}$.

(more leftward), making all eight simulations align with each other (see Figure 4.1).

4.5 CoDa I

We show the PDFs of the y-parameter values calculated for CoDa I, CoDa II and the initial seven auxiliary simulations in Figure 4.16. We use the expression in Equation 3.22 for the electron pressure. We have chosen to compare these results for CoDa I with the initial results of the other eight simulations, and not the results obtained from using Equation 3.28, since this was the assumption we were making for the electron pressure at the point in our study when we decided to omit CoDa I. The lightcone for CoDa I also spans a longer redshift range ($z = 12.61$ - 4.23), so that all of the EoR was included, since its reionisation epoch ended late.

The mean of the y-parameter values for CoDa I is $\langle y \rangle_{\rm CoDa\ I} = 1.18 \times 10^{-7}$. Its distribution also has a positive tail similar to that of CoDa II. As with CoDa II, this is due to the

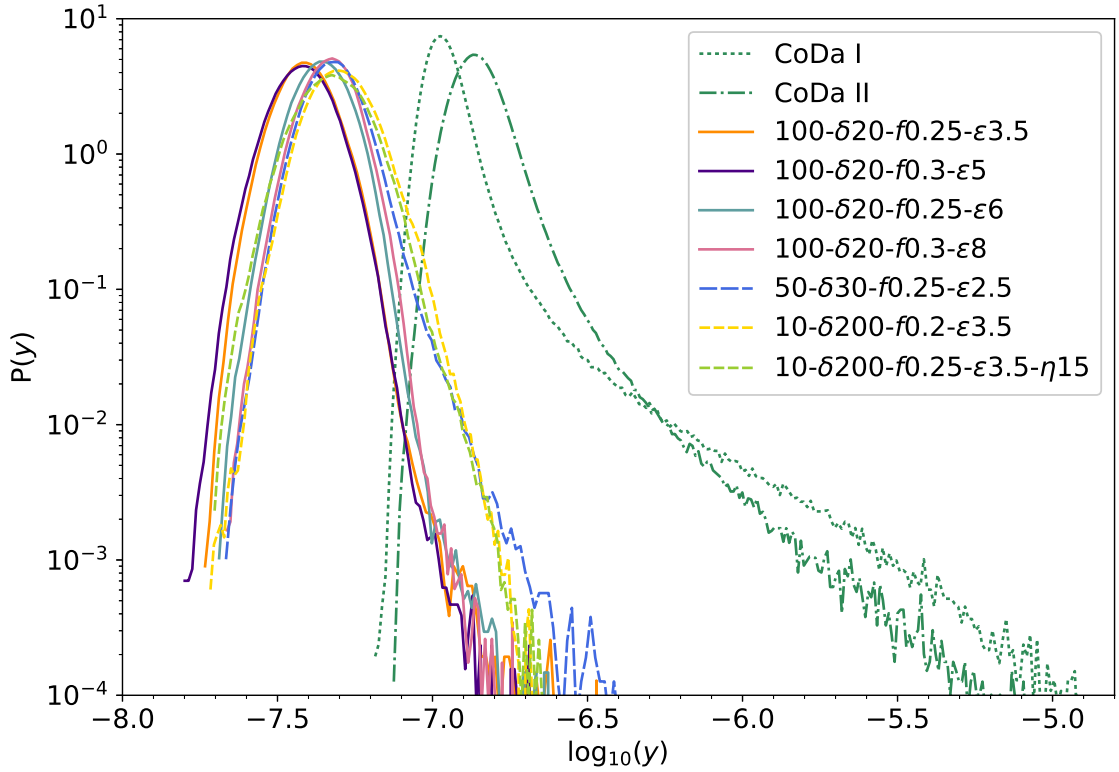

Figure 4.16: The distributions of the y-parameter values for CoDa I, CoDa II and the seven larger auxiliary simulations. All lightcones were constructed using the expression for electron pressure in Equation 3.22. The lightcone for CoDa I starts at $z = 12.61$ and ends at $z = 4.23$.

higher resolution of the box and there being more resolved cells with higher temperatures. However, the distribution is shifted to the right, compared with the auxiliary simulations. At first, we thought this was a result of the higher redshift range used. The fact that the PDF for CoDa II was also shifted suggested otherwise. Ultimately, we omitted CoDa I from the study due to its late EoR.

Chapter 5

Conclusions

The tSZ effect traces the thermal history of the universe. Although its signal is dominated by galaxy clusters at later redshifts, it receives a contribution from the dense ionised IGM during the EoR. Therefore, it is essential to investigate the extent of this effect at this stage in cosmic history, especially as its physics is easily understood. A proper, in-depth grasp of the EoR contribution will enable us to better model the global tSZ effect. As its power spectrum is sensitive to cosmology, advancements in our measurements and models will allow for tighter constraints to be placed on cosmological parameters (e.g. σ_8).

In this thesis, we utilised the hydrodynamic data from sixteen RAMSES-CUDATON simulations to compute the tSZ signal arising from the EoR. We constructed lightcones of the electron pressure between the redshift range $z = 6 - 12$ by interpolating between simulation snapshots, using the ionisation fraction and gas pressure fields. From these lightcones, we calculated the Compton y-parameter by numerically integrating along lines of sight in the direction of light propagation. We obtained maps of the y-parameter which we used to construct PDFs and angular power spectra. We also separated the y-parameter by redshifts in order to determine its redshift contributions. To probe the extent to which the temperature and density fluctuations, and patchiness of the EoR were responsible for the values obtained, we integrated density lightcones for CoDa II and made use of phase diagrams for all sixteen simulations.

All simulations yielded mean Compton y-parameter values in the order of $\langle y \rangle \sim 10^{-8}$, corresponding to the estimate made by Hill et al. (2015). The magnitude of the tSZ signal originating from the EoR shows some dependence on the timing of the end of this epoch. In general, simulations which finished reionising early had higher modal y-parameters than those whose EoR ended later. For example, when the EoR ended at $z \sim 6.6$, the modal y-parameter was $y \sim 3.0 \times 10^{-8}$, but when it ended at $z \sim 5.6$, the modal value was

$y \sim 2.0 \times 10^{-8}$. However, we also noticed that, while the magnitude of the tSZ effect is influenced by the timing of the EoR, it also affected by the SFR; where a higher SFR contributes to a stronger tSZ effect.

We also saw that the y-parameter maps and power spectra for the EoR signal distinctly differ from those of galaxy clusters. Maps smoothed for Gaussian beams of FWHM 1.2 arcmin and 1.7 arcmin had peak values of $y \sim 10^{-8}$, three orders of magnitude smaller than cluster values. At these scales, the EoR contribution to the angular power spectrum of the tSZ signal is $< 1\%$ that of clusters. However, for CoDa II, the power spectrum increases on smaller scales, suggesting a possibility that the EoR contribution might become more significant in this region. Nevertheless, without models that extend down to these angular scales, we are currently unable to confirm this. While the EoR contribution is sub-dominant to that of galaxy clusters, it is still essential to obtain an estimate of its signal as more sensitive technologies are developed in the future era of precision cosmology.

From the phase diagrams and the results of the density lightcones, we note that the high cell temperatures reached by CoDa II are responsible for its higher distribution of y-parameter values. The tail in its PDF is a result of the spatially resolved cells heated by supernova explosions. Removing the variations in the temperature and ionisation fraction fields raises the mean Compton parameter. This is because they widen the range of y-parameter values in the signal. The temperature fluctuations are responsible for the distributions being positively skewed, due to supernova explosions driving up the temperatures of small areas.

For the purpose of consistency, we attempted to use the same redshift range for the lightcones. However, in doing so, we did not capture the full extent of the EoR for some of our simulations. As we saw from separating the redshift contributions for CoDa II, the majority of the tSZ signal arises from the end of the EoR. Therefore, it will be beneficial to include all of the EoR for the eight simulations. Another limiting factor in this study is the shorter lightcones of the 10 Mpc boxes since we did not run these simulations to the end of the EoR. To remedy this, we should finish the runs for the 10 Mpc boxes, and either extend the redshift range of our lightcones to lower redshifts or set the lightcone range in accordance with specific ionisation fractions.

5.1 Future Work

To obtain a more complete tSZ signal, i.e. down to $z = 0$, we can incorporate cluster contributions by utilising halo models (see e.g. Cooray and Sheth, 2002) or cluster cata-

logues. We can also refine our estimations by including the effect of helium gas in the IGM as RAMSES-CUDATON assumes the gas is purely hydrogen. This can be done by interpolating the mean molecular weight of the gas throughout the EoR, since its value depends on the ionisation state of the gas, and updating the temperature field, and hence the pressure, to reflect this. We can also run additional simulations which include hydrogen and helium gas, e.g. RAMSES-RT, and calculate the tSZ signals they produce.

In addition, as we have simulation data for the gas velocity fields, we can calculate the y-parameter contribution from the bulk flow Doppler effect (see Hu et al., 1994). While the quadratic Doppler distortion from the EoR is predicted to be secondary to the tSZ effect, with a value of $y \sim 10^{-8}$, it seems that it may be comparable with the tSZ signal from EoR. As this second order contribution from the EoR has not been extensively investigated, it would be useful to produce a more updated estimate. We can also use the gas velocity data to calculate the kSZ effect during the EoR for our simulations. This would enable us to provide a more thorough study of the SZ effect during this cosmic epoch.

Bibliography

Abel, T., Bryan, G. L., and Norman, M. L. (2002). The Formation of the First Star in the Universe. *Science*, 295:93–98. 10

Aghanim, N., Majumdar, S., and Silk, J. (2008). Secondary anisotropies of the CMB. *Reports on Progress in Physics*, 71(6):066902. 4

Alvarez, M. A. (2016). The Kinetic Sunyaev-Zeldovich Effect from Reionization: Simulated Full-sky Maps at Arcminute Resolution. *ApJ*, 824:118. 21

Arnaud, M., Pointecouteau, E., and Pratt, G. W. (2005). The structural and scaling properties of nearby galaxy clusters. II. The M-T relation. *A&A*, 441:893–903. 24

Aubert, D. and Teyssier, R. (2008). A radiative transfer scheme for cosmological reionization based on a local Eddington tensor. *MNRAS*, 387:295–307. 31, 33, 34, 39

Bañados, E., Venemans, B. P., Mazzucchelli, C., Farina, E. P., Walter, F., Wang, F., Decarli, R., Stern, D., Fan, X., Davies, F. B., Hennawi, J. F., Simcoe, R. A., Turner, M. L., Rix, H.-W., Yang, J., Kelson, D. D., Rudie, G. C., and Winters, J. M. (2018). An 800-million-solar-mass black hole in a significantly neutral Universe at a redshift of 7.5. *Nature*, 553:473–476. 10

Balashev, S. A., Kholupenko, E. E., Chluba, J., Ivanchik, A. V., and Varshalovich, D. A. (2015). Spectral Distortions of the CMB Dipole. *ApJ*, 810:131. 4

Barbosa, D., Bartlett, J. G., Blanchard, A., and Oukbir, J. (1996). The Sunyaev-Zel'dovich effect and the value of {OMEGA}_0_. *A&A*, 314:13–17. 24

Barkana, R. and Loeb, A. (2001). In the beginning: the first sources of light and the reionization of the universe. *Phys. Rep.*, 349:125–238. 8, 58

Bastian, N., Covey, K. R., and Meyer, M. R. (2010). A universal stellar initial mass function? a critical look at variations. *Annual Review of Astronomy and Astrophysics*, 48(1):339–389. 11, 13

Battaglia, N., Bond, J. R., Pfrommer, C., Sievers, J. L., and Sijacki, D. (2010). Simulations of the Sunyaev-Zel'dovich Power Spectrum with Active Galactic Nucleus Feedback. *ApJ*, 725:91–99. 24

Battaglia, N., Natarajan, A., Trac, H., Cen, R., and Loeb, A. (2013a). Reionization on Large Scales. III. Predictions for Low-l Cosmic Microwave Background Polarization and High-l Kinetic Sunyaev-Zel'dovich Observables. *ApJ*, 776:83. 21

Battaglia, N., Trac, H., Cen, R., and Loeb, A. (2013b). Reionization on Large Scales. I. A Parametric Model Constructed from Radiation-hydrodynamic Simulations. *ApJ*, 776:81. 24

Becker, G. D. and Bolton, J. S. (2013). New measurements of the ionizing ultraviolet background over 2 ¡ z ¡ 5 and implications for hydrogen reionization. *Monthly Notices of the Royal Astronomical Society*, 436(2):1023–1039. xiii, 47

Bertschinger, E. (1998). Simulations of Structure Formation in the Universe. *ARA&A*, 36:599–654. 27

Bertschinger, E. (2001). Multiscale Gaussian Random Fields and Their Application to Cosmological Simulations. *ApJS*, 137:1–20. 37

Birkinshaw, M. (1999). The Sunyaev-Zel'dovich effect. *Phys. Rep.*, 310:97–195. 20

Bouwens, R. J., Illingworth, G. D., Oesch, P. A., Trenti, M., Labbé, I., Bradley, L., Carollo, M., van Dokkum, P. G., Gonzalez, V., Holwerda, B., and et al. (2015). Uv luminosity functions at redshifts z 4 to z 10: 10,000 galaxies from hst legacy fields. *The Astrophysical Journal*, 803(1):34. xiii, 49, 51

Bromm, V., Coppi, P. S., and Larson, R. B. (2002). The Formation of the First Stars. I. The Primordial Star-forming Cloud. *ApJ*, 564:23–51. 10

Bromm, V., Kudritzki, R. P., and Loeb, A. (2001). Generic spectrum and ionization efficiency of a heavy initial mass function for the first stars. *The Astrophysical Journal*, 552(2):464–472. 11, 13

Bromm, V. and Larson, R. B. (2004). The First Stars. *ARA&A*, 42:79–118. 8, 10

Bucher, M. (2015). Physics of the cosmic microwave background anisotropy. *International Journal of Modern Physics D*, 24:1530004–303. 4

Calabrese, E., Hložek, R., Battaglia, N., Bond, J. R., de Bernardis, F., Devlin, M. J., Hajian, A., Henderson, S., Hil, J. C., Kosowsky, A., Louis, T., McMahon, J., Moodley, K., Newburgh, L., Niemack, M. D., Page, L. A., Partridge, B., Sehgal, N., Sievers, J. L., Spergel, D. N., Staggs, S. T., Switzer, E. R., Trac, H., and Wollack, E. J. (2014). Precision epoch of reionization studies with next-generation CMB experiments. *J. Cosmology Astropart. Phys.*, 8:010. 21

Calverley, A. P., Becker, G. D., Haehnelt, M. G., and Bolton, J. S. (2011). Measurements of the ultraviolet background at 4.6 ¡ z ¡ 6.4 using the quasar proximity effect star. *MNRAS*, 412(4):2543–2562. xiii, 47

Carlstrom, J. E., Ade, P. A. R., Aird, K. A., Benson, B. A., Bleem, L. E., Busetti, S., Chang, C. L., Chauvin, E., Cho, H.-M., Crawford, T. M., Crites, A. T., Dobbs, M. A., Halverson, N. W., Heimsath, S., Holzapfel, W. L., Hrubes, J. D., Joy, M., Keisler, R., Lanting, T. M., Lee, A. T., Leitch, E. M., Leong, J., Lu, W., Lueker, M., Luong-Van, D., McMahon, J. J., Mehl, J., Meyer, S. S., Mohr, J. J., Montroy, T. E., Padin, S., Plagge, T., Pryke, C., Ruhl, J. E., Schaffer, K. K., Schwan, D., Shirokoff, E., Spieler, H. G., Staniszewski, Z., Stark, A. A., Tucker, C., Vanderlinde, K., Vieira, J. D., and Williamson, R. (2011). The 10 Meter South Pole Telescope. *PASP*, 123:568. 54

Carlstrom, J. E., Holder, G. P., and Reese, E. D. (2002). Cosmology with the Sunyaev-Zel'dovich Effect. *ARA&A*, 40:643–680. xii, 20, 21, 23

Chabrier, G. (2003). Galactic stellar and substellar initial mass function. *Publications of the Astronomical Society of the Pacific*, 115(809):763–795. xi, 12

Challinor, A. (2013). CMB anisotropy science: a review. In Burton, M. G., Cui, X., and Tothill, N. F. H., editors, *Astrophysics from Antarctica*, volume 288 of *IAU Symposium*, pages 42–52. 4

Challinor, A. and Lasenby, A. (1998). Relativistic Corrections to the Sunyaev-Zeldovich Effect. *ApJ*, 499:1–6. 22

Chary, R.-R. (2008). The stellar initial mass function at the epoch of reionization. *The Astrophysical Journal*, 680(1):32–40. xii, 13, 14

Chen, X. and Kamionkowski, M. (2004). Particle decays during the cosmic dark ages. *Phys. Rev. D*, 70(4):043502. 10

Chluba, J., Switzer, E., Nelson, K., and Nagai, D. (2013). Sunyaev-zeldovich signal processing and temperature-velocity moment method for individual clusters. *MNRAS*, 430(4):3054–3069. 22

Choudhury, T. R. and Ferrara, A. (2006). Physics of Cosmic Reionization. *arXiv Astrophysics e-prints*. 8

Ciardi, B. and Ferrara, A. (2005). The First Cosmic Structures and Their Effects. *Space Sci. Rev.*, 116:625–705. 8, 10

Ciardi, B., Inoue, S., Abdalla, F. B., Asad, K., Bernardi, G., Bolton, J. S., Brentjens, M., de Bruyn, A. G., Chapman, E., Daiboo, S., Fernandez, E. R., Ghosh, A., Graziani, L., Harker, G. J. A., Iliev, I. T., Jelic, V., Jensen, H., Kazemi, S., Koopmans, L. V. E., Martinez, O., Maselli, A., Mellema, G., Offringa, A. R., Pandey, V. N., Schaye, J., Thomas, R., Vedantham, H., Yatawatta, S., and Zaroubi, S. (2015). Simulating the 21 cm forest detectable with lofar and ska in the spectra of high-z grbs. *MNRAS*, 453(1):101–105. 17

Cooray, A. and Sheth, R. (2002). Halo models of large scale structure. *Phys. Rep.*, 372:1–129. 86

Crawford, T. M., Schaffer, K. K., Bhattacharya, S., Aird, K. A., Benson, B. A., Bleem, L. E., Carlstrom, J. E., Chang, C. L., Cho, H.-M., Crites, A. T., de Haan, T., Dobbs, M. A., Dudley, J., George, E. M., Halverson, N. W., Holder, G. P., Holzapfel, W. L., Hoover, S., Hou, Z., Hrubes, J. D., Keisler, R., Knox, L., Lee, A. T., Leitch, E. M., Lueker, M., Luong-Van, D., McMahon, J. J., Mehl, J., Meyer, S. S., Millea, M., Mocanu, L. M., Mohr, J. J., Montroy, T. E., Padin, S., Plagge, T., Pryke, C., Reichardt, C. L., Ruhl, J. E., Sayre, J. T., Shaw, L., Shirokoff, E., Spieler, H. G., Staniszewski, Z., Stark, A. A., Story, K. T., van Engelen, A., Vanderlinde, K., Vieira, J. D., Williamson, R., and Zahn, O. (2014). A Measurement of the Secondary-CMB and Millimeter-wave-foreground Bispectrum using 800 deg^2 of South Pole Telescope Data. *ApJ*, 784:143. 24

da Silva, A. C., Barbosa, D., Liddle, A. R., and Thomas, P. A. (2001). Hydrodynamical simulations of the Sunyaev-Zel'dovich effect: the kinetic effect. *MNRAS*, 326:155–163. 24

D'Aloisio, A., McQuinn, M., Maupin, O., Davies, F. B., Trac, H., Fuller, S., and Upton

Sanderbeck, P. R. (2019). Heating of the Intergalactic Medium by Hydrogen Reionization. *ApJ*, 874:154. xiii, 47

Davé, R. (2008). The galaxy stellar mass-star formation rate relation: evidence for an evolving stellar initial mass function? *Monthly Notices of the Royal Astronomical Society*, 385(1):147–160. 11

Davies, F. B., Hennawi, J. F., Bañados, E., Lukić, Z., Decarli, R., Fan, X., Farina, E. P., Mazzucchelli, C., Rix, H.-W., Venemans, B. P., and et al. (2018). Quantitative constraints on the reionization history from the igm damping wing signature in two quasars at z ¿ 7. *The Astrophysical Journal*, 864(2):142. xii, 45, 46

de Marchi, G. and Paresce, F. (2001). The Mass Function of Galactic Clusters and its Evolution with Time. In *Astronomische Gesellschaft Meeting Abstracts*, volume 18 of *Astronomische Gesellschaft Meeting Abstracts*, page MS 05 51. xi, 12

De Zotti, G., Negrello, M., Castex, G., Lapi, A., and Bonato, M. (2016). Another look at distortions of the Cosmic Microwave Background spectrum. *J. Cosmology Astropart. Phys.*, 3:047. 6

Dubois, Y. and Teyssier, R. (2008). On the onset of galactic winds in quiescent star forming galaxies. *A&A*, 477:79–94. 36

Elmegreen, B. G. (2009). The Stellar Initial Mass Function in 2007: A Year for Discovering Variations. In Sheth, K., Noriega-Crespo, A., Ingalls, J. G., and Paladini, R., editors, *The Evolving ISM in the Milky Way and Nearby Galaxies*, volume 14, page 14. 13

Fan, X., Strauss, M. A., Becker, R. H., White, R. L., Gunn, J. E., Knapp, G. R., Richards, G. T., Schneider, D. P., Brinkmann, J., and Fukugita, M. (2006). Constraining the Evolution of the Ionizing Background and the Epoch of Reionization with z˜6 Quasars. II. A Sample of 19 Quasars. *AJ*, 132:117–136. xii, 15, 45, 50

FaucherGiguère, C., Lidz, A., Hernquist, L., and Zaldarriaga, M. (2008). Evolution of the intergalactic opacity: Implications for the ionizing background, cosmic star formation, and quasar activity. *The Astrophysical Journal*, 688(1):85–107. xiii, 47

Field, G. B. (1958). Excitation of the Hydrogen 21-CM Line. *Proceedings of the IRE*, 46:240–250. 17

Fixsen, D. J., Cheng, E. S., Gales, J. M., Mather, J. C., Shafer, R. A., and Wright, E. L. (1996). The Cosmic Microwave Background Spectrum from the Full COBE FIRAS Data Set. *ApJ*, 473:576. 24, 63

Furlanetto, S. R., Oh, S. P., and Briggs, F. H. (2006). Cosmology at low frequencies: The 21 cm transition and the high-redshift Universe. *Phys. Rep.*, 433:181–301. 8, 17

Gehlot, B. K., Mertens, F. G., Koopmans, L. V. E., Brentjens, M. A., Zaroubi, S., Ciardi, B., Ghosh, A., Hatef, M., Iliev, I. T., Jelic, V., Kooistra, R., Krause, F., Mellema, G., Mevius, M., Mitra, M., Offringa, A. R., Pandey, V. N., Sardarabadi, A. M., Schaye, J., Silva, M. B., Vedantham, H. K., and Yatawatta, S. (2019). The first power spectrum limit on the 21-cm signal of neutral hydrogen during the cosmic dawn at z=20-25 from lofar. *MNRAS*, 488(3):4271–4287. 17

George, E. M., Reichardt, C. L., Aird, K. A., Benson, B. A., Bleem, L. E., Carlstrom, J. E., Chang, C. L., Cho, H.-M., Crawford, T. M., Crites, A. T., de Haan, T., Dobbs, M. A., Dudley, J., Halverson, N. W., Harrington, N. L., Holder, G. P., Holzapfel, W. L., Hou, Z., Hrubes, J. D., Keisler, R., Knox, L., Lee, A. T., Leitch, E. M., Lueker, M., Luong-Van, D., McMahon, J. J., Mehl, J., Meyer, S. S., Millea, M., Mocanu, L. M., Mohr, J. J., Montroy, T. E., Padin, S., Plagge, T., Pryke, C., Ruhl, J. E., Schaffer, K. K., Shaw, L., Shirokoff, E., Spieler, H. G., Staniszewski, Z., Stark, A. A., Story, K. T., van Engelen, A., Vanderlinde, K., Vieira, J. D., Williamson, R., and Zahn, O. (2015). A Measurement of Secondary Cosmic Microwave Background Anisotropies from the 2500 Square-degree SPT-SZ Survey. *ApJ*, 799:177. xiv, 24, 55, 68, 73

Giallongo, E., Cristiani, S., D'Odorico, S., and Fontana, A. (2002). A Low Upper Limit to the Lyman Continuum Emission of Two Galaxies at z˜=3. *ApJ*, 568:L9–L12. 10

Giallongo, E., Grazian, A., Fiore, F., Fontana, A., Pentericci, L., Vanzella, E., Dickinson, M., Kocevski, D., Castellano, M., Cristiani, S., Ferguson, H., Finkelstein, S., Grogin, N., Hathi, N., Koekemoer, A. M., Newman, J. A., and Salvato, M. (2015). Faint AGNs at z 4 in the CANDELS GOODS-S field: looking for contributors to the reionization of the Universe. *A&A*, 578:A83. 10

Gingold, R. A. and Monaghan, J. J. (1977). Smoothed particle hydrodynamics: theory and application to non-spherical stars. *MNRAS*, 181(2):375–389. 28

Glover, S. (2005). The formation of the first stars in the universe. *Space Science Reviews*, 117(3-4):445–508. 10

Gottloeber, S., Hoffman, Y., and Yepes, G. (2010). Constrained Local UniversE Simulations (CLUES). *arXiv e-prints*. 40

Greig, B., Mesinger, A., Haiman, Z., and Simcoe, R. A. (2017). Are we witnessing the epoch of reionisation at z = 7.1 from the spectrum of j1120+0641? *Monthly Notices of the Royal Astronomical Society*, page stw3351. xii, 45, 46

Gruzinov, A. and Hu, W. (1998). Secondary Cosmic Microwave Background Anisotropies in a Universe Reionized in Patches. *ApJ*, 508:435–439. 20

Gunn, J. E. and Peterson, B. A. (1965). On the Density of Neutral Hydrogen in Intergalactic Space. *ApJ*, 142:1633–1636. 15

Guth, A. H. (1981). Inflationary universe: A possible solution to the horizon and flatness problems. *Phys. Rev. D*, 23:347–356. 7

Hahn, O. and Abel, T. (2013). MUSIC: MUlti-Scale Initial Conditions. Astrophysics Source Code Library. 37

Hill, J. C., Battaglia, N., Chluba, J., Ferraro, S., Schaan, E., and Spergel, D. N. (2015). Taking the Universe's Temperature with Spectral Distortions of the Cosmic Microwave Background. *Phys. Rev. Lett.*, 115(26):261301. 24, 63, 85

Hill, J. C., Sherwin, B. D., Smith, K. M., Addison, G. E., Battaglia, N., Battistelli, E. S., Bond, J. R., Calabrese, E., Devlin, M. J., Dunkley, J., Dunner, R., Essinger-Hileman, T., Gralla, M. B., Hajian, A., Hasselfield, M., Hincks, A. D., Hlozek, R., Hughes, J. P., Kosowsky, A., Louis, T., Marsden, D., Moodley, K., Niemack, M. D., Page, L. A., Partridge, B., Schmitt, B., Sehgal, N., Sievers, J. L., Spergel, D. N., Staggs, S. T., Swetz, D. S., Thornton, R., Trac, H., and Wollack, E. J. (2014). The Atacama Cosmology Telescope: A Measurement of the Thermal Sunyaev-Zel'dovich One-Point PDF. *arXiv e-prints*. 24

Hinshaw, G., Weiland, J. L., Hill, R. S., Odegard, N., Larson, D., Bennett, C. L., Dunkley, J., Gold, B., Greason, M. R., Jarosik, N., Komatsu, E., Nolta, M. R., Page, L., Spergel, D. N., Wollack, E., Halpern, M., Kogut, A., Limon, M., Meyer, S. S., Tucker, G. S., and Wright, E. L. (2009). Five-Year Wilkinson Microwave Anisotropy Probe Observations: Data Processing, Sky Maps, and Basic Results. *ApJS*, 180:225–245. 61

Hoag, A., Bradač, M., Huang, K., Mason, C., Treu, T., Schmidt, K. B., Trenti, M., Strait,

V., Lemaux, B. C., Finney, E. Q., and et al. (2019). Constraining the neutral fraction of hydrogen in the igm at redshift 7.5. *The Astrophysical Journal*, 878(1):12. xii, 45, 46

Hogg, D. W. (1999). Distance measures in cosmology. *arXiv Astrophysics e-prints*. 53

Holder, G. P., Haiman, Z., Kaplinghat, M., and Knox, L. (2003). The Reionization History at High Redshifts. II. Estimating the Optical Depth to Thomson Scattering from Cosmic Microwave Background Polarization. *ApJ*, 595:13–18. 18

Hopkins, A. M. (2018). The dawes review 8: Measuring the stellar initial mass function. *Publications of the Astronomical Society of Australia*, 35. 13

Horowitz, B. and Seljak, U. (2017). Cosmological constraints from thermal sunyaev-zeldovich power spectrum revisited. *MNRAS*, 469(1):394–400. 24

Hu, W., Scott, D., and Silk, J. (1994). Reionization and cosmic microwave background distortions: A complete treatment of second-order Compton scattering. *Phys. Rev. D*, 49:648–670. 25, 87

Hu, W., Sugiyama, N., and Silk, J. (1997). The physics of microwave background anisotropies. *Nature*, 386:37–43. 4

Hubble, E. and Humason, M. L. (1931). The Velocity-Distance Relation among Extra-Galactic Nebulae. *ApJ*, 74:43. 1

Hui, L. and Gnedin, N. Y. (1997). Equation of state of the photoionized intergalactic medium. *MNRAS*, 292(1):27–42. 33

Iliev, I. T., Ciardi, B., Alvarez, M. A., Maselli, A., Ferrara, A., Gnedin, N. Y., Mellema, G., Nakamoto, T., Norman, M. L., Razoumov, A. O., Rijkhorst, E.-J., Ritzerveld, J., Shapiro, P. R., Susa, H., Umemura, M., and Whalen, D. J. (2006a). Cosmological radiative transfer codes comparison project - I. The static density field tests. *MNRAS*, 371:1057–1086. 29

Iliev, I. T., Mellema, G., Ahn, K., Shapiro, P. R., Mao, Y., and Pen, U.-L. (2014). Simulating cosmic reionization: how large a volume is large enough? *MNRAS*, 439(1):725–743. 9

Iliev, I. T., Mellema, G., Pen, U.-L., Bond, J. R., and Shapiro, P. R. (2008). Current models of the observable consequences of cosmic reionization and their detectability. *MNRAS*, 384:863–874. 21, 39

Iliev, I. T., Mellema, G., Pen, U.-L., Merz, H., Shapiro, P. R., and Alvarez, M. A. (2006b). Simulating cosmic reionization at large scales - I. The geometry of reionization. *MNRAS*, 369:1625–1638. 9

Iliev, I. T., Pen, U.-L., Bond, J. R., Mellema, G., and Shapiro, P. R. (2007). The Kinetic Sunyaev-Zel'dovich Effect from Radiative Transfer Simulations of Patchy Reionization. *ApJ*, 660:933–944. 21, 39

Iliev, I. T., Scannapieco, E., and Shapiro, P. R. (2005). The impact of small-scale structure on cosmological ionization fronts and reionization. *Astrophys. J.*, 624(2):491–504. 50

Iliev, I. T., Whalen, D., Mellema, G., Ahn, K., Baek, S., Gnedin, N. Y., Kravtsov, A. V., Norman, M., Raicevic, M., Reynolds, D. R., Sato, D., Shapiro, P. R., Semelin, B., Smidt, J., Susa, H., Theuns, T., and Umemura, M. (2009). Cosmological radiative transfer comparison project - II. The radiation-hydrodynamic tests. *MNRAS*, 400:1283–1316. 29

Inoue, A. K., Iwata, I., Deharveng, J.-M., Buat, V., and Burgarella, D. (2005). VLT narrow-band photometry in the Lyman continuum of two galaxies at z
3. Limits to the escape of ionizing flux. *A&A*, 435:471–482. 10

Iwata, I., Inoue, A. K., Matsuda, Y., Furusawa, H., Hayashino, T., Kousai, K., Akiyama, M., Yamada, T., Burgarella, D., and Deharveng, J.-M. (2009). Detections of Lyman Continuum from Star-Forming Galaxies at z ˜ 3 through Subaru/Suprime-Cam Narrow-Band Imaging. *ApJ*, 692:1287–1293. 10

Kasuya, S. and Kawasaki, M. (2004). Early reionization by decaying particles and cosmic microwave background radiation. *Phys. Rev. D*, 70(10):103519. 10

Kim, J., Park, C., Gott, III, J. R., and Dubinski, J. (2009). The Horizon Run N-Body Simulation: Baryon Acoustic Oscillations and Topology of Large-scale Structure of the Universe. *ApJ*, 701:1547–1559. 28

Kitayama, T. (2014). Cosmological and astrophysical implications of the Sunyaev-Zel'dovich effect. *Progress of Theoretical and Experimental Physics*, 2014(6):06B111. 20

Knox, L., Scoccimarro, R., and Dodelson, S. (1998). Impact of Inhomogeneous Reionization on Cosmic Microwave Background Anisotropy. *Phys. Rev. Lett.*, 81:2004–2007. 20

Komatsu, E. and Seljak, U. (2002). The Sunyaev-Zel'dovich angular power spectrum as a probe of cosmological parameters. *MNRAS*, 336:1256–1270. 23, 24

Koopmans, L., Pritchard, J., Mellema, G., Aguirre, J., Ahn, K., Barkana, R., van Bemmel, I., Bernardi, G., Bonaldi, A., Briggs, F., de Bruyn, A. G., Chang, T. C., Chapman, E., Chen, X., Ciardi, B., Dayal, P., Ferrara, A., Fialkov, A., Fiore, F., Ichiki, K., Illiev, I. T., Inoue, S., Jelic, V., Jones, M., Lazio, J., Maio, U., Majumdar, S., Mack, K. J., Mesinger, A., Morales, M. F., Parsons, A., Pen, U. L., Santos, M., Schneider, R., Semelin, B., de Souza, R. S., Subrahmanyan, R., Takeuchi, T., Vedantham, H., Wagg, J., Webster, R., Wyithe, S., Datta, K. K., and Trott, C. (2015). The Cosmic Dawn and Epoch of Reionisation with SKA. *Advancing Astrophysics with the Square Kilometre Array (AASKA14)*, page 1. 17

Kroupa, P. (2001). On the variation of the initial mass function. *Monthly Notices of the Royal Astronomical Society*, 322(2):231–246. xi, 12

Kroupa, P., Tout, C. A., and Gilmore, G. (1993). The distribution of low-mass stars in the galactic disc. *Monthly Notices of the Royal Astronomical Society*, 262(3):545–587. 11

Kroupa, P., Weidner, C., Pflamm-Altenburg, J., Thies, I., Dabringhausen, J., Marks, M., and Maschberger, T. (2013). The stellar and sub-stellar initial mass function of simple and composite populations. In *Planets, Stars and Stellar Systems*, pages 115–242. Springer Netherlands. 13

Krumholz, M. R. (2014). The big problems in star formation: The star formation rate, stellar clustering, and the initial mass function. *Physics Reports*, 539(2):49–134. 13

Levermore, C. D. (1984). Relating Eddington factors to flux limiters. *J. Quant. Spectrosc. Radiative Transfer*, 31:149–160. 33

Lewis, A., Weller, J., and Battye, R. (2006). The cosmic microwave background and the ionization history of the universe. *MNRAS*, 373(2):561–570. 18

Lidz, A. (2016). Physics of the Intergalactic Medium During the Epoch of Reionization. In Mesinger, A., editor, *Understanding the Epoch of Cosmic Reionization: Challenges and Progress*, volume 423 of *Astrophysics and Space Science Library*, page 23. 27

Liu, H., Slatyer, T. R., and Zavala, J. (2016). Contributions to cosmic reionization from dark matter annihilation and decay. *Phys. Rev. D*, 94(6):063507. 10

Loeb, A. and Barkana, R. (2001). The Reionization of the Universe by the First Stars and Quasars. *ARA&A*, 39:19–66. 8

Lucy, L. B. (1977). A numerical approach to the testing of the fission hypothesis. *AJ*, 82:1013–1024. 28

Ma, Q., Helgason, K., Komatsu, E., Ciardi, B., and Ferrara, A. (2018). Measuring patchy reionization with ksz(2)-21 cm correlations. *MNRAS*, 476(3):4025–4031. 21

Mapelli, M. and Ferrara, A. (2005). Background radiation from sterile neutrino decay and reionization. *MNRAS*, 364(1):2–12. 10

Mapelli, M., Ferrara, A., and Pierpaoli, E. (2006). Impact of dark matter decays and annihilations on reionization. *MNRAS*, 369(4):1719–1724. 10

Martel, H. and Shapiro, P. R. (1998). A convenient set of comoving cosmological variables and their application. *MNRAS*, 297(2):467–485. 35

Maselli, A., Ferrara, A., and Ciardi, B. (2003). Crash: a radiative transfer scheme. *MNRAS*, 345(2):379–394. 33

Mason, C. A., Treu, T., Dijkstra, M., Mesinger, A., Trenti, M., Pentericci, L., de Barros, S., and Vanzella, E. (2018). The universe is reionizing atz 7: Bayesian inference of the igm neutral fraction using lyemission from galaxies. *The Astrophysical Journal*, 856(1):2. xii, 45, 46

McQuinn, M., Furlanetto, S. R., Hernquist, L., Zahn, O., and Zaldarriaga, M. (2005). The Kinetic Sunyaev-Zel'dovich Effect from Reionization. *ApJ*, 630:643–656. 21

McQuinn, M., Lidz, A., Zahn, O., Dutta, S., Hernquist, L., and Zaldarriaga, M. (2007). The morphology of hii regions during reionization. *MNRAS*, 377(3):1043–1063. 9

Meiksin, A. (2005). Constraints on the ionization sources of the high-redshift intergalactic medium. *MNRAS*, 356(2):596–606. 10

Meiksin, A. and Madau, P. (1993). On the photoionization of the intergalactic medium by quasars at high redshift. *ApJ*, 412:34–55. 10

Mellema, G., Iliev, I. T., Pen, U.-L., and Shapiro, P. R. (2006). Simulating cosmic reionization at large scales - II. The 21-cm emission features and statistical signals. *MNRAS*, 372:679–692. 17

Mellema, G., Koopmans, L. V. E., Abdalla, F. A., Bernardi, G., Ciardi, B., Daiboo, S., de Bruyn, A. G., Datta, K. K., Falcke, H., Ferrara, A., Iliev, I. T., Iocco, F., Jelić, V., Jensen, H., Joseph, R., Labroupoulos, P., Meiksin, A., Mesinger, A., Offringa, A. R., Pandey, V. N., Pritchard, J. R., Santos, M. G., Schwarz, D. J., Semelin, B., Vedantham, H., Yatawatta, S., and Zaroubi, S. (2013). Reionization and the Cosmic Dawn with the Square Kilometre Array. *Experimental Astronomy*, 36:235–318. 17

Mesinger, A., McQuinn, M., and Spergel, D. N. (2012). The kinetic Sunyaev-Zel'dovich signal from inhomogeneous reionization: a parameter space study. *MNRAS*, 422:1403–1417. 21, 39

Mihalas, D. and Mihalas, B. W. (1984). *Foundations of radiation hydrodynamics*. 31

Miller, G. E. and Scalo, J. M. (1979). The initial mass function and stellar birthrate in the solar neighborhood. *The Astrophysical Journal Supplement Series*, 41:513. 11

Morales, M. F. and Wyithe, J. S. B. (2010). Reionization and Cosmology with 21-cm Fluctuations. *ARA&A*, 48:127–171. 9, 16

Mortonson, M. J. and Hu, W. (2008). Model-Independent Constraints on Reionization from Large-Scale Cosmic Microwave Background Polarization. *ApJ*, 672:737–751. 18

Mroczkowski, T., Nagai, D., Basu, K., Chluba, J., Sayers, J., Adam, R., Churazov, E., Crites, A., Di Mascolo, L., Eckert, D., Macias-Perez, J., Mayet, F., Perotto, L., Pointecouteau, E., Romero, C., Ruppin, F., Scannapieco, E., and ZuHone, J. (2019). Astrophysics with the Spatially and Spectrally Resolved Sunyaev-Zeldovich Effects. A Millimetre/Submillimetre Probe of the Warm and Hot Universe. *Space Sci. Rev.*, 215:17. 20

Natarajan, A. and Schwarz, D. J. (2010). Distinguishing standard reionization from dark matter models. *Phys. Rev. D*, 81(12):123510. 10

Norman, M. L. (2008). Population III star formation and IMF. American Institute of Physics. 13

Nozawa, S., Itoh, N., Suda, Y., and Ohhata, Y. (2006). An improved formula for the relativistic corrections to the kinematical Sunyaev-Zeldovich effect for clusters of galaxies. *Nuovo Cimento B Serie*, 121:487–500. 22

Ocvirk, P., Aubert, D., Sorce, J. G., Shapiro, P. R., Deparis, N., Dawoodbhoy, T., Lewis, J., Teyssier, R., Yepes, G., Gottlöber, S., Ahn, K., Iliev, I. T., and Hoffman,

Y. (2018). Cosmic Dawn II (CoDa II): a new radiation-hydrodynamics simulation of the self-consistent coupling of galaxy formation and reionization. *arXiv e-prints*. 39, 40

Ocvirk, P., Gillet, N., Shapiro, P. R., Aubert, D., Iliev, I. T., Teyssier, R., Yepes, G., Choi, J.-H., Sullivan, D., Knebe, A., Gottlöber, S., D'Aloisio, A., Park, H., Hoffman, Y., and Stranex, T. (2016). Cosmic Dawn (CoDa): the First Radiation-Hydrodynamics Simulation of Reionization and Galaxy Formation in the Local Universe. *MNRAS*, 463(2):1462. 61

Offner, S. S. R., Clark, P. C., Hennebelle, P., Bastian, N., Bate, M. R., Hopkins, P. F., Moreaux, E., and Whitworth, A. P. (2014). The origin and universality of the stellar initial mass function. In *Protostars and Planets VI*. University of Arizona Press. xi, 11, 12, 13

Oldengott, I. M., Boriero, D., and Schwarz, D. J. (2016). Reionization and dark matter decay. *J. Cosmology Astropart. Phys.*, 8:054. 10

Olum, K. D. and Vilenkin, A. (2006). Reionization from cosmic string loops. *Phys. Rev. D*, 74(6):063516. 10

Ouchi, M., Shimasaku, K., Furusawa, H., Saito, T., Yoshida, M., Akiyama, M., Ono, Y., Yamada, T., Ota, K., Kashikawa, N., Iye, M., Kodama, T., Okamura, S., Simpson, C., and Yoshida, M. (2010). Statistics of 207 Lyα Emitters at a Redshift Near 7: Constraints on Reionization and Galaxy Formation Models. *ApJ*, 723:869–894. xii, 45

Padmanabhan, N. and Finkbeiner, D. P. (2005). Detecting dark matter annihilation with CMB polarization: Signatures and experimental prospects. *Phys. Rev. D*, 72(2):023508. 10

Park, H., Komatsu, E., Shapiro, P. R., Koda, J., and Mao, Y. (2016). The Impact of Nonlinear Structure Formation on the Power Spectrum of Transverse Momentum Fluctuations and the Kinetic Sunyaev-Zel'dovich Effect. *ApJ*, 818:37. 21

Park, H., Shapiro, P. R., Komatsu, E., Iliev, I. T., Ahn, K., and Mellema, G. (2013). The Kinetic Sunyaev-Zel'dovich Effect as a Probe of the Physics of Cosmic Reionization: The Effect of Self-regulated Reionization. *ApJ*, 769:93. 21, 39

Patil, A. H., Yatawatta, S., Koopmans, L. V. E., de Bruyn, A. G., Brentjens, M. A., Zaroubi, S., Asad, K. M. B., Hatef, M., Jelić, V., Mevius, M., Offringa, A. R., Pandey, V. N., Vedantham, H., Abdalla, F. B., Brouw, W. N., Chapman, E., Ciardi, B., Gehlot,

B. K., Ghosh, A., Harker, G., Iliev, I. T., Kakiichi, K., Majumdar, S., Mellema, G., Silva, M. B., Schaye, J., Vrbanec, D., and Wijnholds, S. J. (2017). Upper Limits on the 21 cm Epoch of Reionization Power Spectrum from One Night with LOFAR. *ApJ*, 838:65. 17

Pen, U.-L. (1997). Generating Cosmological Gaussian Random Fields. *ApJ*, 490:L127–L130. 37

Penzias, A. A. and Wilson, R. W. (1965). A Measurement of Excess Antenna Temperature at 4080 Mc/s. *ApJ*, 142:419–421. 2

Planck Collaboration, Ade, P. A. R., Aghanim, N., Armitage-Caplan, C., Arnaud, M., Ashdown, M., Atrio-Barandela, F., Aumont, J., Baccigalupi, C., Banday, A. J., and et al. (2014). Planck 2013 results. XVI. Cosmological parameters. *A&A*, 571:A16. 40, 61

Planck Collaboration, Aghanim, N., Akrami, Y., Ashdown, M., Aumont, J., Baccigalupi, C., Ballardini, M., Banday, A. J., Barreiro, R. B., Bartolo, N., Basak, S., Battye, R., Benabed, K., Bernard, J.-P., Bersanelli, M., Bielewicz, P., Bock, J. J., Bond, J. R., Borrill, J., Bouchet, F. R., Boulanger, F., Bucher, M., Burigana, C., Butler, R. C., Calabrese, E., Cardoso, J.-F., Carron, J., Challinor, A., Chiang, H. C., Chluba, J., Colombo, L. P. L., Combet, C., Contreras, D., Crill, B. P., Cuttaia, F., de Bernardis, P., de Zotti, G., Delabrouille, J., Delouis, J.-M., Di Valentino, E., Diego, J. M., Doré, O., Douspis, M., Ducout, A., Dupac, X., Dusini, S., Efstathiou, G., Elsner, F., Enßlin, T. A., Eriksen, H. K., Fantaye, Y., Farhang, M., Fergusson, J., Fernandez-Cobos, R., Finelli, F., Forastieri, F., Frailis, M., Franceschi, E., Frolov, A., Galeotta, S., Galli, S., Ganga, K., Génova-Santos, R. T., Gerbino, M., Ghosh, T., González-Nuevo, J., Górski, K. M., Gratton, S., Gruppuso, A., Gudmundsson, J. E., Hamann, J., Handley, W., Herranz, D., Hivon, E., Huang, Z., Jaffe, A. H., Jones, W. C., Karakci, A., Keihänen, E., Keskitalo, R., Kiiveri, K., Kim, J., Kisner, T. S., Knox, L., Krachmalnicoff, N., Kunz, M., Kurki-Suonio, H., Lagache, G., Lamarre, J.-M., Lasenby, A., Lattanzi, M., Lawrence, C. R., Le Jeune, M., Lemos, P., Lesgourgues, J., Levrier, F., Lewis, A., Liguori, M., Lilje, P. B., Lilley, M., Lindholm, V., López-Caniego, M., Lubin, P. M., Ma, Y.-Z., Macías-Pérez, J. F., Maggio, G., Maino, D., Mandolesi, N., Mangilli, A., Marcos-Caballero, A., Maris, M., Martin, P. G., Martinelli, M., Martínez-González, E., Matarrese, S., Mauri, N., McEwen, J. D., Meinhold, P. R., Melchiorri, A., Mennella, A., Migliaccio, M., Millea, M., Mitra, S., Miville-Deschênes, M.-A., Molinari, D., Montier,

L., Morgante, G., Moss, A., Natoli, P., Nørgaard-Nielsen, H. U., Pagano, L., Paoletti, D., Partridge, B., Patanchon, G., Peiris, H. V., Perrotta, F., Pettorino, V., Piacentini, F., Polastri, L., Polenta, G., Puget, J.-L., Rachen, J. P., Reinecke, M., Remazeilles, M., Renzi, A., Rocha, G., Rosset, C., Roudier, G., Rubiño-Martín, J. A., Ruiz-Granados, B., Salvati, L., Sandri, M., Savelainen, M., Scott, D., Shellard, E. P. S., Sirignano, C., Sirri, G., Spencer, L. D., Sunyaev, R., Suur-Uski, A.-S., Tauber, J. A., Tavagnacco, D., Tenti, M., Toffolatti, L., Tomasi, M., Trombetti, T., Valenziano, L., Valiviita, J., Van Tent, B., Vibert, L., Vielva, P., Villa, F., Vittorio, N., Wandelt, B. D., Wehus, I. K., White, M., White, S. D. M., Zacchei, A., and Zonca, A. (2018a). Planck 2018 results. VI. Cosmological parameters. *arXiv e-prints*. x, xi, xiii, 1, 5, 6, 18, 40, 48, 50

Planck Collaboration, Aghanim, N., Arnaud, M., Ashdown, M., Aumont, J., Baccigalupi, C., Banday, A. J., Barreiro, R. B., Bartlett, J. G., Bartolo, N., and et al. (2015). Planck 2015 results. XXII. A map of the thermal Sunyaev-Zeldovich effect. *ArXiv e-prints*. 24

Planck Collaboration, Akrami, Y., Arroja, F., Ashdown, M., Aumont, J., Baccigalupi, C., Ballardini, M., Banday, A. J., Barreiro, R. B., Bartolo, N., Basak, S., Battye, R., Benabed, K., Bernard, J.-P., Bersanelli, M., Bielewicz, P., Bock, J. J., Bond, J. R., Borrill, J., Bouchet, F. R., Boulanger, F., Bucher, M., Burigana, C., Butler, R. C., Calabrese, E., Cardoso, J.-F., Carron, J., Casaponsa, B., Challinor, A., Chiang, H. C., Colombo, L. P. L., Combet, C., Contreras, D., Crill, B. P., Cuttaia, F., de Bernardis, P., de Zotti, G., Delabrouille, J., Delouis, J.-M., Désert, F.-X., Di Valentino, E., Dickinson, C., Diego, J. M., Donzelli, S., Doré, O., Douspis, M., Ducout, A., Dupac, X., Efstathiou, G., Elsner, F., Enßlin, T. A., Eriksen, H. K., Falgarone, E., Fantaye, Y., Fergusson, J., Fernandez-Cobos, R., Finelli, F., Forastieri, F., Frailis, M., Franceschi, E., Frolov, A., Galeotta, S., Galli, S., Ganga, K., Génova-Santos, R. T., Gerbino, M., Ghosh, T., González-Nuevo, J., Górski, K. M., Gratton, S., Gruppuso, A., Gudmundsson, J. E., Hamann, J., Handley, W., Hansen, F. K., Helou, G., Herranz, D., Hivon, E., Huang, Z., Jaffe, A. H., Jones, W. C., Karakci, A., Keihänen, E., Keskitalo, R., Kiiveri, K., Kim, J., Kisner, T. S., Knox, L., Krachmalnicoff, N., Kunz, M., Kurki-Suonio, H., Lagache, G., Lamarre, J.-M., Langer, M., Lasenby, A., Lattanzi, M., Lawrence, C. R., Le Jeune, M., Leahy, J. P., Lesgourgues, J., Levrier, F., Lewis, A., Liguori, M., Lilje, P. B., Lilley, M., Lindholm, V., López-Caniego, M., Lubin, P. M., Ma, Y.-Z., Macías-Pérez, J. F., Maggio, G., Maino, D., Mandolesi, N., Mangilli, A., Marcos-Caballero, A., Maris, M., Martin, P. G., Martínez-González, E., Matarrese, S., Mauri, N., McEwen, J. D., Meerburg, P. D., Meinhold, P. R., Melchiorri, A., Mennella, A., Migliaccio, M.,

Millea, M., Mitra, S., Miville-Deschênes, M.-A., Molinari, D., Moneti, A., Montier, L., Morgante, G., Moss, A., Mottet, S., Münchmeyer, M., Natoli, P., Nørgaard-Nielsen, H. U., Oxborrow, C. A., Pagano, L., Paoletti, D., Partridge, B., Patanchon, G., Pearson, T. J., Peel, M., Peiris, H. V., Perrotta, F., Pettorino, V., Piacentini, F., Polastri, L., Polenta, G., Puget, J.-L., Rachen, J. P., Reinecke, M., Remazeilles, M., Renzi, A., Rocha, G., Rosset, C., Roudier, G., Rubiño-Martín, J. A., Ruiz-Granados, B., Salvati, L., Sandri, M., Savelainen, M., Scott, D., Shellard, E. P. S., Shiraishi, M., Sirignano, C., Sirri, G., Spencer, L. D., Sunyaev, R., Suur-Uski, A.-S., Tauber, J. A., Tavagnacco, D., Tenti, M., Terenzi, L., Toffolatti, L., Tomasi, M., Trombetti, T., Valiviita, J., Van Tent, B., Vibert, L., Vielva, P., Villa, F., Vittorio, N., Wandelt, B. D., Wehus, I. K., White, M., White, S. D. M., Zacchei, A., and Zonca, A. (2018b). Planck 2018 results. I. Overview and the cosmological legacy of Planck. *arXiv e-prints*. xi, 3

Pogosian, L. and Vilenkin, A. (2004). Early reionization by cosmic strings reexamined. *Phys. Rev. D*, 70(6):063523. 10

Press, W. H. and Schechter, P. (1974). Formation of Galaxies and Clusters of Galaxies by Self-Similar Gravitational Condensation. *ApJ*, 187:425–438. 24

Pritchard, J. R. and Loeb, A. (2012). 21 cm cosmology in the 21st century. *Reports on Progress in Physics*, 75(8):086901. 17

Prunet, S., Pichon, C., Aubert, D., Pogosyan, D., Teyssier, R., and Gottloeber, S. (2008). Initial Conditions For Large Cosmological Simulations. *ApJS*, 178:179–188. 37

Puchwein, E., Bolton, J. S., Haehnelt, M. G., Madau, P., Becker, G. D., and Haardt, F. (2015). The photoheating of the intergalactic medium in synthesis models of the uv background. *MNRAS*, 450(4):4081–4097. 10

Rasera, Y. and Teyssier, R. (2006). The history of the baryon budget. Cosmic logistics in a hierarchical universe. *A&A*, 445:1–27. 36

Rauch, M. (1998). The Lyman Alpha Forest in the Spectra of QSOs. *ARA&A*, 36:267–316. 16

Refregier, A., Komatsu, E., Spergel, D. N., and Pen, U.-L. (2000). Power spectrum of the Sunyaev-Zel'dovich effect. *Phys. Rev. D*, 61(12):123001. 24, 63

Rephaeli, Y. (1995). Comptonization Of The Cosmic Microwave Background: The Sunyaev-Zeldovich Effect. *ARA&A*, 33:541–580. 20

Ripamonti, E., Mapelli, M., and Ferrara, A. (2007). The impact of dark matter decays and annihilations on the formation of the first structures. *MNRAS*, 375(4):1399–1408. 10

Rosdahl, J. and Blaizot, J. (2012). Extended lya emission from cold accretion streams. *MNRAS*, 423(1):344–366. 34

Rosdahl, J., Blaizot, J., Aubert, D., Stranex, T., and Teyssier, R. (2013). ramses-rt: radiation hydrodynamics in the cosmological context. *MNRAS*, 436(3):2188–2231. 31, 32, 34

Ross, H. E., Dixon, K. L., Ghara, R., Iliev, I. T., and Mellema, G. (2019). Evaluating the qso contribution to the 21-cm signal from the cosmic dawn. *MNRAS*, 487(1):1101–1119. 17

Ross, H. E., Dixon, K. L., Iliev, I. T., and Mellema, G. (2017). Simulating the impact of x-ray heating during the cosmic dawn. *MNRAS*, 468(4):3785–3797. 17

Rybicki, G. B. and Lightman, A. P. (1979). *Radiative processes in astrophysics*. 21

Sachs, R. K. and Wolfe, A. M. (1967). Perturbations of a Cosmological Model and Angular Variations of the Microwave Background. *ApJ*, 147:73. 19

Salpeter, E. E. (1955). The luminosity function and stellar evolution. *The Astrophysical Journal*, 121:161. xi, 11, 12

Salvador-Solé, E., Manrique, A., Guzman, R., Espinosa, J. M. R., Gallego, J., Herrero, A., Mas-Hesse, J. M., and Franch, A. M. (2016). Constraining the Epoch of Reionization from the Observed Properties of the High-z Universe. *The Astrophysical Journal*, 834(1):49. 13

Santos, M. G., Cooray, A., Haiman, Z., Knox, L., and Ma, C.-P. (2003). Small-Scale Cosmic Microwave Background Temperature and Polarization Anisotropies Due to Patchy Reionization. *ApJ*, 598:756–766. 20

Sazonov, S. Y. and Sunyaev, R. A. (2000). The Profile of a Narrow Line after Single Scattering by Maxwellian Electrons: Relativistic Corrections to the Kernel of the Integral Kinetic Equation. *ApJ*, 543:28–55. 21

Scalo, J. M. (1986). The Stellar Initial Mass Function. *Fundamentals Cosmic Phys.*, 11:1–278. 11

Schaerer, D. (2002). On the properties of massive population III stars and metal-free stellar populations. *Astronomy & Astrophysics*, 382(1):28–42. 10, 11, 13

Scheuer, P. A. G. (1965). A Sensitive Test for the Presence of Atomic Hydrogen in Intergalactic Space. *Nature*, 207:963. 15

Sehgal, N., Bode, P., Das, S., Hernandez-Monteagudo, C., Huffenberger, K., Lin, Y.-T., Ostriker, J. P., and Trac, H. (2010). Simulations of the Microwave Sky. *ApJ*, 709:920–936. 24

Seljak, U., Burwell, J., and Pen, U.-L. (2001). Sunyaev-Zeldovich effect from hydrodynamical simulations: Maps and low order statistics. *Phys. Rev. D*, 63(6):063001. 24

Semelin, B. (2016). Detailed modelling of the 21-cm forest. *MNRAS*, 455(1):962–973. 17

Semelin, B., Combes, F., and Baek, S. (2007). Lyman-alpha radiative transfer during the epoch of reionization: contribution to 21-cm signal fluctuations. *A&A*, 474:365–374. 17

Shapley, A. E., Steidel, C. C., Pettini, M., Adelberger, K. L., and Erb, D. K. (2006). The Direct Detection of Lyman Continuum Emission from Star-forming Galaxies at z˜3. *ApJ*, 651:688–703. 10

Shaw, L. D., Nagai, D., Bhattacharya, S., and Lau, E. T. (2010). Impact of Cluster Physics on the Sunyaev-Zel'dovich Power Spectrum. *ApJ*, 725:1452–1465. xiv, 23, 24, 55, 68, 73

Shklovskii, I. S. (1965). Physical Conditions in the Gaseous Envelope of 3c-273. *Soviet Ast.*, 8:638. 15

Sievers, J. L., Hlozek, R. A., Nolta, M. R., Acquaviva, V., Addison, G. E., Ade, P. A. R., Aguirre, P., Amiri, M., Appel, J. W., Barrientos, L. F., Battistelli, E. S., Battaglia, N., Bond, J. R., Brown, B., Burger, B., Calabrese, E., Chervenak, J., Crichton, D., Das, S., Devlin, M. J., Dicker, S. R., Bertrand Doriese, W., Dunkley, J., Dünner, R., Essinger-Hileman, T., Faber, D., Fisher, R. P., Fowler, J. W., Gallardo, P., Gordon, M. S., Gralla, M. B., Hajian, A., Halpern, M., Hasselfield, M., Hernández-Monteagudo, C., Hill, J. C., Hilton, G. C., Hilton, M., Hincks, A. D., Holtz, D., Huffenberger, K. M., Hughes, D. H., Hughes, J. P., Infante, L., Irwin, K. D., Jacobson, D. R., Johnstone, B., Baptiste Juin, J., Kaul, M., Klein, J., Kosowsky, A., Lau, J. M., Limon, M., Lin, Y.-T., Louis, T., Lupton, R. H., Marriage, T. A., Marsden, D., Martocci, K., Mauskopf, P., McLaren, M., Menanteau, F., Moodley, K., Moseley, H., Netterfield, C. B., Niemack,

M. D., Page, L. A., Page, W. A., Parker, L., Partridge, B., Plimpton, R., Quintana, H., Reese, E. D., Reid, B., Rojas, F., Sehgal, N., Sherwin, B. D., Schmitt, B. L., Spergel, D. N., Staggs, S. T., Stryzak, O., Swetz, D. S., Switzer, E. R., Thornton, R., Trac, H., Tucker, C., Uehara, M., Visnjic, K., Warne, R., Wilson, G., Wollack, E., Zhao, Y., and Zunckel, C. (2013). The Atacama Cosmology Telescope: cosmological parameters from three seasons of data. *J. Cosmology Astropart. Phys.*, 10:060. 24

Smoot, G. F., Bennett, C. L., Kogut, A., Wright, E. L., Aymon, J., Boggess, N. W., Cheng, E. S., de Amici, G., Gulkis, S., Hauser, M. G., Hinshaw, G., Jackson, P. D., Janssen, M., Kaita, E., Kelsall, T., Keegstra, P., Lineweaver, C., Loewenstein, K., Lubin, P., Mather, J., Meyer, S. S., Moseley, S. H., Murdock, T., Rokke, L., Silverberg, R. F., Tenorio, L., Weiss, R., and Wilkinson, D. T. (1992). Structure in the COBE differential microwave radiometer first-year maps. *ApJ*, 396:L1–L5. 3

Springel, V., Frenk, C. S., and White, S. D. M. (2006). The large-scale structure of the Universe. *Nature*, 440:1137–1144. 27

Staggs, S., Dunkley, J., and Page, L. (2018). Recent discoveries from the cosmic microwave background: a review of recent progress. *Reports on Progress in Physics*, 81(4):044901. 19

Steidel, C. C., Pettini, M., and Adelberger, K. L. (2001). Lyman-Continuum Emission from Galaxies at Z ˜= 3.4. *ApJ*, 546:665–671. 10

Sunyaev, R. A. and Zeldovich, Y. B. (1972). The Observations of Relic Radiation as a Test of the Nature of X-Ray Radiation from the Clusters of Galaxies. *Comments on Astrophysics and Space Physics*, 4:173. 19, 38

Sunyaev, R. A. and Zeldovich, Y. B. (1980a). Microwave background radiation as a probe of the contemporary structure and history of the universe. *ARA&A*, 18:537–560. 19, 38

Sunyaev, R. A. and Zeldovich, Y. B. (1980b). The velocity of clusters of galaxies relative to the microwave background - The possibility of its measurement. *MNRAS*, 190:413–420. 19, 38

Teyssier, R. (2002). Cosmological hydrodynamics with adaptive mesh refinement. A new high resolution code called RAMSES. *A&A*, 385:337–364. 29, 39

Teyssier, R., Pires, S., Prunet, S., Aubert, D., Pichon, C., Amara, A., Benabed, K.,

Colombi, S., Refregier, A., and Starck, J.-L. (2009). Full-sky weak-lensing simulation with 70 billion particles. *A&A*, 497:335–341. 28

Thies, I. and Kroupa, P. (2007). A discontinuity in the low-mass initial mass function. *The Astrophysical Journal*, 671(1):767–780. xi, 12

Thomas, R. M., Zaroubi, S., Ciardi, B., Pawlik, A. H., Labropoulos, P., Jelic, V., Bernardi, G., Brentjens, M. A., de Bruyn, A. G., Harker, G. J. A., Koopmans, L. V. E., Mellema, G., Pandey, V. N., Schaye, J., and Yatawatta, S. (2009). Fast large-scale reionization simulations. *MNRAS*, 393(1):32–48. xi, 9

Topping, M. W. and Shull, J. M. (2015). The Efficiency of Stellar Reionization: Effects of Rotation, Metallicity, and Initial Mass Function. *The Astrophysical Journal*, 800(2):97. 13

Trac, H., Bode, P., and Ostriker, J. P. (2011). Templates for the Sunyaev-Zel'dovich Angular Power Spectrum. *ApJ*, 727:94. 24, 27

Trac, H. and Cen, R. (2007). Radiative Transfer Simulations of Cosmic Reionization. I. Methodology and Initial Results. *ApJ*, 671:1–13. 9

Tumlinson, J. and Shull, J. M. (2000). Zero-metallicity stars and the effects of the first stars on reionization. *The Astrophysical Journal*, 528(2):L65–L68. 11, 13

Tumlinson, J., Venkatesan, A., and Shull, J. M. (2004). Nucleosynthesis, reionization, and the mass function of the first stars. *The Astrophysical Journal*, 612(2):602–614. 11, 13

van Haarlem, M. P., Wise, M. W., Gunst, A. W., Heald, G., McKean, J. P., Hessels, J. W. T., de Bruyn, A. G., Nijboer, R., Swinbank, J., Fallows, R., Brentjens, M., Nelles, A., Beck, R., Falcke, H., Fender, R., Hörandel, J., Koopmans, L. V. E., Mann, G., Miley, G., Röttgering, H., Stappers, B. W., Wijers, R. A. M. J., Zaroubi, S., van den Akker, M., Alexov, A., Anderson, J., Anderson, K., van Ardenne, A., Arts, M., Asgekar, A., Avruch, I. M., Batejat, F., Bähren, L., Bell, M. E., Bell, M. R., van Bemmel, I., Bennema, P., Bentum, M. J., Bernardi, G., Best, P., Bîrzan, L., Bonafede, A., Boonstra, A.-J., Braun, R., Bregman, J., Breitling, F., van de Brink, R. H., Broderick, J., Broekema, P. C., Brouw, W. N., Brüggen, M., Butcher, H. R., van Cappellen, W., Ciardi, B., Coenen, T., Conway, J., Coolen, A., Corstanje, A., Damstra, S., Davies, O., Deller, A. T., Dettmar, R.-J., van Diepen, G., Dijkstra, K., Donker, P., Doorduin, A., Dromer, J., Drost, M., van Duin, A., Eislöffel, J., van Enst, J., Ferrari, C., Frieswijk, W.,

Gankema, H., Garrett, M. A., de Gasperin, F., Gerbers, M., de Geus, E., Grießmeier, J.-M., Grit, T., Gruppen, P., Hamaker, J. P., Hassall, T., Hoeft, M., Holties, H. A., Horneffer, A., van der Horst, A., van Houwelingen, A., Huijgen, A., Iacobelli, M., Intema, H., Jackson, N., Jelic, V., de Jong, A., Juette, E., Kant, D., Karastergiou, A., Koers, A., Kollen, H., Kondratiev, V. I., Kooistra, E., Koopman, Y., Koster, A., Kuniyoshi, M., Kramer, M., Kuper, G., Lambropoulos, P., Law, C., van Leeuwen, J., Lemaitre, J., Loose, M., Maat, P., Macario, G., Markoff, S., Masters, J., McFadden, R. A., McKay-Bukowski, D., Meijering, H., Meulman, H., Mevius, M., Middelberg, E., Millenaar, R., Miller-Jones, J. C. A., Mohan, R. N., Mol, J. D., Morawietz, J., Morganti, R., Mulcahy, D. D., Mulder, E., Munk, H., Nieuwenhuis, L., van Nieuwpoort, R., Noordam, J. E., Norden, M., Noutsos, A., Offringa, A. R., Olofsson, H., Omar, A., Orrú, E., Overeem, R., Paas, H., Pandey-Pommier, M., Pandey, V. N., Pizzo, R., Polatidis, A., Rafferty, D., Rawlings, S., Reich, W., de Reijer, J.-P., Reitsma, J., Renting, G. A., Riemers, P., Rol, E., Romein, J. W., Roosjen, J., Ruiter, M., Scaife, A., van der Schaaf, K., Scheers, B., Schellart, P., Schoenmakers, A., Schoonderbeek, G., Serylak, M., Shulevski, A., Sluman, J., Smirnov, O., Sobey, C., Spreeuw, H., Steinmetz, M., Sterks, C. G. M., Stiepel, H.-J., Stuurwold, K., Tagger, M., Tang, Y., Tasse, C., Thomas, I., Thoudam, S., Toribio, M. C., van der Tol, B., Usov, O., van Veelen, M., van der Veen, A.-J., ter Veen, S., Verbiest, J. P. W., Vermeulen, R., Vermaas, N., Vocks, C., Vogt, C., de Vos, M., van der Wal, E., van Weeren, R., Weggemans, H., Weltevrede, P., White, S., Wijnholds, S. J., Wilhelmsson, T., Wucknitz, O., Yatawatta, S., Zarka, P., Zensus, A., and van Zwieten, J. (2013). LOFAR: The LOw-Frequency ARray. *A&A*, 556:A2. 17

Weinberg, D. H., Davé, R., Katz, N., and Kollmeier, J. A. (2003). The Lyman-α Forest as a Cosmological Tool. In Holt, S. H. and Reynolds, C. S., editors, *The Emergence of Cosmic Structure*, volume 666 of *American Institute of Physics Conference Series*, pages 157–169. 16

Weltman, A., Bull, P., Camera, S., Kelley, K., Padmanabhan, H., Pritchard, J., Raccanelli, A., Riemer-Sørensen, S., Shao, L., Andrianomena, S., Athanassoula, E., Bacon, D., Barkana, R., Bertone, G., Bonvin, C., Bosma, A., Brüggen, M., Burigana, C., Bœhm, C., Calore, F., Cembranos, J. A. R., Clarkson, C., Connors, R. M. T., de la Cruz-Dombriz, Á., Dunsby, P. K. S., Fonseca, J., Fornengo, N., Gaggero, D., Harrison, I., Larena, J., Ma, Y.-Z., Maartens, R., Méndez-Isla, M., Mohanty, S. D., Murray, S. G., Parkinson, D., Pourtsidou, A., Quinn, P. J., Regis, M., Saha, P., Sahlén, M.,

Sakellariadou, M., Silk, J., Trombetti, T., Vazza, F., Venumadhav, T., Vidotto, F., Villaescusa-Navarro, F., Wang, Y., Weniger, C., Wolz, L., Zhang, F., and Gaensler, B. M. (2018). Fundamental Physics with the Square Kilometre Array. *arXiv e-prints*. 17

Windhorst, R. A., Timmes, F. X., Wyithe, J. S. B., Alpaslan, M., Andrews, S. K., Coe, D., Diego, J. M., Dijkstra, M., Driver, S. P., Kelly, P. L., and Kim, D. (2018). On the observability of individual population III stars and their stellar-mass black hole accretion disks through cluster caustic transits. *The Astrophysical Journal Supplement Series*, 234(2):41. 13

Wouthuysen, S. A. (1952). On the excitation mechanism of the 21-cm (radio-frequency) interstellar hydrogen emission line. *AJ*, 57:31–32. 17

Wyithe, J. S. B. and Bolton, J. S. (2011). Near-zone sizes and the rest-frame extreme ultraviolet spectral index of the highest redshift quasars. *MNRAS*, 412(3):1926–1936. xiii, 47

Yoshida, N., Abel, T., Hernquist, L., and Sugiyama, N. (2003). Simulations of Early Structure Formation: Primordial Gas Clouds. *ApJ*, 592:645–663. 10

Yoshida, N., Hosokawa, T., and Omukai, K. (2012). Formation of the first stars in the universe. *Progress of Theoretical and Experimental Physics*, 2012(1):01A305. 10

Zahn, O., Reichardt, C. L., Shaw, L., Lidz, A., Aird, K. A., Benson, B. A., Bleem, L. E., Carlstrom, J. E., Chang, C. L., Cho, H. M., Crawford, T. M., Crites, A. T., de Haan, T., Dobbs, M. A., Doré, O., Dudley, J., George, E. M., Halverson, N. W., Holder, G. P., Holzapfel, W. L., Hoover, S., Hou, Z., Hrubes, J. D., Joy, M., Keisler, R., Knox, L., Lee, A. T., Leitch, E. M., Lueker, M., Luong-Van, D., McMahon, J. J., Mehl, J., Meyer, S. S., Millea, M., Mohr, J. J., Montroy, T. E., Natoli, T., Padin, S., Plagge, T., Pryke, C., Ruhl, J. E., Schaffer, K. K., Shirokoff, E., Spieler, H. G., Staniszewski, Z., Stark, A. A., Story, K., van Engelen, A., Vanderlinde, K., Vieira, J. D., and Williamson, R. (2012). Cosmic Microwave Background Constraints on the Duration and Timing of Reionization from the South Pole Telescope. *ApJ*, 756:65. 21

Zahn, O., Zaldarriaga, M., Hernquist, L., and McQuinn, M. (2005). The Influence of Nonuniform Reionization on the CMB. *ApJ*, 630:657–666. 21

Zaroubi, S. (2013). The Epoch of Reionization. In Wiklind, T., Mobasher, B., and Bromm,

V., editors, *The First Galaxies*, volume 396 of *Astrophysics and Space Science Library*, page 45. 9

Zeldovich, Y. B., Illarionov, A. F., and Syunyaev, R. A. (1972). Influence of Energy Release on the Radiation Spectrum in the Hot Model of the Universe. *Zhurnal Eksperimentalnoi i Teoreticheskoi Fiziki*, 62:1217. 25

Zhang, L., Chen, X., Lei, Y.-A., and Si, Z.-G. (2006). Impacts of dark matter particle annihilation on recombination and the anisotropies of the cosmic microwave background. *Phys. Rev. D*, 74(10):103519. 10

Zhang, P., Pen, U.-L., and Trac, H. (2004a). Precision era of the kinetic Sunyaev-Zel'dovich effect: simulations, analytical models and observations and the power to constrain reionization. *MNRAS*, 347:1224–1233. 20

Zhang, P., Pen, U.-L., and Trac, H. (2004b). The temperature of the intergalactic medium and the Compton y parameter. *MNRAS*, 355:451–460. 24, 63